Development of high-performance gas sensors integrated on wearable substrates with two-dimensional nanostructure materials

by

Eunji Lee

A dissertation submitted to the Graduate Faculty of
Auburn University
in partial fulfillment of the
requirements for the Degree of
Doctor of Philosophy

Auburn, Alabama
December 15, 2018

Keywords: Wearable electronics, Gas sensors, Graphene oxide, hybrids, TMDs, MXenes.

Approved by

Dong-Joo (Daniel) Kim, Chair, Professor of Materials Engineering
Majid Beidaghi, Assistant Professor of Materials Engineering
Pengyu Chen, Assistant Professor of Materials Engineering
Taesik Oh, Assistant Professor of Chemical Engineering

Abstract

In this dissertation, much effort has been dedicated to developing high-performance gas sensors utilizing two-dimensional (2D) nanostructure materials integrated onto wearable substrates. Low-temperature and non-corrosive manufacture processes were explored to adapt wearable textile as a sensor platform, and solution process was selected to deposit sensing nanomaterials. The focus was placed on the control of wettability of the sensing solution by adjusting the ratio between two types of solvents, ethanol and water. Improved adhesion between sensing film and hydrophilic fabric was obtained by tailoring wetting properties of solution where the surface tension of the solution and capillary force of spatial hole in the woven fabric were balanced, resulting in uniformly stacked structure and high resistance of bending.

Room-temperature sensing properties of two-dimensional (2D) nanomaterials were studied using two representative 2D nanomaterials, graphene oxide (GO) and molybdenum disulfide (MoS_2). An attempt was made to develop an understanding of sensing properties of 2D nanomaterials by examining their material properties. In particular, the effect of surface dangling bonds of 2D nanomaterials on sensing properties was mainly investigated. Analysis of the trend in the sensing behavior of 2D nanomaterials in terms of surface functionality provides guidance for material selection with desired sensing properties.

Newly emerged 2D MXene was introduced as a promising room-temperature sensing material with their intriguing surface chemistry. The capability of titanium carbide ($Ti_3C_2T_x$) to sense an array of VOC gases was demonstrated. The possible sensing mechanism of the MXene

sensor was proposed in terms of the interaction between sensing species and the oxygen terminated surface of MXene. Another MXene material, vanadium carbide (V_2CT_x), was also investigated. 2D V_2CT_x gas sensors showed outstanding gas sensing performance and sensitivity toward non-polar gases such as hydrogen and methane. Compared to $Ti_3C_2T_x$ sensor, enhanced sensing response of V_2CT_x was observed to the tested VOC gases, and selectivity to hydrogen was shown. Transformation of ordered structure and constituent elements of MXenes play an important role in interaction between analyte and MXenes showing outstanding selectivity and LoD to non-polar gases.

To enhance sensing performance of 2D nanomaterials, the incorporation of 2D materials and metal oxides was considered. The gas sensing performance of the GO/TiO_2 hybrid was enhanced due to titanium dioxide (TiO_2). Detection of various reducing gases was enabled with higher response and reduced recovery time than GO sensor. To extend long-term stability of the sensor, the GO/TiO_2 solution was irradiated by ultraviolet. Due to the photocatalysis of TiO_2, the gas sensing behavior of the hybridized sensor was converted from n-type to p-type, which confirms that the dominant sensing material of the composite is GO, and TiO_2 acts as a catalyst. The function to identify target gas was maintained over one month, showing strong resistance to humidity due to photo reduced GO. The emphasis places on more specific elaboration of each materials' role in sensing mechanism by tailoring charge transfer under the same hybrid structure to provide a framework for effective design of new hybrids and ultimately advance their sensing performances.

Acknowledgments

It is with my deepest appreciation to my academic advisor Dr. Dong-Joo (Daniel) Kim to whom enabled me to pursuit a Ph. D. with this great dissertation. I sincerely appreciate all his contribution with his precious dedication, counsel, and encouragement to guide me during my Ph.D. study in Auburn University. It is one of my greatest luck to study under his advices.

I wish to express my gratitude to my committee members, Dr. Majid Beidaghi, Dr. Pengyu Chen, Dr. Taesik Oh, and Dr. Minseo Park, for their valuable advice to hole me up for consistent work. Due to their professional suggestions on my research, my Ph.D. study could be much developed and progressed.

I also would like to thank to my group members, Dr. Hyejin Park, Dr. Yoonsung Chung, Dr. Seokhee Lee, Mr. Doohee Lee, Mr. Jaesik Yoon, Mr. Christopher Lincoln, Ms. Karenna Choi, Mr. Benjamin Keith, Mr. Ian Crane, for their co-work and support through all these years. Especially, thank you Mr. Steve Moore and Ms. Cheryl Rhodes for many service in the material engineering department.

In addition, I am thankful to my friends: Ms. Sein Kim, Ms. Jinna Lee, Ms. Jihyun Sung, Ms. Hannah Davis, Ms. Seungyeon Seo, Ms. Yesseul Choi, Ms. Yaeji Kim, and my materials friends: Ms. Xingxing Zhang, Ms. Bethany Brooks, Ms. Sadhwi Ravichandran, Mr. Hossein Talebinezhad, Mr. Songtao Du, Mr. Armin Vahid Mohammadi, Mr. Jafar Orangi, and Mr. Lang Zhou for many enjoyable conversations and friendships.

Lastly, I must give my all appreciation and admiration to my family: Mr. Dong myung Lee, Ms. Kyunglim Park, Ms. Minji Lee and Mr. Chungman Yang. Any words cannot express their endless supports and love. Thank you for being there when I needed you the most. Thank you for helping me through all these tough times in my life. Thank you for being such a good family no matter what I did, but most of all, thank you for being you. I love you so much.

Table of Contents

List of Tables

List of Figures

List of Abbreviations

SnO_2 Tin Oxide

ZnO Zinc Oxide

NiO Nickel Oxide

CuO Copper Oxide

TiO_2 Titanium Oxide

Fe_2O_3 Iron Oxide

WO_3 Tungsten Oxide

Co_3O_4 Cobalt Oxide

VO_x Vanadium Oxide

GO Graphene Oxide

rGO Reduced Graphene Oxide

CNT Carbon Nano Tube

MoS_2 Molybdenum Disulfide

TMD Transition Metal Dichalcogenide

$Ti_3C_2T_x$ Titanium Carbide

V_2CT_x Vanadium Carbide

O Oxygen

OH Hydroxyl

F Fluorine

Pt Platinum

Ti Titanium

Cr Chromium

Ag Silver

Au Gold

Pd Palladium

DI water Deionized water

HF Hydrofluoric

DMSO Dimethyl Sulfoxide

TBA^+ Tetra n-Butyl Ammonium ions

$NaBH_4$ Sodium borohydride

DFT Density Functional Theory

MD Molecular Dynamics

RT Room Temperature

ML Multilayered

PET Polyethylene Terephthalate

PVC Poly Vinyl Chloride

PVD Physical Vapor Deposition

CVD Chemical Vapor Deposition

SEM Scanning Electron Microscopy

XRD X-ray Diffraction

EDS Energy Dispersive X-ray Spectroscopy

XPS X-ray Photoelectron Spectroscopy

FTIR Fourier Transform Infrared Spectroscopy

AFM Atomic Force Microscopy

I-V Current Voltage

NMR Nuclear Magnetic Resonance spectroscopy

VOC Volatile Organic Compound

UV Ultra Violet

UV-Vis Ultraviolet–visible

DC Direct Current

RF Radio Frequency

MFC Mass Flow Controller

S/N Signal to Noise

FWHM Full Width at Half Maximum

LOD Limit of Detection

e Electrons

h Holes

Ø Work function

Chapter 1. Introduction

1.1. Background and motivation

A gas sensor is a device that identifies the presence and amount of target gases. The detection of gas molecules is extremely important for many purposes such as environmental monitoring, air and water quality control, agricultural condition monitoring, and food safety to prevent disastrous accidents from gas emission, normally as part of a safety system[1-3]. Among several types of gas detectors, chemiresistive gas sensors have received lots of attention due to their many advantages compared to other gas detecting equipment, such as acoustic, optical, and calorimetric methods[4]. Chemiresistors are a class of chemical sensor that based on the chemical interaction between the sensing material and the analyte. It is consisting of a sensing material that bridges the gap of two electrodes, and the electrical variation between the electrodes is measured by the presence or absence of the analyte. The benefits of chemiresistive sensors include low cost, small size and long lifetime, which contribute to their widespread use as a gas detector.

Recently, the development of chemiresistive gas sensors is brought by nanotechnology. Nanoscience enables sensing materials to be controlled in the level of molecules, which innovatively enhances the performance of chemiresistive gas sensors including the aspect of gas sensor design and its functionality.[5] For example, the most critical factor that influences gas response is the specific surface to volume ratio, which is much enlarged in nanostructures than conventional micro sensors. With the power of nanotechnology, the performance of miniaturized sensor has been improved and the sensor can be integrated in many practical applications such as

smart phones. To be more pragmatic, emphasis has been placed on more functionalities such as portability and wearability. As the demands of flexible and wearable electronics increase, wearable sensors have emerged as new interest for smart sensing applications[6-7]. Wearable electronics have evolved from life-supporting devices for solders to fashion accessories such as smart watches. Wearable devices are not limited to on-body devices since they can be further transformed by integrating with other surfaces such building and vehicles. Accordingly, the market demand for wearables keeps greatly increasing, and the research in sensor field directs towards the adaption of wearability. By combining ubiquitous computing and smart textile technology, high performance sensor with wearability has been developed to be adapted in various applications. On the wearable platform, miniaturized gas sensors will provide real-time information of the atmosphere to protect each personnel from possible hazardous chemical attacks. Moreover, high performance sensors on adaptable and wearable platform are anticipated to play an important role in future medical diagnostics and physiological monitoring[8-9]. For example, the level of exhaled ammonia can be an important index for viral and bacterial infections in lung diseases or in renal diseases. In the breath of an unhealthy person, 5 ppm of ammonia is generally detected, whereas only 1 ppm should be exist in normal person.[10] Therefore, the use of easy accessible breath testing device will be beneficial to early detection of disease by continuously checking the patients' breaths, and wearable gas sensor can technically support it as medical applications.

To realize wearable gas sensors, functional materials that measure amounts of gases should be built on wearable platform. For portable and wearable gas sensor devices, electronic hardware should be flexible for a comfortable fit and gas detection should be possible at low temperatures without a power supply. However, there is a large practical discrepancy to materialize and commercialize wearable gas sensor. Integration electronic circuits on wearable substrates remain

2

as a big technical challenge. The main challenges of the smart fabric technologies are difficult mass production of components and high cost. Textile circuitry which is a technique to fabricate circuits on fabrics is the essential part for a smart fabric technology. Solution process is the most convenient way among many coating methods in terms of mass producibility. To process solution deposition on bare fabric, unlike solid substrate, wettability of the solution of sensing materials should be carefully controlled due to the porousness and roughness of the fabric. To cut down process complexity and costs in the engineering aspect, finding suitable textiles and manufacturing methods are necessary for the expansion of wearable electronics. In addition, the working temperature of commercialized sensing materials limits application towards wearable gas sensors. The common sensing materials in commercial sensors are metal oxides such as SnO_2, ZnO, and NiO with working temperatures of over 100 °C, which in principle restricts to apply them to wearable gas sensors. As an alternative, 2D nanomaterials such as graphene relatives have been adapted for RT sensing materials. However, most of 2D nanomaterials sensor have focused on detection of polar molecules, and their sensing mechanism based on material's properties have not been clearly established. Furthermore, the performance of gas sensors such as their sensitivity, selectivity, and stability needs to be improved. Considering the future medical application of wearable gas sensors, sensors should be able to detect target chemical in the range of a single ppm or ppb within several minutes. The sensor should discriminate chemicals having same functional groups to obtain high selectivity at RT.

1.2. Objectives of research

In this dissertation, the development of high-performance gas sensors on wearable substrates will be studied by overcoming the aforementioned limitations; the challenges are deficient adaptability, high working temperature, and insufficient sensing performance. The main approach to surmount these challenges will be focused on the development of process engineering to embed gas sensors on fabric platforms, exploration of two-dimensional (2D) nanostructured materials, introduction of new 2D sensing material, and investigation of sensing materials hybridization.

1. To fabricate sensor prototypes on fabric platforms, various substrates and manufacture processes were explored. Sensor electronics were integrated on bare nylon, polyester, and cotton fabrics using sputtering and silk-printing as low-temperature and non-corrosive methods. Sensing material, graphene oxide (GO), was dispersed in two types of solvents of water and ethanol and then deposited on bare fabrics by drop-casting. In solution process, wettability of the solution was controlled by the mixture of solvent. Then the gas sensing properties of the GO fabric sensor were compared to those on solid substrates.

2. To achieve room temperature (RT) sensing on wearable platforms, 2D nanostructured materials were adopted instead of conventional metal oxides, which are in principle difficult to operate at low temperature. Typical 2D materials with semiconducting properties, graphene-based materials and transition metal dichalcogenide (TMDs), were explored by specifically focusing on the dangling bonds on the surface of 2D materials. Two representatives were selected, GO with considerable amount of oxygen functional

groups, and MoS$_2$ with few dangling bonds on the surface. Through investigation of materials properties based on surface dangling bonds, sensing mechanisms and sensing performances were comprehensively understood.

3. To find the best performing sensing materials, newly emerged 2D materials of MXenes were introduced to gas sensor applications. MXenes consist of 2D transition metal carbides, nitrides, and carbonitrides with chemically active terminations. Since its discovery in 2011, experimental investigation on the sensing properties of MXenes has not been published. Yet, theoretical studies on the material have suggested the potential of MXenes to be used for detecting volatile organic compound (VOC) gases. Therefore, the material characteristics of two different MXenes, Ti$_3$C$_2$T$_x$ and V$_2$CT$_x$, were explored for sensing materials, and RT gas sensing was demonstrated. The fundamental physics behind the gas sensing behavior of MXenes was also investigated as well as relative performance comparison.

4. To enhance the sensing performance of 2D nanomaterials, hybrid structures combining 2D materials and metal oxides were studied. Since the selectivity is strongly dependent on the type of materials utilized, arraying sensing materials or constructing hybrid structures should be a reasonable approach to improve selectivity and gas response. Metal oxide (TiO$_2$) nanoparticles were hybridized on GO nanosheets. In addition, the hybrid was UV-treated in consideration of the photocatalytic effect of TiO$_2$, and gas sensing properties of the two hybrids were comprehensively analyzed. Focused investigations were on clear understanding of mechanism and hybridization effect of the hybrid structure.

5

1.3. Dissertation structure

This dissertation constitutes of 9 chapters from an introduction to summary of the research. Each chapter covers details that are listed below.

Chapter 1 introduces the importance of my research and its contribution to scientific and engineering fields, outlining the motivation, objectives, and dissertation structure.

Chapter 2 elaborates the purpose of this dissertation based on the research backgrounds and literature review, including process engineering to integrate sensor devices onto wearable substrates, exploration of two-dimensional (2D) materials for room temperature detection, introduction of new 2D nanomaterials (MXenes) for gas sensing applications, and investigation of hybrids consisting of 2D nanomaterials and metal oxides.

Chapter 3 provides the details of experiments: processes to synthesize solutions / suspension of sensing materials and procedures to measure the gas sensing properties.

Chapter 4 describes various engineering processes to manufacture wearable gas sensors.

Chapter 5 shows the investigation of 2D nanomaterials, graphene oxide (GO) and molybdenum disulfide (MoS_2), focusing on their surface dangling bonds for room temperature detection.

Chapter 6 demonstrates the sensing properties of 2D titanium carbide (MXenes).

Chapter 7 describes the sensing properties of 2D vanadium carbide (MXenes).

Chapter 8 addresses the investigation of hybrids constituting 2D nanomaterials (GO) and metal oxide (TiO_2) to enhance sensing performance.

Chapter 9 summarized the achievements attained from this research and future study direction that may further advance the field.

Chapter 2. Research Background and Literature Review

2.1. Process engineering to integrate sensors device on wearable substrates

The two main technical challenges to fabricate wearable gas sensor are the integration of electrodes and deposition of sensing materials. Fabric is a highly desirable platform for wearable gas sensors due to its flexibility and light weight, which make it an excellent candidate for use in various human activities[11]. However, since the structure of fabric is porous, rough, and non-organized, traditional fabrication methods such as lithography are not appropriate to build electrodes. In addition, due to the low thermal resistance of many fabrics, processes requiring high temperature such as chemical vapor deposition (CVD) must be avoided. As a pre-step, alternative materials such as paper and polymeric film have been applied as a flexible platform in previous literatures. Their flexibility and non-organized structure are similar to fabric, but more flat, rigid and solid. Table 1 shows the literature survey of summarized process methods and gas sensing conditions on flexible substrates. Typically, paper and PET (Polyethylene terephthalate), the most common thermoplastic polymer resin of the polyester fibers used in clothing, were employed as flexible substrates. Due to relatively stronger thermal resistance of the polymer compared to fabric, thermal evaporation and CVD process could be used to fabricate electrodes. For RT detection, carbon-based materials such as CNT or rGO were coated as sensing materials on flexible substrates.

Table 2.1. Literature survey of process method and gas sensing condition using flexible substrates.

Ref	Year	Purpose	Materials	Coating method	Substrate	Electrode coating	Temp	Sensing Condition
[12]	2014	RT flexible ammonia sensor	rGO	vacuum filtration	Filter paper	Thermal evaporation	RT	400–4000 ppm NH_3
[13]	2013	Flexible graphene-based chemical sensors	Graphene	CVD	Paper	Silver paste	RT	200ppm NO_2
[14]	2012	Flexible chemi-resistor for aggressive vapor	CNT	Inkjet-print	PET, Paper	Inkjet-print	RT	250ppb NO_2 500ppb Cl_2
[15]	2011	Flexible sensors	rGO	Drop coating	PET	Thermal evaporation	RT	7.6ppb Rogor
[16]	2014	Flexible NO_2 sensor	rGO	Layer by Layer	PET	Sputtering	RT	1-20ppm NO_2 200ppm NH_3 1000ppm CO, H_2
[17]	2016	Wearable chemical sensor	rGO	Drop coating	polyimide film	Thermal evaporation	RT	5~20ppm H_2S, C_2H_5OH, H_2
[18]	2013	Flexible CNT sensor	CNT	Spray deposition	polyimide film	Thermal evaporation	RT	10~100ppm NH_3

The effort on the development of wearable sensor has been continued beyond flexible substrate, and real fabric has been demonstrated as a sensor platform as listed in table 2.1. In the literatures, woven fabrics such as cotton, wool, and polyester have been adapted as wearable substrates to embed a circuit board by using silk printing and silver paste. In detail, conducting polymer was laminated on the surface of the fabrics, and metal was attached[19]. In another example, circuit was manufactured on functional garment such as GORE-TEX[20], which is a waterproof, breathable fabric membrane and registered trademark of W. L. Gore and Associates. On the fabrics, expanded polytetrafluoroethylene membrane were laminated by a screen-printing process. Then, a metal layer was coated as an under layer and carbon was deposited as working and counter electrode for electrochemical sensing. After that, the ink with insulating property was coated on the fabrics for the insulation. Through these multi-steps process, electrochemical sensor was manufactured on functional garment. In other electrode fabrication processes such as stencil and dispenser, passive materials were laminated prior to the manufacture of the electrode. The role of lamination is to mitigate the rough and porous surface of fabrics so that connection of electrode can be sustained. Typical passive elements used to lamination were conductive inks and polymer. Another modification to enable sensing process on wearable substrate is in the level of yarn before it intertwines to be fabric. Cotton and polyester yarns were coated by sensing materials such as GO, and the treated yarn were intertwined in fabric substrates. To enhance adhesion between yarn and sensing materials, usually BSA (bovine serum albumin) was utilized as a role of glue.

Table 2.2. Literature survey of process method and detailed condition for electrode fabrication on fabrics.

Ref	Purpose	Substrate	Electrode coating	Coating materials	Max Temp	Process detail
19	Fabrication circuit board on fabric	cotton, viscose, silk, wool, polyester (PES), polyacrylonitrile (PAN)	Silk screening + sputter	Conducting epoxy + Au	RT	Silk screening of conducting epoxy and by gold sputtering.
20	Electrochemical sensing	GORE-TEX (Expanded polytetrafluoroethylene membrane laminated by fabrics)	Screen printing	Silver/silver chloride ink + carbon ink	125°C	Silver/silver chloride ink as under layer carbon ink as working/counter electrode Insulating ink printed Curing at 125°C
21	biopotential monitoring	'Escalade' - 46% cotton, 16% polyester and 38% elastic fiber	Screen printing, Stencil printing	polyurethane paste+ silver polymer Conductive rubber + polyerethane	120°C	Polyurethane screen print/UV cure Ag screen print at 120 ∘C Stencil print at 100 ∘C Stencil print/UV cure
22	Functional electrical stimulation	Polyester/cotton blend	paste	Silver + Carbon filled silicone polymer	120°C	Silver flake in vinyl resin polymer and solvent at 120 ∘C Carbon filled silicone polymer paste at 80 ∘C
23	Electronic textile application	Sport textile garment	Stencil printing, Dispenser	Elastomer conductor+Ag flake +	80°C	Elastomer Ink was printed with polyimide stencil mask Heated at 80°C

				fluorine		
				rubber +		
				fluorine		
				surfactant		
24	Single yarn for wearable gas sensor	Cotton, Polyester yarn	Embroidery	GO + BSA (bovine serum albumin)	RT	Dip coating of BSA Electrostatic self-assembly of GO Low temperature reduction of GO
25	E-textile gas sensors	Cotton yarn	Embroidery	BSA+GO +MoS$_2$	40 °C	Dip coating of BSA Electrostatic self-assembly of GO Reduction Oxygen plasma Dip coating of MoS$_2$

As shown in table 2.2, the way of fabricating wearable sensor can be mainly classified as two categories depending on extrinsic or intrinsic modifications. An intrinsic modification is the tailoring fiber and yarns to be sensitive to chemical stimuli. Making sensitive threads can be done by conventional and unconventional methods. Coating methods include electrospinning, wet-spinning, self-assembly, carding, combining, and die extrusion[9]. After integrating sensing materials on yarn, this yarn can be intertwined by sewing, embroidering, and weaving. However, these intertwining methods require a crafted process, which is not proper for mass production. Extrinsic modification can be implemented by two levels; textile circuitry and deposition of sensing materials. Fabrics are extrinsically modified to enable sensing features and electrical conductivity.

| Silk printing | Sputtering | Soldering | Nozzle |
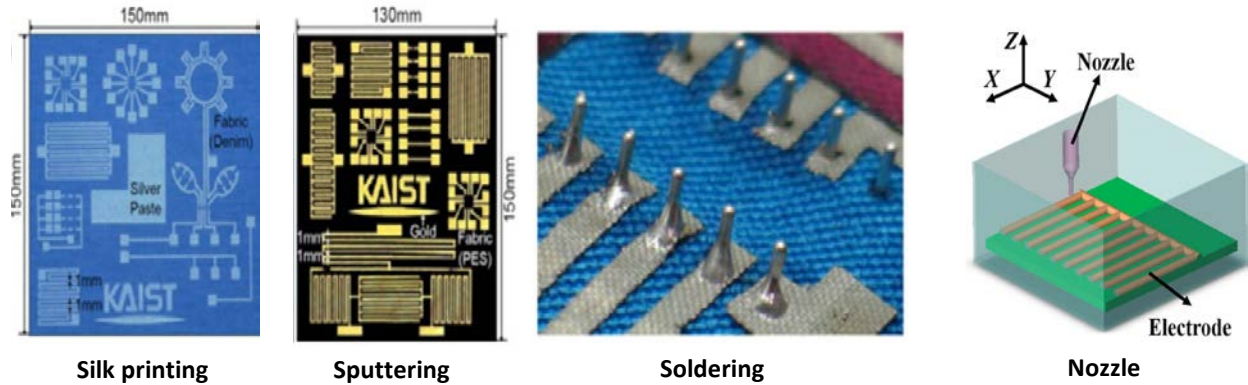
Figure 2.1. Different types of manufactured electrode circuit on fabric.

First, electronics should be embedded on fabric substrates by using low temperature and non-corrosive process. The typical methods of low temperature and non-corrosive process such as silk printing, sputtering, soldering, and nozzling can be considered as shown in Figure 2.1. After manufacturing electrodes on fabric, sensing material working at low temperature should be built on the prepared fabric platform. With fabric substrate, deposition process should also be low temperature process. Among coating methods in table 2.1, solution process such as drop coating, dip coating, inkjet printing, and spray deposition tend to suitable compared to CVD or thermal evaporation. In such solution process, selection of solvent to disperse sensing material is critical, which further influences on coating uniformity and sensing properties. Unlike solid substrates such as silicon wafer, wettability of the sensing solution on bare fabric is critical factor in solution coating process. Solution on fabrics should be balanced between adhesive and cohesive force, otherwise, it passes through the fabric through tiny holes of the woven fabric. In addition, the types of fabrics also influence on coating properties. Depending on its origin of fibers, properties of fabrics are different. For example, cotton with natural fibers shows hydrophilic properties, while, nylon with synthetic fibers have hydrophobic properties. Therefore, Control of the wettability between solution and fabrics is important in solution coating process.

13

2.2. Exploration of 2D nanomaterials for room temperature detection

Chemiresistive sensors work based on sensing materials, and metal oxide semiconductors are the most widely employed sensing materials in chemiresistive sensors due to their low cost, ease of fabrication, as well as high sensitivity to gas molecules. The most studied semiconducting materials for gas sensor application are SnO_2, ZnO, and TiO_2 in order as n-type sensing materials, and CuO and NiO are the typical p-type sensing materials shown in figure 2.2. [26]
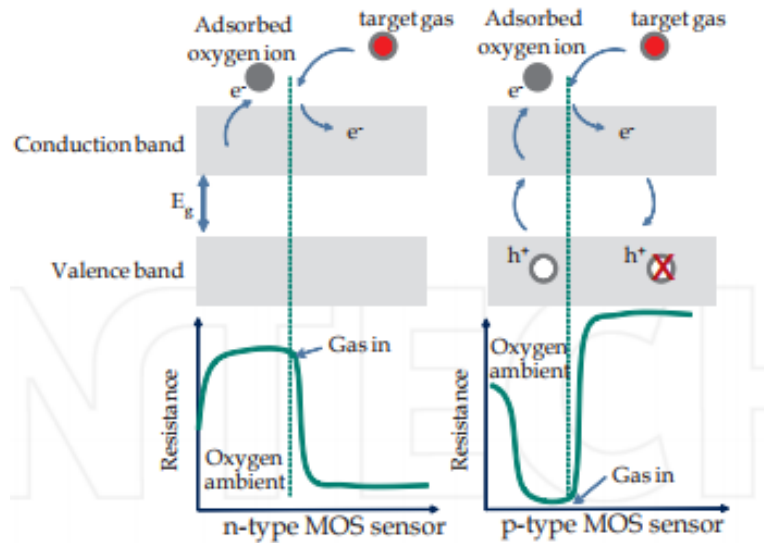
Figure 2.2. The schematic diagram of resistance changes in both n-type and p-type metal oxide sensor with target gas (reducing gas). [27]

Figure 2.2 shows the working principle of metal oxide sensors which has been extensively studied. The sensing mechanism of the conventional metal oxide sensors is related to adsorbed oxygen ions on the oxide surface. The oxygen ions are formed by drawing electrons from the

14

conduction band of the metal oxide, and different forms are possible depending on the operating temperature[27-28]. Below 200°C, electrons are attached to oxygen molecules as shown in Eq. (1). Above 250°C, the oxygen molecules are dissociated into oxygen ion atoms with electric charge by pulling electrons from metal oxide as shown in Eq. (2) and (3).

$$O_2(gas) + e^- \leftrightarrow O_2^-(adsorbed) \text{ [below 200°C] Eq. (1)}$$

$$\frac{1}{2}O_2 + e^- \leftrightarrow O^-(adsorbed) \text{ [above 250°C] Eq. (2)}$$

$$\frac{1}{2}O_2 + 2e^- \leftrightarrow O^{2-}(adsorbed) \text{ [above 250°C] Eq. (3)}$$
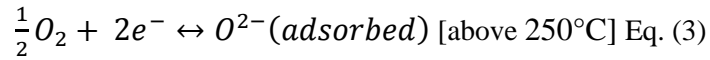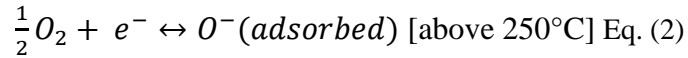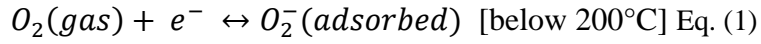
The interaction between the oxygen ions and gas analytes can be divided into two main categories depending on the majority carrier, electrons or holes. When the majority carriers are electrons, the metal oxide is considered to be n-type, while the majority carriers are holes in the p-type metal oxide sensors. Using n-type metal oxides as an example, the electrons in the conduction band of the metal oxide are decreased due to the reactions of Eq. (1) - (3) resulting in increased resistance at the operating temperature. Once the target gas is introduced, the electrons from the reducing gas are transferred to the conduction band of the metal oxide causing the resistance of the sensor to decrease. It should be noted that the opposite resistance change occurs with an oxidizing gas. The categorized sensing behavior of n-type and p-type sensing materials to reducing and oxidizing gases is compared elsewhere[29]. As an example, NO_x is considered as an oxidizing gas due to unpaired electrons around the N atom, while NH_3 acts as a reducing gas due to its lone electron pair.[30] Due to the dominant role of oxygen ions, the metal oxide sensors are typically operated at elevated temperatures. The summarized sensing behavior of n-type and p-type sensing materials to reducing and oxidizing gases was tabled in figure 2.3.

Sensor response behavior	n-type material	p-type material	Example gases
Reducing gases	Resistance decreases	Resistance increases	H_2, H_2S, CO, NH_4, Ethanol, Acetone, CH_4
Oxidizing gases	Resistance increases	Resistance decreases	O_2, O_3, NO_X, CO_2, SO_2
Dominant charge carrier	Electrons (e^-)	Holes (h^+)	–

Figure 2.3. Sensing response behavior of n-type and p-type materials to reducing and oxidizing gases.[29]

Due to the essential mechanism to produce the charge oxygen ions, the optimum temperature for metal oxide sensor is round 200-350°C. As a result, an external or internal heater is normally required to control system temperature. Nevertheless, high working temperature incurs many downsides such as high power-consumptions, the possibility of igniting flammable or explosive gases, which limits the metal oxide gas sensor to be applied in practical applications. In order to decrease the sensing temperature, research has been focused on modification of morphology of metal oxide, doping catalyst, and constructing composite structure[29]. However, these approaches are inevitably dependent on the property of sensing material. Hence, developing novel sensing material that can work at low temperature should be crucial.

Recently, significant upsurge in research interests to two-dimensional (2D) nanostructured materials has aroused to utilize the extraordinary properties inherent to 2D materials for use in multiple fields, including energy storage, electronics, and chemical sensing[31-32]. A 2D nanostructure is defined as one or few atomically layered nano-crystalline materials, which structurally exist as nanosheets, nano-membranes, and nanoflakes[33]. The 2D nanostructure can generally be classified as either 2D allotropic elements or covalently bonded compounds[34]. Originated from their atomically thin layers, the 2D nanostructured materials manifest unique

chemical and physical characteristics, which show great promise for sensing applications. Specifically, the atomic scale thickness of a 2D nanomaterial magnifies the surface to volume ratio, which exposes more active surfaces to target gases. Van der Waals gaps between the characteristic surface configuration of the layers and thickness-dependent physical and chemical properties are distinct qualities that make 2D nanomaterials outstanding candidates for gas sensors[30, 35]. The ability of 2D nanomaterial to identify gas analytes at room temperature offers the possibility of wearable gas sensors integrated on a flexible substrate[36]. By employing 2D nanostructure as sensing materials, sensitivity (gas response), selectivity, adaptability, and portability have been significantly developed. Nanoscale thickness of 2D nanomaterials enhance high surface to volume ratio, which will provide more active surfaces to react to target gas. In addition, newly discovered 2D materials have the potential to be very selective to specific gas molecules as graphene was found to be very sensitive to NO_2 or NH_3 gas. Furthermore, 2D layered structure can be easily integrated on devices with good compatibility and it has the possibility of being assembled into 3D materials. More significantly, it has been demonstrated that 2D nanomaterial has successfully decreased the working temperature for gas sensors, which greatly facilitates the opportunity to be portable devices. Up to now, some emerging 2D materials such as graphene, dichalcogenides, phosphorene, and MXenes have been mentioned as potential gas sensing materials. Gas sensing performance with 2D materials are listed in the table 2.3.

Table 2.3. Literature study on gas sensing performance of chemiresistive sensor with 2D nanomaterials working on room temperature (RT).

Ref	Year	Material	Working temp	Gas	Concentration	Gas response $(\Delta R/R_a)$
[37]	2010	Graphene	RT	NO_2	100ppm	9%
[38]	2010	Graphene	RT	NO_2	18ppm	9%
[39]	2015	Graphene	RT	NO_2	2.5ppm	65%
				NH_3		15%
[40]	2010	rGO	RT	NH_3	100ppm	20%
[41]	2013	rGO	RT	NH_3	200ppm	5.5%
[42]	2013	rGO	RT	NH_3	1ppb	2.4%
[43]	2015	rGO	RT	NH_3	500ppm	2%
				H_2	500ppm	<1%
				NO_2	5ppm	16%
[44]	2014	GO	RT	Ethanol	150ppm	6.21(R_{air}/R_{gas})
[45]	2013	MoS_2	RT	NH_3	2ppm	0.01%
[46]	2015	MoS_2	RT	NO_2	5ppm	15%
				NH_3		1%
[47]	2015	MoS_2	RT	NO_2	120ppb	35%
[48]	2014	$MoSe_2$	RT	NH_3	50ppm	<10%
[49]	2014	WS_2	RT	NH_3	1ppm	0.2%
[50]	2017	WS_2	RT	NH_3	250ppm	2.6
[51]	2015	Black Phosphorus	RT	NO_2	5ppb	2%
[52]	2016	Black Phosphorus	RT	NO_2	0.1ppm	50%
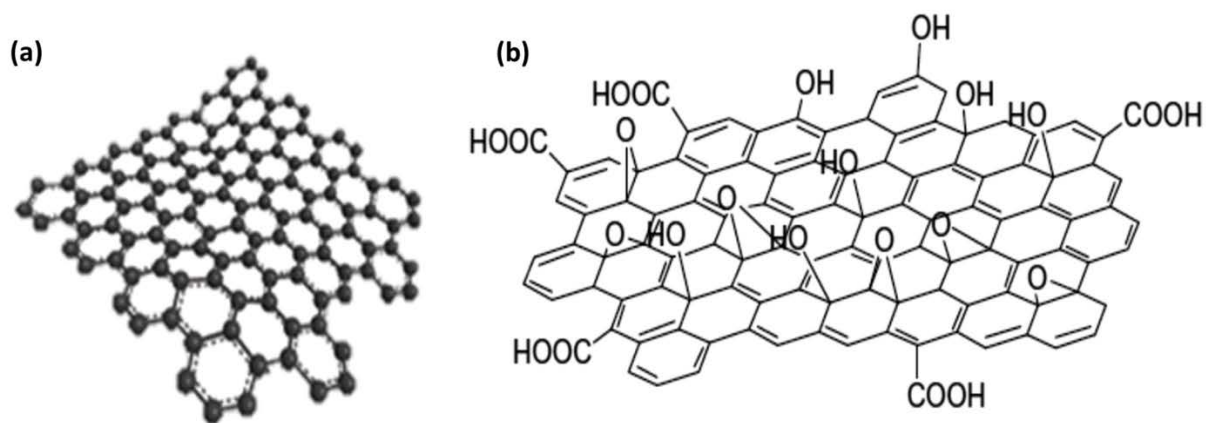
Figure 2.4. The schematic of (a) graphene and (b) the proposed graphene oxide[53].

The intensively studied 2D materials are carbon-based materials due to their high electrical conductivity, large surface to volume ratio, and high charge carrier mobility at RT. Graphene is a monolayer of sp^2 hybridized carbon atoms in a honeycomb lattice, and graphene oxide (GO) is a graphene with oxygen functional groups such as hydroxyl and carboxyl groups on the surface as shown in figure 2.4. Even though much attention has been focused on graphene and modified GO for sensing materials, pure GO has aroused as a practical material due to its capability of mass production and functional groups. The large-scale production of graphene is challenging, and its high-quality manufacture is restricted on laboratory scale by CVD growth or graphite exfoliation. To produce graphene in a large scale, solution-based methods have been processed, with which graphene was oxidized to GO. Thus, further reduction processes should be required to produce graphene from GO, and it is hardly possible to eliminate all functional groups on GO in a large scale as producing reduced GO. More importantly, GO would be preferable for adsorbing gas molecule than graphene, since the surface functional groups such as hydroxyl and epoxy promote

19

the interaction between gas and GO according to Peng et al. [54]. Also, Huang et al. [55] showed larger

adsorption energy and charge transfer of gas molecules such as O_2, N_2, CO_2, NH_3, CO, NO_2 and

NO on graphene nanoribbons with armchair-shaped edges compared to graphene. This is due to

dangling bond defects on graphene which are chemically reactive than graphene that has a stable

sp^2 bonded carbon. Graphene weakly interacts with target gases without dangling bonds on the

surface, resulting in low adsorption energy to attract gas molecules. Leenaerts et al.[56] studied the

interaction between graphene and several gas molecules such as H_2O, NH_3, CO, NO_2, and NO

using density functional theory (DFT) calculation. In their study, it was found that the target gases

were physically absorbed on graphene. However, the common problems of gas sensor such as

sensitivity, selectivity, recovery, and stability are also applied to GO sensors. Considering the

medical application of GO sensor, the sensor should be able to measure target gas in the range of

ppb. However, the sensitivity of most GO sensors could not accommodate that range as listed in

table 2.3. In addition, GO sensor usually responds to many gases such as H_2O, NH_3, CO, NO_2,

H_2S, H_2 and NO, among which NH_3 and NO_2 seem more sensitive than other gases. For the

recovery, the interaction of gas molecules with oxygen functional groups of GO is irreversible

without external assistance owing to high binding energy through single or double hydrogen

bonding. As a result, initial resistance does not recover after target gas removal and degradation

of sensing performance. Besides, initial resistance of GO varies depending on the sample due to

randomly distributed functional groups on the surface of GO. Consequently, controlling functional

groups of GO should be necessary. Moreover, long-term stability of GO sensor against oxidative

conditions is another important issue. It is reported that graphene sensor can be stable up to 100

days in air, however, the stability of GO sensor reduced to half the days of graphene sensor[44].

Therefore, further insights on mechanism and performance development are needed.
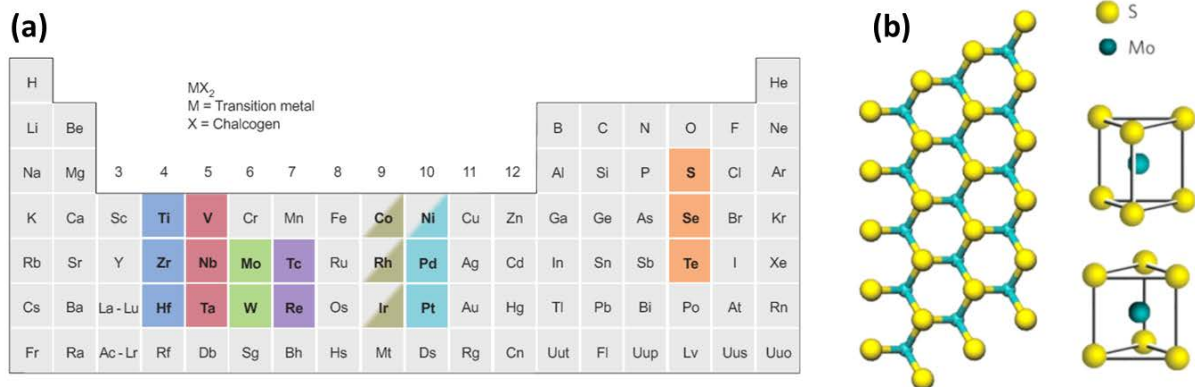
Figure 2.5. Structure of monolayered TMDs. (a) About 40 different layered TMD compounds exist. The transition metals and three chalcogen elements that predominantly crystallize in these layered structures are highlighted in the periodic table. (b) Schematic of MoS_2 monolayer structure.

As mentioned, extensively researched graphene and other carbon-based materials are chemically inert, which requires surface functionalization with other molecules for gas sensing applications. In contrast, 2D Transition metal dichalcogenides (TMDs) display versatile chemistry and tunable band gap that are much more beneficial to design practical gas sensing devices. Transition metal dichalcogenides (TMDs) are MX_2-type inorganic compounds where M is a transition element such as Ti, Zr, Hf, V, Nb, Ta, Mo, W, Tc, or Re in groups IV, V, and VI of the periodic table, and X is an element of the chalcogen species such as S, Se, or Te in figure 2.5. When reduced to single or few layers, the TMDs have shown excellent electric properties comparable to that of graphene[57]. The 2D layered structure of TMDs consists of strong molecular intralayer bonds and weak Van der Waals interlayer bonds. The weak interlayer bonding allows exfoliation of TMDs down to single- or multi-layers by using mechanical exfoliation or electrochemical intercalation[58]. In general, the thickness of layered TMDs is about 6-7 Å, and the length of M-M bond is typically between 3.15-4.03 Å, depending on the size of the metal and

21

chalcogen atoms[59]. Higher specific surface area and functionalities driven by such structure make 2D TMDs promising candidates for sensor applications.

The electronic and magnetic characteristics of TMDs hinge on the coordination number of the transition metal and its d-electrons. The transition metal (M) atoms in TMDs have four electrons to fill the bonding states and chalcogen (X) atoms have an oxidation state of -2. Thus, the number of d orbital electrons will vary 0 to +6, which influences electronic properties. The electrical nature of TMDs can be tuned from semiconductors (MoS_2, $MoSe_2$, WS_2, WSe_2, …), to metallic ($NbTe_2$, $TaTe_2$, ...,), to superconductors (NbS_2, $NbSe_2$, ...). The partially filled d-orbitals in transition metals provide metallic conductivity, while fully filled d-orbitals give semiconducting properties. The surface of layered TMDs is terminated by chalcogen atoms with lone-pair electrons. The absence of dangling bonds in TMDs stabilizes the material against ambient environment and gives high mobility in compliance with the substrates and metal contacts. For instance, the mobility of molybdenum disulfide (MoS_2) is about $700\ cm^{-1}V^{-1}s^{-1}$ on SiO_2/Si substrate at room temperature[60]. An important attribute of TMDs for gas sensing can be a tunable band gap. Graphene, a popular 2D material, is metallic with a zero-band gap, but several TMDs such as molybdenum disulfide (MoS_2), tungsten disulfide (WS_2), and tin disulfide (SnS_2) have a direct and indirect band gap around 1-2 eV due to their low intrinsic carrier concentration. The fascinating electrical and optical properties of TMDs arise from the transition of an indirect band gap to a direct band gap as the thickness changes from bulk to monolayer due to quantum confinement. Moreover, mechanically flexible and strong TMDs can be another advantage to extend fields of chemical sensors. It is reported that few-layered MoS_2 has a high Young's modulus of 0.33 ± 0.07 TPa that outperforms the stainless steel and graphene oxide[61]. In the TMD class, disulfides such as MoS_2, WS_2, and SnS_2, are great representatives of TMDs for chemical sensing. In each layer of

MoS$_2$, Mo atoms are sandwiched between covalently bonded S atoms, with a layer height of about 0.65 nm. As shown in figure 2.5 (b), the crystal structure of MoS$_2$ with a trigonal prismatic arrangement manifests as hexagonal crystal structure[62]. Monolayers of MoS$_2$ have a direct band gap of 1.8 eV while bulk (>8 layers) MoS$_2$ presents an indirect band gap of 1.29 eV. Unique features of MoS$_2$ for gas sensors include a layer-dependent band gap, a high surface to volume ratio, and a high adsorption coefficient. Based on investigation of material properties when it comes to TMD materials, there has been some reports to examine gas sensing performance of the representative TMDs including MoS$_2$, WS$_2$, and MoSe$_2$ in table 2.4. Since most literature uses NH$_3$ and/or NO$_x$ for evaluation of sensing properties, the results were compared in terms of NH$_3$ and/or NO$_x$ gas. RT sensing of TMDs was demonstrated and sensing properties with NH$_3$ and/or NO$_x$ analytes have been studied. However, less efforts have been dedicated to developing TMDs for sensing applications, and the TMD research still needs to address challenges such as selectivity, gas response, response time, recovery time, and stability similar to other 2D sensing materials.

Each 2D material presents different electrical features and surface configurations, which influence their gas sensing properties. Another important interpretation of gas sensing property in 2D TMDs can be conducted by understanding the charge transfer mechanism depending on their surface configuration and electrical characteristics. The interactions between sensing materials and gas molecules can be inferred by the adsorption energy and the amount of charge transfer, which are commonly evidenced by first-principles calculations based on density functional theory (DFT). Such computational simulations were able to consider parameters including adsorption positions and orientations of gas molecules on a 2D material. Table 2.4 gives the results of the DFT simulations on the most stable adsorption position and orientation. Absorption energy between 2D materials and gas molecules was calculated by the Eq. (4)[63].

$$E_{ad} = E_{(2D+gas)} - [E_{(2D)} + E_{(gas)}] \quad \text{Eq. (4)}$$

where $E_{(2D+gas)}$ is the total energy of a supercell containing both a 2D material and a gas molecule, $E_{(2D)}$ is the total energy of the 2D sensing material, and $E_{(gas)}$ is the total energy of a supercell containing a gas molecule. Here, the negative value of E_{ad} indicates an exothermic reaction, meaning thermodynamically favorable reaction. The negative value of ΔQ means the direction of charge transfer from gas molecules to sensing material or vice versa at the optimal adsorption configuration. The large value of adsorption energy can be interpreted as the level of selective response to the gas molecule over other species[55]. The amount of ΔQ can be associated with the number of transferred electrons between gas molecules and the sensing material. In addition, physisorption and chemisorption can be determined from ΔQ value.

Table 2.4. Density Functional Theory (DFT) calculation of adsorption energy and charge transfer for 2D materials

		NH_3	H_2O	NO_2	NO	CO	O_2	H_2	Ref
Graphene	E_{ad} (eV)	0.031	0.047	0.067	0.029	0.014			56
	ΔQ (e)	0.027	-0.025	-0.099	0.018	0.012			
Graphene oxide	E_{ad} (eV)	-0.18		-2.7	-2.29	-1.34	-1.88		55
	ΔQ (e)	0.27		-0.53	-0.55	-0.3	-0.78		
MoS$_2$	E_{ad} (eV)	-0.250	-0.234	-0.276	-0.195	-0.128	-0.106	-0.07	64
	ΔQ (e)	-0.069	0.012	0.100	0.011	0.020	0.034	0.004	

2.3. Introduction of 2D MXenes for gas sensing application
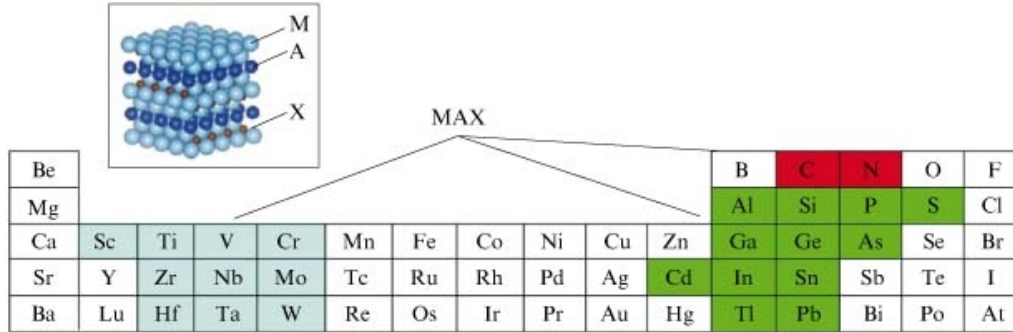
Figure 2.6. Fragment of the periodic table showing elements to form MAX phases of the general composition $M_{n+1}AX_n$ [n=1-3; M is a transition d-metal (blue section); A is a p-element (green section); X is carbon or nitrogen (red section)][65].

Transition metal carbides, carbonitrides and nitrides (MXenes) are among the latest additions to the 2D materials worlds[66]. Since its discovery in 2011, around 20 different MXenes have been successfully synthesized, and its main application is the energy storage such as batteries and capacitors. The recent discovery of ordered, double transition metals MXenes will probably lead to the synthesis of a larger number of this interesting family of materials[66-67]. General formula of MXenes is $M_{n+1}X_nT_x$ (n = 1–3), where M represents an transition d-metal (such as Sc, Ti, Zr, Hf, V, Nb, Ta, Cr, Mo and so on), X is carbon and/or nitrogen and T_x stands for the surface terminations (for example, hydroxyl, oxygen or fluorine) as shown in figure 2.6. $Ti_3C_2T_x$ is the first discovered and well-investigated material of the MXenes. $Ti_3C_2T_x$ is exfoliated from Ti_3AlC_2 MAX phase, a ternary carbide with a hexagonal closed-packed structure, by selectively etching Al

atoms[68-69]. The M-A bonds in the MAX phases are chemically more reactive than M-X bonds, which enables the selective etching of A-layer atoms. The overall crystal of MXenes is a hexagonal close-packed structure. In the case of Ti_3AlC_2, the removal of Al atoms in aqueous hydrofluoric (HF) acid solutions results in weakly bonded $Ti_3C_2T_x$ layers that can be further separated through intercalation of large organic molecules like dimethyl sulfoxide (DMSO)[70]. It is also shown that $Ti_3C_2T_x$ can be synthesized and directly delaminated through etching with a mixture of LiF salt and HCl acid.[71] This method eliminates the use of hazardous HF and intercalation of large organic molecules, resulting in a facile synthesis process for delaminated MXene solutions[71]. In both cases, the surface of $Ti_3C_2T_x$ is mostly terminated by oxygen, hydroxyl, and fluorine groups, and the synthesis method has a great influence on the ratio of these groups on the surface of synthesized MXene[69]. For simplicity, the existence of these different functional groups is shown with T_x in the MXenes formula, i.e. $Ti_3C_2T_x$. According to the Density functional theory (DFT) calculations, the type and concentration of these surface terminations largely affect the properties of MXenes, through which MXenes can be easily tailored in compliance with various applications[29, 72-74].

gas molecules	E_{ads} (eV)	C_T (e)^a	$d_{Gas-Ti2CO2}$ (Å)
NH_3	−0.37	0.174	2.35
H_2	−0.05	0.003	2.76
CO	−0.07	0.004	3.19
CO_2	−0.14	−0.007	3.08
NO_2	−0.12	−0.003	3.35
O_2	−0.08	−0.003	3.46
N_2	−0.12	−0.002	3.71
CH_4	−0.11	−0.001	3.06

^{a}A positive C_T value indicates a transfer of electrons from the gas molecule to Ti_2CO_2.
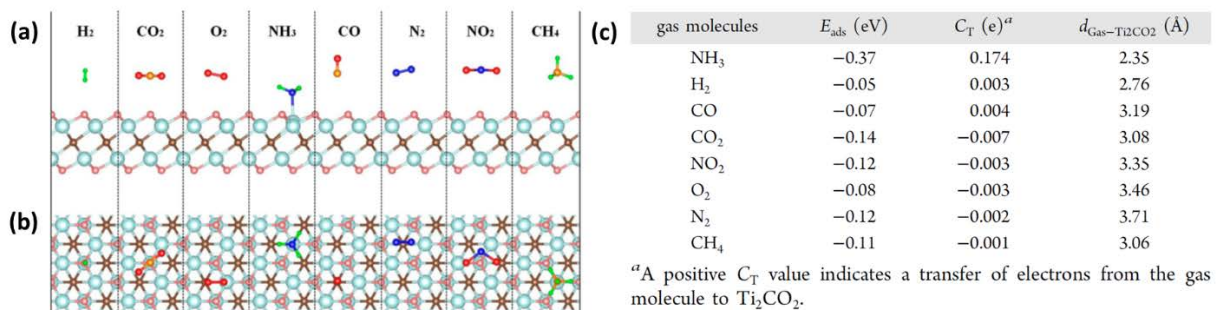
Figure 2.7. A schematic illustration of (a) side, and (b) top view of the adsorption of NH_3, H_2, CH_4, CO, CO_2, N_2, NO_2, or O_2 molecule on monolayer Ti_2CO_2[75].

Previously, theoretical studies on Ti_2CO_2, another member of the MXene family of materials, have suggested the potential of this material for sensing different gases[75]. By using first principles simulations, the adsorption of NH_3, H_2, CH_4, CO, CO_2, N_2, NO_2, and O_2 on Ti_2CO_2 was investigated, and it turns out that only NH_3 could be chemisorbed on Ti_2CO_2 with large absorption energy and charge transfer as shown in figure 2.7. Here, the absorption energy is defined as

$$E_{ads} = E_{Ti2CO2+Gas} - E_{Gas} - E_{Ti2CO2}$$

where $E_{Ti2CO2+Gas}$ is the total energy of monolayer Ti_2CO_2 adsorbed with gas molecule, E_{Gas} is the total energy of gas molecule, and E_{Ti2CO2} is the total energy of monolayer Ti_2CO_2. The same author also showed the interaction between NH_3 and other O-terminated MXenes (M_2CO_2, M=Sc, Ti, Zr, and Hf) by using fist-principle simulations as presenting the potential of MXenes for NH_3 sensor[76]. Very recently, Ma et al.[77] studied SO_2 adsorption on O-terminated M_2CO_2 (M=Sc, Hf, Zr, and Ti) by using first-principle calculation and demonstrated that Sc_2CO_2 is most preferable for SO_2 molecule. However, there has not been a focus on experimentally investigation regarding the gas sensing property of MXenes. Therefore, it is highly desirable to experimentally explore gas sensing property of MXene and study the mechanism by comparing with simulated results.
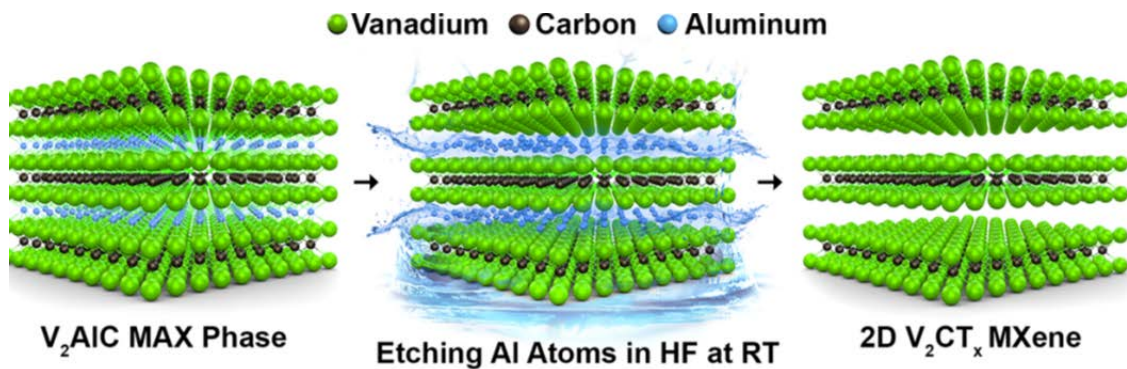
Figure 2.8. Schematic illustration of the selective etching process used to synthesize V_2CT_X MXene from V_2AlC MAX phase[78].

Another MXene material introduced for gas sensing applications was V_2CT_X MXene. V_2CT_X MXene can be obtained from the selective etching of V_2AlC MAX phase as other 2D MXenes. Figure 2.8 shows the schematic illustration of the etching process to synthesize V_2CT_X MXene from V_2AlC MAX phase. The 2D structure of V_2CT_X MXene consists of two layers of vanadium (V) atoms with a sandwiched conductive carbide layer. Through the etching process, the MAX phase of V_2AlC was exfoliated into 2D V_2CT_X MXene, leaving chemically terminated oxygen (O), hydroxyl (OH), and fluorine (F) on the surface. In practice, these surface functional groups are randomly distributed on the surface with at least three combinations of V_2CO_2, $V_2C(OH)_2$, and V_2CF_2, and non-terminated MXenes are yet to be synthesized. These surface terminations are highly dependent on the synthetic methods[74], however, a few of practical methods to control surface terminations of MXenes have appeared so far[79]. The hydrophilic nature of these active terminal groups on the surface of MXenes make them effective adsorbents of polar gases, ionic / non-ionic species, and metals, which consequently can be used for environmental pollutant purification or sensing[80]. The surface functionalities are strongly relevant to the physical and chemical characteristics of MXene materials, which further impacts the sensing properties. The hydrophilic surface is beneficial for the adsorption of polar or ionic species, the -O and -OH terminations are more favorable than -F groups. Fortunately, these oxygen containing groups are found to be more stable, and -F termination will be replaced by -OH groups upon rinsing and/or storage in water[80].
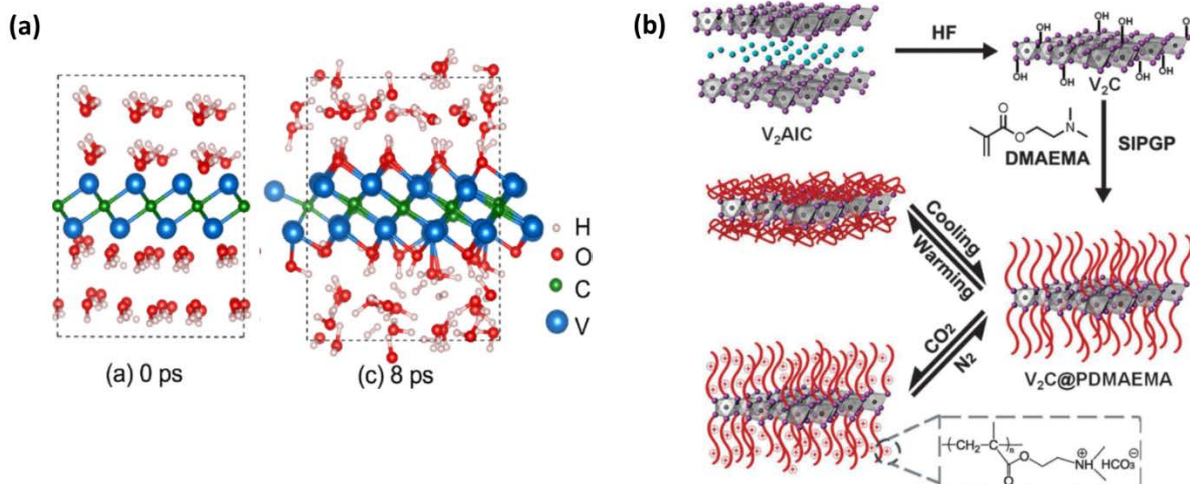
Figure 2.9. (a)Snapshot of a bare V_2C in water at 0 and 8 ps.[81] (b) Schematic of V_2C@PDMAEMA system[82]. (C denotes off-white, V denotes purple, and Al denotes blue)

Recently, theoretical insights into the metal adsorption on 2D V_2CT_X MXene reported with DFT and molecular dynamics (MD) simulations show an intriguing feasibility of V_2CT_X MXene for sensing applications[81]. Figure 2.9 (a) indicates that the -OH functional groups promptly attached on the surface of monolayer V_2C in water and the system became a stable state in about 2 ps. Theoretical study further revealed that Uranyl (U) adsorbates bond strongly with hydroxylated V_2C MXene by forming a U-O bond, which is more energetically favorable than U-F bonds with lower adsorption energy, suggesting that F terminated MXenes are less benign for adsorption applications. Further, grafting responsive poly(2-(dimethylamoni)ethylmethacrylate) (PDMAEMA) brushes on multilayered V_2CT_x was reported as a method to make MXenes-based hybrid materials with CO_2 and temperature dual-sensitivity as shown in Figure 2.9 (b)[82]. Based on the reaction of PDMAEMA with the CO_2 simulation, its conductivity underwent an uncharged-charged transition in aqueous solution. However, until now, there has been no experimental investigation on gas sensing properties of V_2CT_x MXene itself.

2.4. Investigation of hybrids consisting of 2D nanomaterials and metal oxides

Previously reported results have demonstrated promising potential of 2D nanomaterials for gas sensor application, but the experimental results on the sensing performance has not been as high as their theoretical values. Such discrepancy can result from the restacking or aggregating of nanosheets due to the electrostatic force between each layer, which influences a reduced gas response by depleting the number of reaction sites. Therefore, the strategies to prevent restacking of 2D layered materials are devised, including the formation of hierarchical structures[83-84], incorporation of nanomaterials, and novel metal doping[76, 85]. These methods provide improved sensitivity, but the sensors still have a deficiency in selectivity by responding to more than one analyte gas. A possible approach to improve selectivity is to design an electronic nose, an array of single chips to identify several gases simultaneously. In a single unit, decoration or doping of novel metals such as platinum (Pt), palladium (Pd), silver (Ag), and gold (Au), could be a reasonable solution to increase the selectivity via catalytic activities. The use of novel metals improves gas sensing performance by lowering the activation energy because of electronic sensitization and spill-over effects[86]. Some novel metals have a high affinity for specific gas species. Catalyzing the dissociation of O_2 subsequently spills out O^- ions onto the surface of the metal oxide, which results in an increased response and faster reaction time[87]. However, the cost of novel metal and its catalytic poisoning largely offset its merit. Not only selectivity and response, but also long-term stability of the 2D materials sensor is another critical issue. When 2D nanomaterials are tightly bound with oxygen molecules in ambient atmosphere, their sensing properties have not been maintained for extended periods of time[88-89]. To overcome the problem, the application of external

30

energy such as thermal energy or UV energy was attempted to eliminate oxygen molecules by breaking their bonds[90]. As an alternative approach to enhance selectivity and sensitivity for an array, the integration of 2D materials with metal oxides can be considered for multiple benefits. This combination may solve several challenges including sensitivity, selectivity, and stability issues. Based on the material features of TMDs and metal oxides, the advantages and disadvantages of each material for gas sensing applications are listed in table 2.5.[91]

Table 2.5. Advantages and disadvantages of metal oxide and GO sensor performance.

	Metal oxide	Graphene oxide
Advantages	Short response time Low cost Long-term stability Scalable fabrication	High electron mobility at low temperature Low energy consumption High gas response at low temperature Light Good compatibility Mechanical flexibility
Disadvantages	Low electron mobility at low temperature High operating temperature High power consumption Low gas response at low temperature	Low selectivity Sluggish recovery Deficient long-term stability Lack of scalable fabrication Relatively high cost

It should be noted that these advantages and disadvantages of each classification are not absolute for either category. Rather, they are comparative features that provide reasonable options when designing a gas sensor. Even though gas response of GO normally higher than that of metal oxide sensor, it should be improved more to the range of ppb considering medical applications. To improve gas response, typical approach is to enlarge specific surface area in which they react with target molecules by tailoring morphology of sensing materials. Long-term stability is another unsolved problem of GO sensor. Due to chemically reactive oxygen functional groups of GO, GO easily oxidize in ambient atmosphere resulting in long-term instability. To improve long-term stability of GO, oxygen-containing functional groups of GO is controlled through chemical or thermal reduction processes. By adjusting functional groups, lifetime can be extended at the expense of gas response.

With their combination, the agglomeration of 2D nanosheets can be avoided. The resulting porous structure exposes much more surface of GO, providing a higher chance to interact with gas molecules. More importantly, the hybrid nanostructure can enhance the gas sensing performance by organizing a heterojunction at the interface between the two materials with a creation of either an n-/p-type nanostructure or an n-/n-(p-/p-) type structure. Since GO has the bandgap unlike graphene, bandgap of the composite can be engineered. After building contact between two semiconducting materials, the Fermi levels across the interface will be equilibrated to the same energy state. Charge carriers will be transferred, and depletion or accumulated layers will be generated at a heterojunction. Thereupon, electrical features of the hybrids can be tuned toward the significant improvement of gas sensing properties. The collective benefits of TMDs and metal oxides hybridization can be broken down into three general aspects: geometrical effects, electronic effects, and chemical effects[29]:

32

- Geometrical effects

  - The construction of a hierarchical structure prevents the agglomeration or restacking of 2D GO nanosheets or metal oxides, which enlarges the active surface area for reaction with analytes.

  - The porous and controlled nanostructure by the incorporation of metal oxides to 2D GO during the synthesis facilitates gas absorption and diffusion corresponding to fine-tuning of the metal oxide gas response.

- Electronic effects

  - The potential energy barrier and charge carrier depletion zone at the heterojunction can be modulated by gas adsorption and desorption to act as additional reaction sites.

  - The built-in internal electric field formed at the interface promotes additional oxygen adsorption and charge carrier's conveyance.

  - The depletion zone of charge carriers at the heterojunction acts as a passivation layer to prevent the interaction between oxygen and GO.

- Chemical effects

  - The chemical bonds created between 2D GO and metal oxides can act as efficient charge transport bridges during the gas sensing process.

  - The density of chemisorbed oxygen on the surface of metal oxides can be increased by the interfacial chemical bonds.

  - The receptor function of metal oxides can improve selective adsorption of analytes.
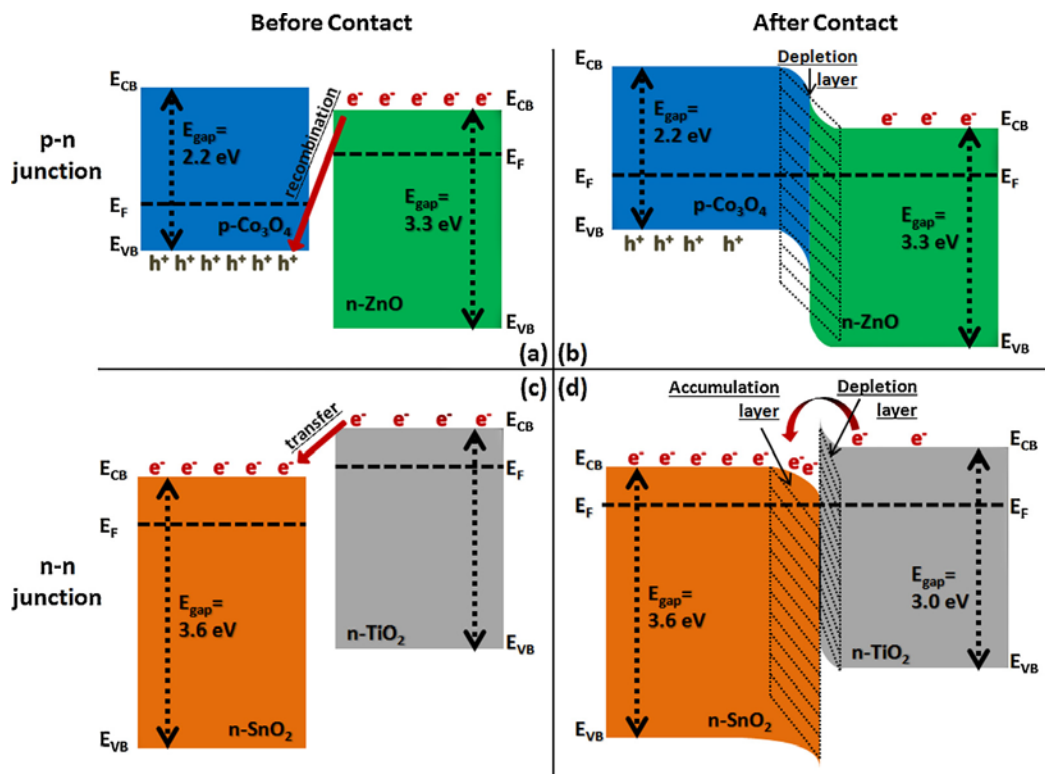
Figure 2.10. The schematic diagram of band bending of metal oxide at heterojunction. (a,b) p-n junction before/after contact. (c,d) n-n junction before/after contact.

Predicated upon these synergistic effects, the hybrids can be considerably developed. Figure 2.10 shows the schematic diagram of the bending of metal oxide at the heterojunction to help understanding. Table 2.7 shows the summary of gas sensing condition of GO/metal oxide nanocomposite and effects of hybridization on sensing performance. Various metal oxides such as tin oxide (SnO_2), zinc oxide (ZnO), and iron oxide (Fe_2O_3) with various nanostructures have been incorporated to 2D GO by hydrothermal or layer by layer method. Sensing temperature of the composites vary from RT to 280°C, depending on the dominant sensing materials as a function of the amount of insulating metal oxides. When compounding GO and metal oxide, the ratio of the

composite is an important factor to determine working temperature. If a small amount of metal oxide was decorated on GO, GO is the assertive sensing material, and metal oxide supports to enhance the performance. On the contrary, if metal oxide would be the main sensing material, working temperature of the composite should be higher than that of GO owing to the insulated property of metal oxide at RT. Accordingly, sensing type to target gas is also dependent on the predominant sensing materials. It is well known that reduced GO shows p-type sensing behavior to reducing gases such as NH_3, NO_2, and methanol. As shown in table 2.6, the composite exhibits p-type sensing behavior to reducing gases at RT and n-type sensing behavior at high temperature as suggesting n-type metal oxide reacts with gas molecules. Furthermore, target gases are diversified to ethanol, methanol, and acetone as well as NH_3, and NO_2, which propounds that GO-based sensor can be employed as multi-purpose sensor. Notably, the impacts of the hybridization on sensing performance were collected in table 2.7. Through the incorporation, RT sensing was enabled, gas response and selectivity were increased, and response and recovery time was reduced. Yet, few reports have been studied of GO and TiO_2 composite to date, and there is no clear answer as to which electrical modification corresponds to each specific performance improvement. The relationship between the modified properties and the enhanced performance should be more clearly defined in terms of electronic or chemical mechanisms.

Table 2.6. Literature survey of gas sensing condition of GO/metal oxide nanocomposites and their sensing performances.

Ref	Materials	Structure	Working temp	Analyte	Sensing behavior	Concentration	Gas response ($\Delta R/R_a$)	Effects
[92]		Hydrothermal	RT	NH_3	P type	10 ppm	6%	RT sensing Sensitivity↑
[93]	$rGO+SnO_2$	Hydrothermal	30-60°C	NO_2	P type	5 ppm	3.31	Response↑ Selectivity↑ Reproducibility↑
[94]		Hydrothermal	RT	Acetone	P type	10 ppm	2.19%	Response↑
[95]		Reflux	150°C	H_2	N type	200 ppm	3.5	Operable temperature↓ Response↑
[96]	$rGO+ZnO$	In situ	RT	NO_2	P type	1 ppm	13.1%	Sensitivity↑ Response and recovery time↓
[97]		Hydrothermal	RT	NH_3	P type	10 ppm	1.5%	Sensitivity↑ Selectivity↑
[98]	$rGO+TiO_2$	Thermal treatment	RT	NH_3	P type	10 ppm	0.65	Sensitivity↑ Selectivity↑
[99]	$rGO+WO_3$	Layer	RT	NO_2	P type	1 ppm	1.96	Sensitivity↑ Response and recovery time↓
[100]	$rGO+Co_3O_4$	Hydrothermal	RT	Methanol	P type	300 ppm	4%	Sensitivity↑ Response and recovery time↓
[101]	$rGO+\alpha Fe_2O_3$	Hydrothermal	280	Ethanol	N type	1000ppm	30%	Sensitivity↑

3.1. Device fabrication

3.1.1. Substrates preparation
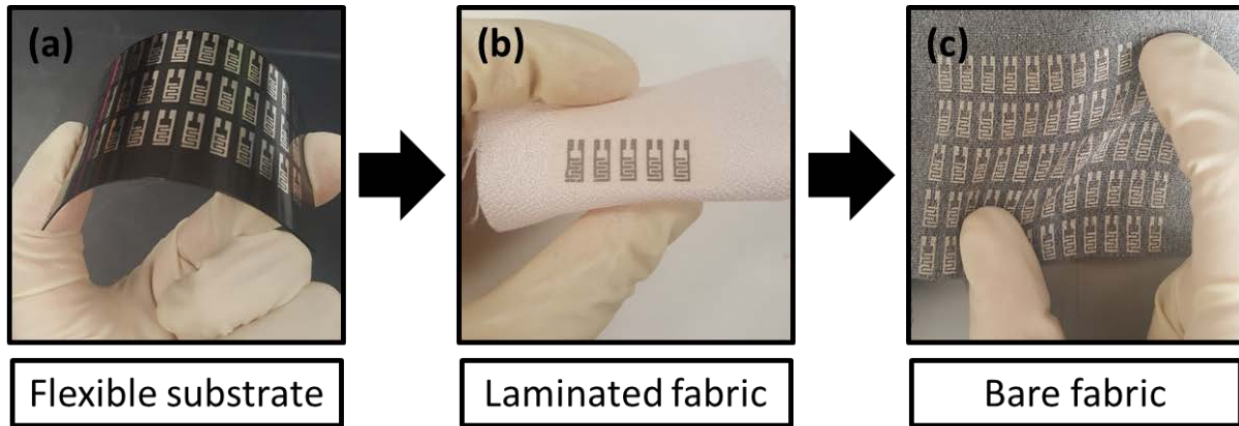
Figure 3.1. Images of (a) flexible substrate (polyimide film), (b) laminated polyester fabric, and (c) bare polyester fabric.

Three different types of substrates have been utilized to build sensor devices as shown in figure 3.1. Flexible substrates, laminated fabrics, and bare fabrics were used as wearable sensor platforms. First, nylon plate, polyimide film, and cotton paper were selected as flexible substrates, which are bendable, but not wearable. Second, laminated fabrics were adapted as an intermediate step prior to bare fabric. By laminating the porous surface of fabrics, conventional electrode fabrication processes could be applied. Last, bare fabrics such as nylon, polyester, and cotton were employed as wearable substrates without surface treatment. Due to low thermal resistance and corrosive

resistance of garments, low-temperature and non-corrosive processes should be utilized to manufacture interdigitated electrodes.

(a) Flexible substrates

For the fabrication of gas sensing devices, nylon plate, polyimide film, and cotton paper were utilized as flexible substrate. The flexible substrates (except cotton paper) were immersed in 99.9% of liquid ethanol and then in DI water and subsequently were subjected to ultra-sonication (Brason, 3510) to remove contaminants from their surface. After the cleaning, substrates were dried with an air gun.

(b) Laminated fabrics

Pure woven nylon, polyester, and cotton fabrics (Fabric.com Inc.) with 15 µm thread width were immersed in deionized water for cleaning and dried overnight in normal atmosphere. Thin PVC film was then coated on the prepared fabric by ironing to laminate porous surface of the fabrics for 30 sec.

(c) Bare fabrics

Ripstop type of woven nylon, polyester, and cotton fabric (Fabric.com Inc.) were immersed in deionized water for cleaning and dried overnight in normal atmosphere.

3.1.2. Electrode fabrication

Once substrates were chosen, conductive electrodes should be patterned on the substrates to measure the electrical signal of the sensing materials. Three different methods to fabricate electrodes were introduced including sputtering, silk-printing, and embroidering.

(a) Sputtering
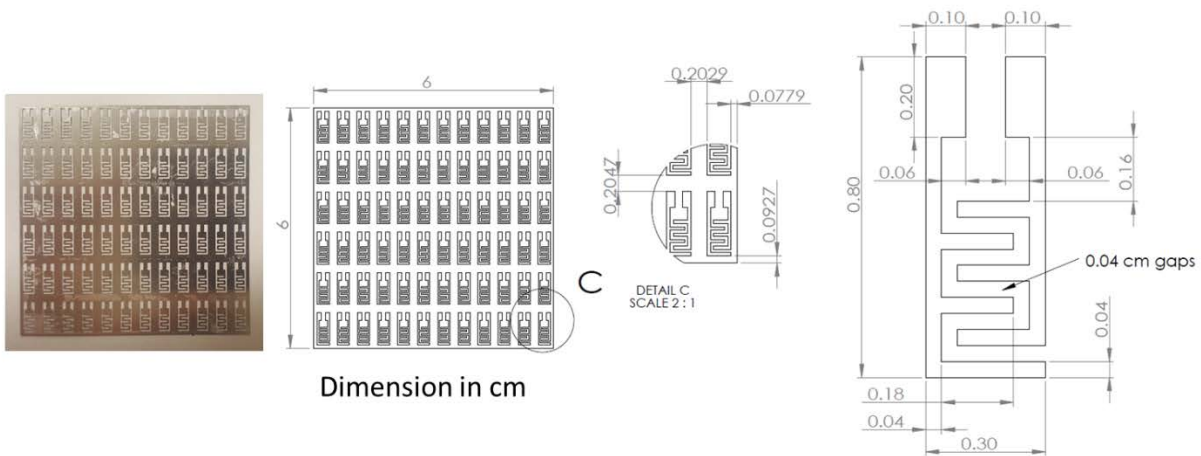
Figure 3.2. A shadow mask of interdigitated electrodes arrays.

The interdigitated electrodes, which were designed to enlarge the surface area in same dimension resulting in larger conductivity, were utilized to pattern on substrates to measure the resistance of sensing films. The arrays of electrodes with a size of 8 x 3 mm were engraved on stainless steel with a 400 μm interdigitated gap between electrodes. A stainless-steel shadow mask of interdigitated electrodes with a detailed size are shown in figure 3.2.
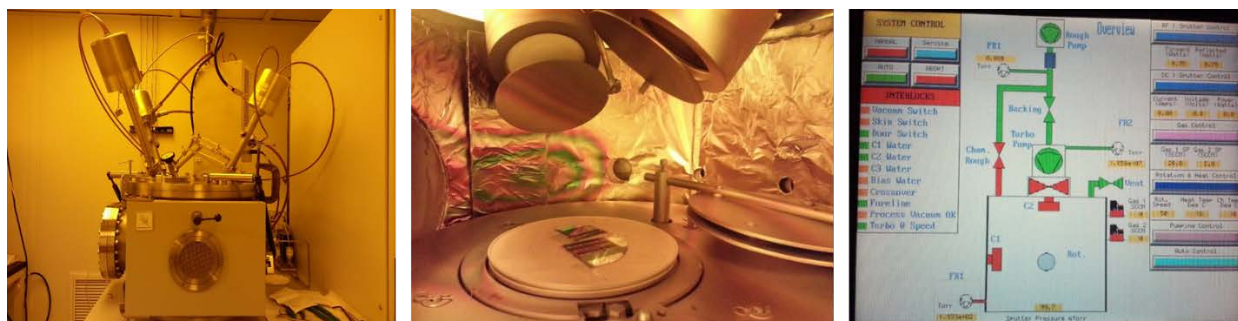
Figure 3.3. Denton Discovery 18 RF/DC sputtering system.

The prepared substrates were placed inside of the magnetron-sputter chamber (Discovery 18, Denton Vacuum) as described in figure 3.3. Pt target (Lasker, 99.9 %) was used as the electrode material due to its good electrical conductivity and resistance to be oxidized. When an adhesion layer is required, Ti (Lasker, 99.9%) or Cr (Lasker, 99.9%) target should be setup as well as Pt target. Once the chamber pressure became below $2 * 10^{-5}$ mTorr, the system is ready to perform the sputtering. Adhesion layer of Ti or Cr was sputtered first in radio frequency (RF) sputter with around 10nm thickness. Then, Pt was sputtered in direct current (DC) with a thickness of around 100nm on the substrates. (Detailed sputter condition was summarized in table 3.1)

Table 3.1. Sputter deposition conditions for material preparations.

	Power type	Power (W)	Time (sec)	Estimate thickness (nm)	Ar (sccm)	O_2 (sccm)	Working pressure (mTorr)
Pt	D.C.	100	360	100	25	0	4.3
Ti	R.F.	400	25	10	25	0	4.3

(b) Silk printing

Interdigitated electrodes with the same dimensions were printed by silk printing on bare fabrics where silver paste was utilized as a printing material After printing electrodes, the fabrics were dried in ambient atmosphere.

(c) Embroidering
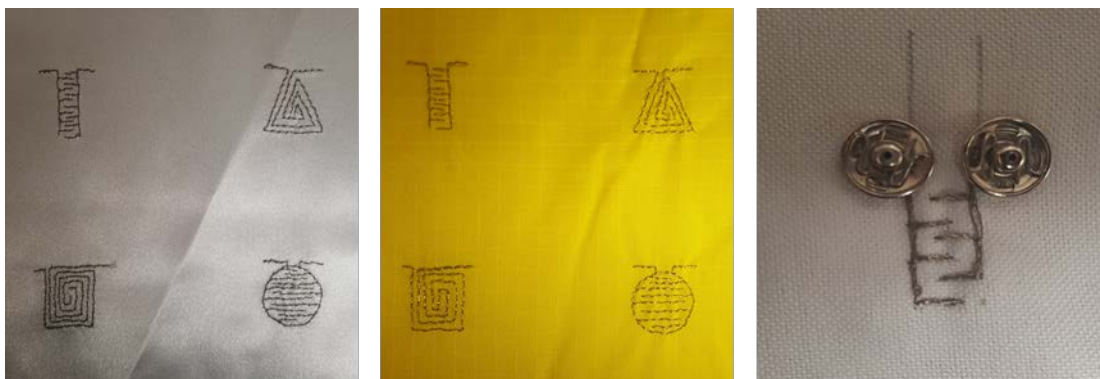
Figure 3.4. Various shapes of electrodes embroidered in polyester (white saint), nylon (yellow ripstop), and cotton (white)

Various shapes of electrodes were embroidered in bare fabrics such as polyester, nylon, and cotton in figure 3.4. Conductive sewing thread (117/17 2ply, Shieldex, U.S.) was used for making conductive paths in garments and textiles.

3.2. Synthesis of sensing materials

3.2.1. Graphene oxide (GO)

Graphene oxide (GO) was commercially available from ACS materials. Graphene oxide was prepared by a modified Hummers' method and was distributed in D.I water. Typical flake size was 0.5-2.0 μm with thickness raining from 0.6 to 1.2nm. Aqueous GO dispersion with 10mg/ml was created and then sonicated for 30min. This dispersion was used to deposit GO films. Two dispersions using 10 mg of commercial single layer GO powder (Cheap Tubes Inc.) were made in 10 ml of deionized water and 99.9 % ethanol respectively. The dispersions were sonicated for 30 min to be uniformly dispersed.

3.2.2. Molybdenum disulfide (MoS$_2$)

Monolayer Molybdenum disulfide (MoS$_2$) powder was purchased from ACS materials. Molybdenum disulfide was prepared by a lithium-based intercalation method and dispersed in D.I water with a concentration of 5 mg/ml. The diameter of the flake ranges from 0.2μm to 5μm with a thickness around 1 nm. The aqueous solution of MoS$_2$ was hand-shaken or sonicated for 10 min for uniformity, and then was deposited.

3.2.3. Titanium carbide (Ti$_3$C$_2$T$_x$)

Figure 3.5. Schematic illustration of Ti$_3$C$_2$T$_x$ synthesis procedure.

Dispersions of delaminated Ti$_3$C$_2$T$_x$ in water were prepared through a method previously reported in the literature[71]. In short, 1 g of Ti$_3$AlC$_2$ powder (with an average particle size of less than ～32 μm) was etched in a mixture of 9 M HCl and LiF (～1 g) at 35 °C for 24 h. The etched particles were washed with deionized water (DI) several times and centrifuged until the pH of the supernatant was above 5. The resulting powder was collected, and probe sonicated in deaerated DI water for 30 min as shown in figure 3.5. The obtained solution was centrifuged at 3500 rpm for 1 h, and the resulting black supernatant (referred to as d-Ti$_3$C$_2$T$_x$ solution) was collected for further analysis and sensor fabrication. For deposition of Ti$_3$C$_2$T$_x$ films, a dispersion of Ti$_3$C$_2$T$_x$ in water with a concertation of 0.19 mg/mL was sonicated for 30 min.

3.2.4. Vanadium carbide (V_2CT_x)

Single/few-layers V_2CT_x MXene dispersions were prepared by delamination of multilayered (ML) V_2CT_x particles according to previous reports in the literature[78, 102]. Initially, V_2AlC MAX phase powder was etched in 50% hydrofluoric (HF) acid (ACS grade, BDH) for 92h at room temperature. After the etching process was complete, the powders were washed several times with DI water until the pH of the supernatant was above 4. Then the etched powders were collected by filtration and dried under vacuum at RT over the night. The obtained multilayered MXene particles did not delaminate directly even with sonication[103-104]. The delamination process was done by intercalation of MXene particles with tetra-n butyl ammonium hydroxide (40% w/w aqueous solution of TBAOH, Alfa Aesar) for 4h at RT (200 mg MXene to 4 mL TBAOH solution). The intercalated powders were delaminated by adding DI water and handshaking for 2 minutes. The resulting dispersion was centrifuged at 2000 rpm for 10 minutes to separate the delaminated MXenes from any residual MAX phase particles. After the centrifugation, the resulting supernatant (labeled as d-V_2CT_x) was collected and used for further characterization and device fabrication.

3.2.5. Graphene oxide / Titanium dioxide (GO/TiO₂) hybrids

Figure 3.6. Schematic illustration of GO/TiO₂ nano-composite synthesis procedure.

GO powder (0.5 - 2.0 μm, ACS Materials Company) with 50 mg was dispersed in 15 mL ethanol and stirred for 30 minutes. The GO solution was mixed with 2.5 mM of TiO₂ nanoparticles (size < 21 nm, a mass fraction of 80 % anatase / a mass fraction 20 % of rutile, Sigma-Aldrich) and stirred until the mixed nano-powder was completely dispersed in ethanol. After vigorous sonication, the solution was irradiated by UV (ELC-500 UV curing chamber, 30W/cm^2) for 2 hours as shown in figure 3.6.

3.3. Deposition of sensing materials

To deposit sensing materials on the prepared sensor platform, drop casting is mostly utilized. Using a syringe or disposable pipet, a droplet of the uniformly dispersed suspension was dropped onto the interdigitated electrodes and dried overnight at ambient atmosphere.

3.4. Materials characterization

The JEOL JSM-7000F scanning electron microscope (SEM) equipped with an energy dispersive spectrometer (EDS) and an optic microscope (Olympus BX51) were utilized to observe the morphology of the synthesized nanomaterials. For TEM sample preparation, a dual beam focused ion beam (FIB) was utilized, and the materials were imaged using a Tecnai G2 F30S-Twin transmission electron microscope (AP Tech) equipped with EDAX analyzer (DPP-‖) at 300kV. Ultraviolet–visible (UV-vis) spectra was employed to characterize optical property of the material (Ultra spec 2100 pro, Harvard Bioscience, Inc.) in a specific range. Structure and surface condition of the composite were investigated using an X-ray diffractometer (XRD, Bruker D8 Discover) equipped with LYNXEYE™ technology at 40 kV and 40 mA Cu-kα radiation at a scan speed of 2 seconds per step. XPS was carried out by K-alpha (Thermo Scientific Inc., U.K) having a 180° double focusing hemispherical analyzer with a 128-channel detector. Under the vacuum of 4.8×10^{-9} mbar, monochromatic Al X-ray were exposed with a step size of 1eV in a sampling area of 400μm diameter range. Surface bonding of the sample was investigated using Fourier transform infrared spectroscopy (FTIR) with PerkinElmer spectrum 100 ATR-FTIR spectrometer and a resolution of 4 cm^{-1}. Atomic force microscopy (AFM) measurements were carried out using Park Instruments NX10 AFM in non-contact mode to study surface morphology of the film. The room-temperature micro Raman system is homemade which is equipped with a Jobin Yvon spectrometer and a thermal electrically-cooled charge coupled device (CCD) detector (2048 pixels by 512 pixels.) The Raman spectroscopy was carried out in back scattering geometry using 441.563 nm line (80 mW) from a He-Cd laser.

Table 3.2. XRD specification.

Wave length	Range	Step size	X-ray
1.54 A	5 ~ 80 °	0.25	40kV/40mA

3.5. Measurement of gas sensing properties
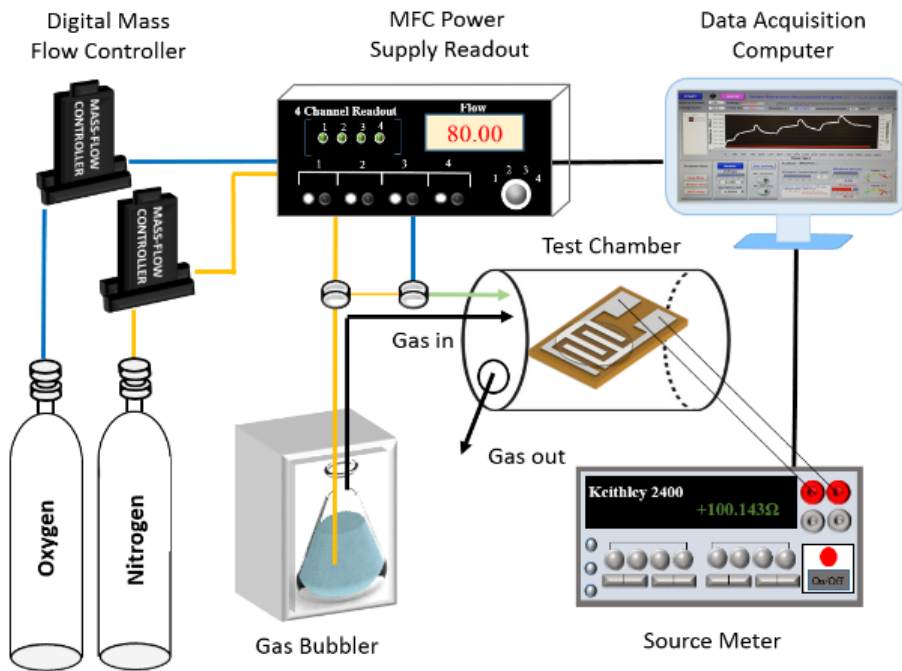
Figure 3.7. Schematic diagram of the gas sensing experiment setup (bubbling).

Figure 3.7 shows the gas sensor characterization system. Two types of dry gas, i.e. oxygen and nitrogen, were used to generate synthetic air. The amount of synthetic air was controlled by using mass flow controllers (MKS1179A, MKS Instruments, Andover, MA, USA). The synthetic

air was comprised of 80sccm of nitrogen and 20sccm of oxygen. 20sccm of oxygen was injected into the test chamber and 80sccm of nitrogen gas was split in half. Half of nitrogen gas was introduced into the gas bubbler as a target gas carrier, and the other half nitrogen was directly entered into the test chamber. The nitrogen gas carrier is bubbled through the liquid analyte of interest for producing the target gases and subsequently mixed with the synthetic air in the test chamber. Before introducing target gas, the initial resistance of the sample was measured under synthetic air condition. After stabilization of the sensor's resistance signal, a target gas was introduced into the gas chamber.
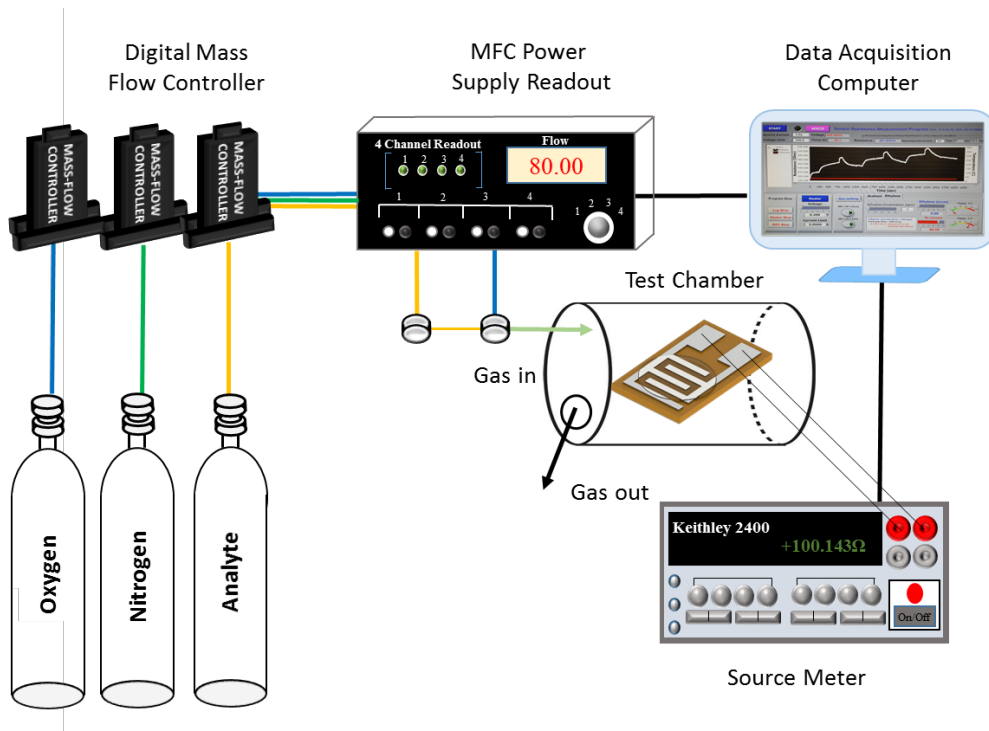
Figure 3.8. Schematic diagram of the gas sensing experiment setup (vapor injection).

Figure 3.8 shows the gas sensor characterization system. Two types of dry gas, i.e. oxygen and nitrogen, were used to generate synthetic air. The amount of synthetic air was controlled by using mass flow controllers (MKS1179A, MKS Instruments, Andover, MA, USA). For the target gas injection, the total gas flow was fixed to 100sccm by combing three gases; pure nitrogen (MFC 1), pure oxygen (MFC 2), and target gas diluted in nitrogen (MFC 3). The amount of oxygen was fixed to 20sccm during the synthetic air and analyte injection, and amount of pure nitrogen and analyte was adjusted with an analyte concentration by the following Eq. (5).

$$C_{analyte}(ppm) = \frac{C_{gas} * MFC\ 3}{MFC\ 1 + MFC\ 2 + MFC\ 3} \text{ Eq. (5)}$$

For 200 ppm of acetone gas concentration ($C_{analyte}$), 40 sccm of pure nitrogen (MFC 1), 20 sccm of pure oxygen (MFC 2), and 40 sccm of acetone diluted nitrogen (MFC 3), with the 500ppm concentration (C_{gas}), were injected. The resistance change of the sensor was measured by a Keithley 2400 source meter. Two conductive pads on the interdigitated electrode were used to extract the signal, and the data acquisition was controlled with a customized Labview program. The resistance of the sample was recorded in the presence or absence of the target gas under the continuous synthetic air atmosphere. The gas response was calculated as the ratio of $|R_a\text{-}R_g|/R_a$, where R_g is the resistance of the film under the target gas, and R_a is the resistance of the film under the ambient air.

Class	General Formula	Example	Common Name (Systematic Name)	Common Suffix/Prefix (Systematic)
Hydrocarbons				
Alkanes	RH	CH_3CH_3	ethane	-ane
Alkenes	RR'C=CR''R'''	$H_2C=CH_2$	ethylene (ethene)	-ene
Alkynes	RC≡CR'	HC≡CH	acetylene (ethyne)	(-yne)
Arenes	ArH[a]		benzene	-ene
Halogen-Containing Compounds				
Alkyl halides	RX	CH_3CH_2Cl	ethyl chloride (chloroethane)	halide (halo-)
Aryl halides	ArX[a]	—Cl	chlorobenzene	halo-
Oxygen-Containing Compounds				
Alcohols	ROH[a]	CH_3CH_2OH	ethyl alcohol (ethanol)	-ol
Phenols	ArOH[b]	—OH	phenol	-ol
Ethers	ROR'	$H_3CH_2COCH_2CH_3$	diethyl ether	ether
Aldehydes	RCHO	CH_3CH (O)	acetaldehyde (ethanal)	-aldehyde (-al)
Ketones	RR'C=O	CH_3CCH_3 (O)	acetone (2-propanone)	-one
Carboxylic acids	RCO_2H	CH_3COH (O)	acetic acid (ethanoic acid)	-ic acid (-oic acid)
Carboxylic Acid Derivatives				
Esters	RCO_2R'	CH_3COCH_3 (O)	methyl acetate (methyl ethanoate)	-ate (-oate)
Amides	RCONHR'	CH_3CNHCH_3 (O)	N-methylacetamide	-amide
Nitrogen-Containing Compounds				
Amines	RNH_2, RNHR', RNR'R''	$CH_3CH_2NH_2$	ethylamine	-amine
Nitriles	RC≡N	$H_3CC≡N$	acetonitrile	-nitrile
Nitro compounds	$ArNO_2$[a]	—NO_2	nitrobenzene	nitro-

[a]R indicates an alkyl group [b]Ar indicates an *aryl* group.

Figure 3.9. Common functional groups in organic chemicals.[105]

Gas sensing properties were analyzed with various organic chemicals. Figure 3.9 shows the classification of organic chemical in terms of common functional groups. Organic chemicals can be sorted by functional groups, which are responsible for the chemical characteristic. The chemicals in same functional groups will undergo similar chemical reaction with sensing materials.

50

In the group of hydrocarbons, methane gas was utilized as typical chemical compound with the chemical formula CH_4 in the class of alkane. Methane has strong equivalent C-H bonding, and it is flammable. In oxygen containing groups, ethanol and methanol were selected in the class of alcohols, and acetone was employed as a representative of ketones. Ethanol is a simple alcohol with the chemical formula C_2H_5OH, and it is volatile and flammable. Methanol, also known as methyl alcohol (CH_3OH), was chosen another chemical in alcohol group with methyl radical. Its characteristic is similar to ethanol, but it is highly toxic and improper for consumption. Acetone is volatile, flammable liquid with a simple formula of $(CH_3)_2CO$. In nitrogen-containing compounds, ammonia with the formula NH_3 was used in the class of amines due to its flammability.

Chapter 4. Process Engineering to Integrate Sensors Device on Wearable Substrates

4.1. Introduction

As the demand of flexible and wearable electronics has surged, much research in the field of gas sensor has been focused on wearable gas sensors. With the addition of wearability, the sensor systems can be used in clothing not only to identify atmospheric attacks as a protective device, but also to measure emitted gases from human breath as a health monitoring system[106]. For example, a wearable gas sensor could easily be worn by soldiers or fire fighters who are exposed to harsh environments to protect themselves and by chronically ill patients who need to care for their health continuously. Fabric is the most desirable platform for wearable gas sensors among many flexible alternative candidates such as paper [39] and polymer film[107], since its flexibility and light weight make it viable for various human activities[11]. Typically, polyester and nylon are the in highest demand for synthetic fabrics, while cotton is in highest demand for natural fabric. Each fabric has its own physical and chemical properties depending on the source and structure so deciding on a fabric type and pattern is a crucial when designing wearable electronics. Despite these tremendous advantages of fabric construction, there many challenges for the realization of wearable electronics due to several technical limits. One of main challenges of the smart fabric technologies is the lack of mass availability of components which creates high costs. One unique issue for manufacturing sensors onto textiles include the porosity and roughness of different fabrics. To overcome this, sophisticated manufacturing processes such as embroidery and soldering or pre-treatment like lamination, should be required to integrate electronics on fabric[19-20]. The

52

development of textile circuitry, which is the technique to fabricate circuits on fabrics, is an essential part of a smart fabric technology, and finding suitable garments and manufacturing methods is the first step to commercialize wearable electronics[9].

4.2. Electrode preparation on wearable substrates

Fabric was employed as a new senor platform, and nylon, polyester and cotton fabrics with same woven pattern were used as typical fabrics. Since woven fabric has a complex structure with porosity, integration electronics on fabric demands greater challenge[108]. To overcome this technical limit, we effort to construct electronics on fabrics by tailoring the surface of the fabrics. By laminating the surface of woven fabrics, the pores were covered, and rough surface was leveled as firmly connecting electrode circuit.
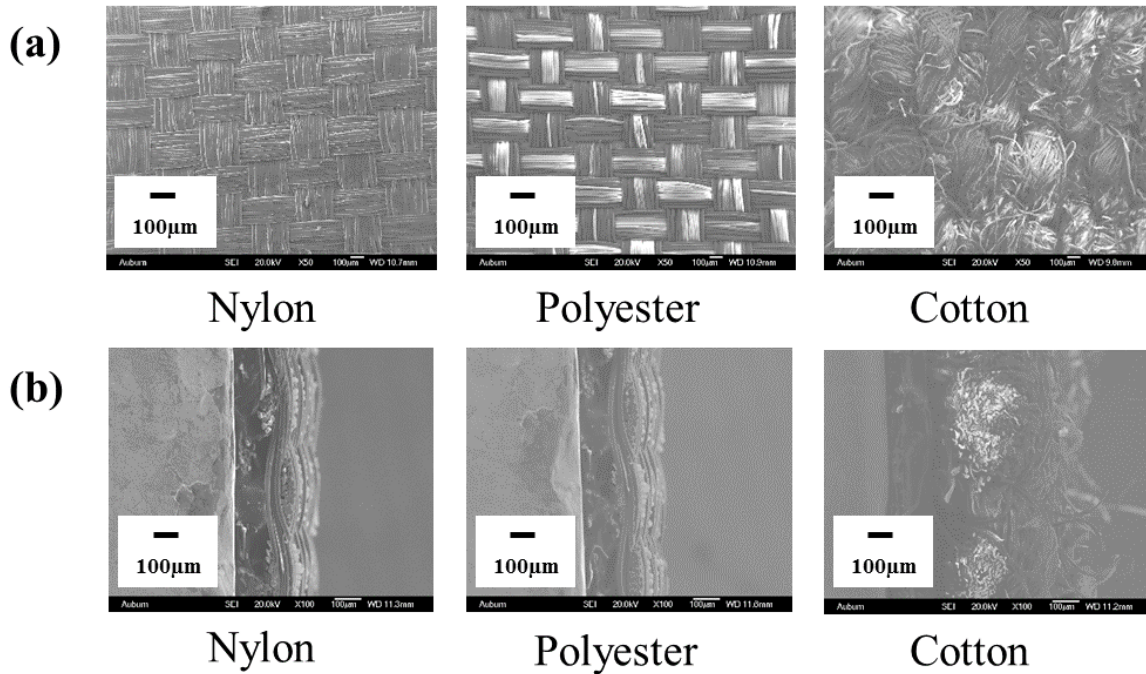
Figure 4.1. SEM images of bare nylon, polyester and cotton fabrics with same weave pattern in (a) face view (b) side view.

Top and side views of bare nylon, polyester and cotton fabric were observed by SEM in figure 4.1. Three types of fabrics were woven by 17 µm thick threads with the same Ripstop pattern in crosshatch. Synthetic fabrics such as nylon and polyester had a more organized pattern compared to natural fabric, whereas the cotton fabric was patterned with more hairiness due to its intrinsic properties. Relative roughness of the surface of the three different fabrics was compared in figure 4.1 (b). The side view of cotton fabric shows the cross section of ruggedly woven threads with more spaces compared to nylon and polyester fabric.
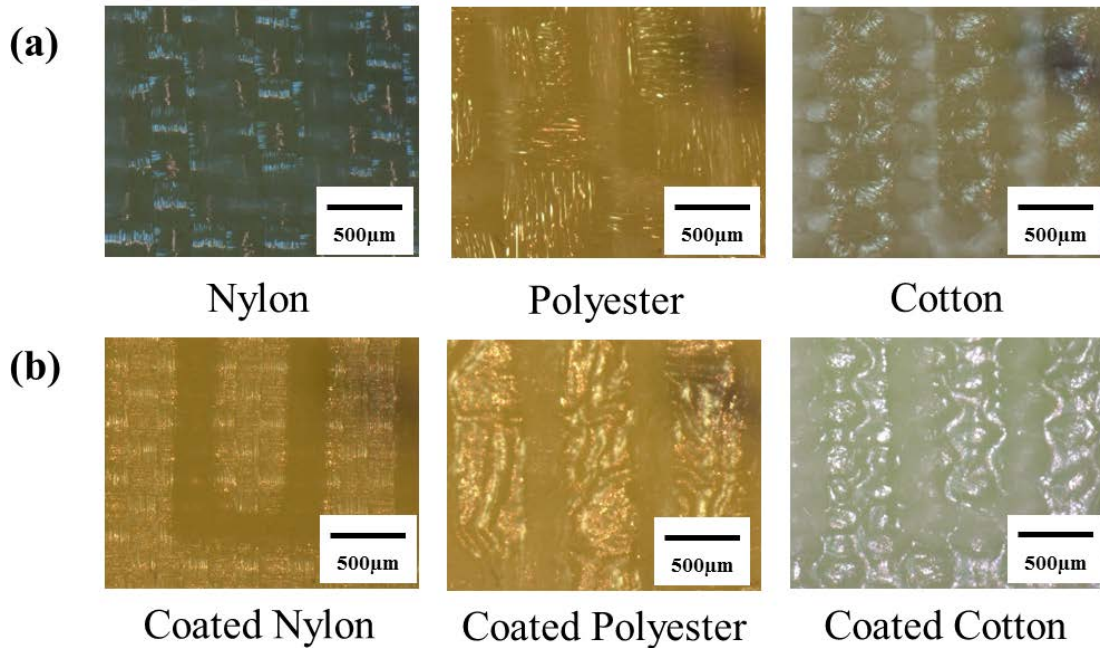
Figure 4.2. Optic microscopic images of the interdigitated electrodes on (a) bare fabrics (b) PVC coated fabrics.

Figure 4.2 shows the optic microscopic images of the sputtered interdigitated electrodes on bare and PVC coated fabrics. Interdigitated electrodes were well patterned on bare nylon and polyester fabrics with a 400 µm gap. The electrode was disconnected on cotton fabric due to its rough surface. As shown in Figure 4.2 (a), the patterned electrodes were influenced by the surface roughness of the fabrics, and rough fabrics resulted in the failure of electrode connection. To overcome the surface roughness issue, thin PVC film was coated on top of the fabrics and then the electrodes were sputtered with interdigitated pattern. Sputtered electrodes were clearly defined on all coated fabrics after thin PVC film was laminated on uneven woven pattern of the fabrics because the surface roughness became relatively flat.
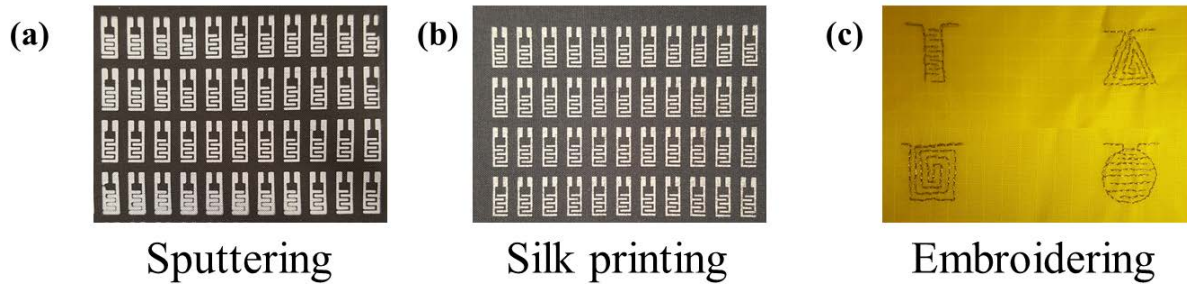
Figure 4.3. Photography of electrodes on bare fabrics. (a) interdigitated electrodes sputtered on nylon fabric, (b) interdigitated electrodes silk-printed on cotton fabrics, (c) various shapes of electrodes embroidered on polyester fabric.

Figure 4.3 shows photographic images of various shapes of electrodes on bare fabrics manufactured by sputtering, silk-printing, and embroidering. Interdigitated electrodes were patterned on bare nylon fabrics with a 400 µm interdigitated gap. Due to contact issues between the stainless-steel shadow mask and the fabric, the blurred electrodes were sputtered normally at edge of the fabrics. Another low-temperature process to produce electrodes on fabric is silk-printing. Using silver paste, interdigitated electrodes were clearly printed on bare cotton fabrics as shown in figure 4.3 (b). It is worthwhile to highlight micro-scale electrodes were printed on cotton fabrics by low temperature process without surface lamination. Embroidering was further processed to produce various shapes of electrodes on bare polyester fabrics in figure 4.3 (c). Conductive sewing thread was used for making conductive paths in garments, and its connection was well maintained when measuring resistance.

Through the exploration of various low-temperature processes, and the benefits and limitations of each process were summarized in table 4.1. Silk printing is a straightforward manufacturing process to deposit electrode on fabric. However, its scale is not proper to nano-sized electronics and it tends to brittle after curing. Sputtering is typical process of physical vapor deposition (PVD) and it is suitable for miniaturized electronics due to its high resolution. The use of nozzling has the benefit of automated system, but the limitation of synthesizing ink and endurance. Embroidering needs to be craft, but it gives the most flexibility.

Table 4.1. The summarized benefits and limitations of fabric circuit techniques.[9]

	Benefits	Limitations
Silk printing	Straightforward manufacturing	Micro-scale Tendency to brittleness
Sputtering	High resolution for miniaturized electronics	Specific fabrication environment
Soldering	No need pretreatment	Comfortless, Design
Nozzle	Automated process	Delicate to synthesizing ink Endurance
Embroidering	Flexibility	Need to be crafted

4.3. Deposition of sensing materials on wearable substrates
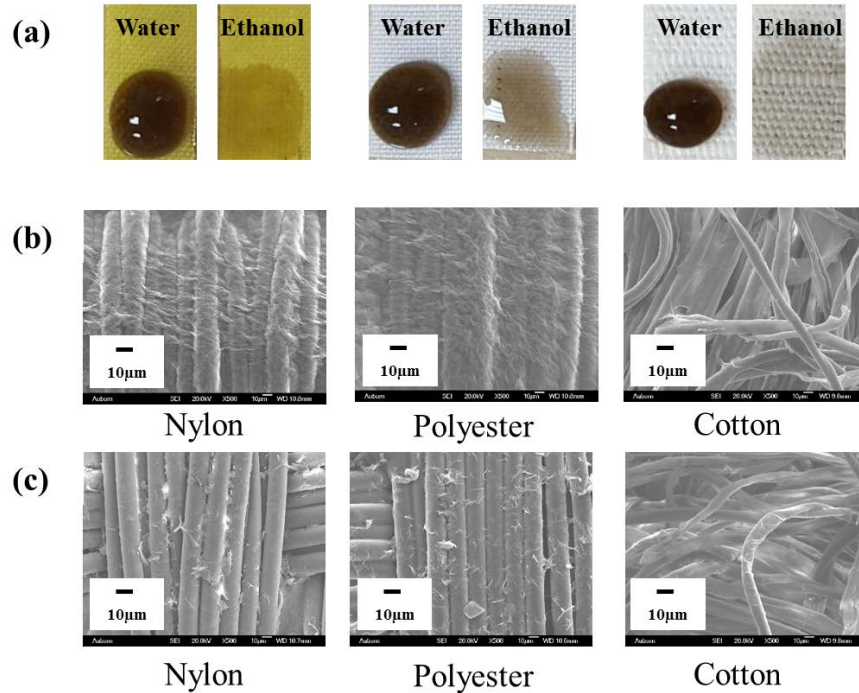
Figure 4.4. (a) The photographs of one drop of GO solution dispersed in water and ethanol on nylon, polyester and cotton fabrics. SEM images of dried GO dispersed in (b) water, (c) ethanol.

Figure 4.4 shows the effect of GO solvent on coating behavior. When considering the structure of fabric, the interaction between solution and substrate will be a critical factor in the solution deposition method. In our experiment, water and ethanol are compared as solvents to disperse GO nanoflakes, and the same amount of GO powders were distributed. As shown in figure 4.4 (a), water-based GO solution maintained a sphere shape when it was dropped on nylon, polyester, and cotton fabrics. On the other hand, ethanol-based GO solution was rapidly spread out and absorbed into the fabrics, which makes it tough to control a specific coating area. This behavior results from different surface tension energy of water and ethanol, $72.8 * 10^{-3} J/m^2$ and $22 *$

$10^{-3} J/m^2$, respectively[109]. Since water has high strong intermolecular cohesive force than adhesion force in between fabric and water, it can retain the sphere shape with high surface tension. However, with its low surface tension and high evaporation at room temperature, ethanol rapidly spilled over into the fabric. After drying the solution, each GO film was examined by SEM as shown in figure 4.4 (b,c). Water dispersed GO was uniformly built on the rough surface of the fabric by fully covering each fiber. In the case of ethanol dispersed GO, GO flakes were sucked into the spatial crack in between fibers. For water solvent, GO nanoflakes were uniformly gravitated in the solution and slowly dried while the solution kept its state due to the relatively slow absorption and evaporation of water at room temperature. However, GO flakes in ethanol solvent were immediately drawn into the weave gap in a state of agglomeration because of the fast absorption and evaporation rate of ethanol. As a result, GO flake in ethanol did not fully cover the fabric sensor platform.
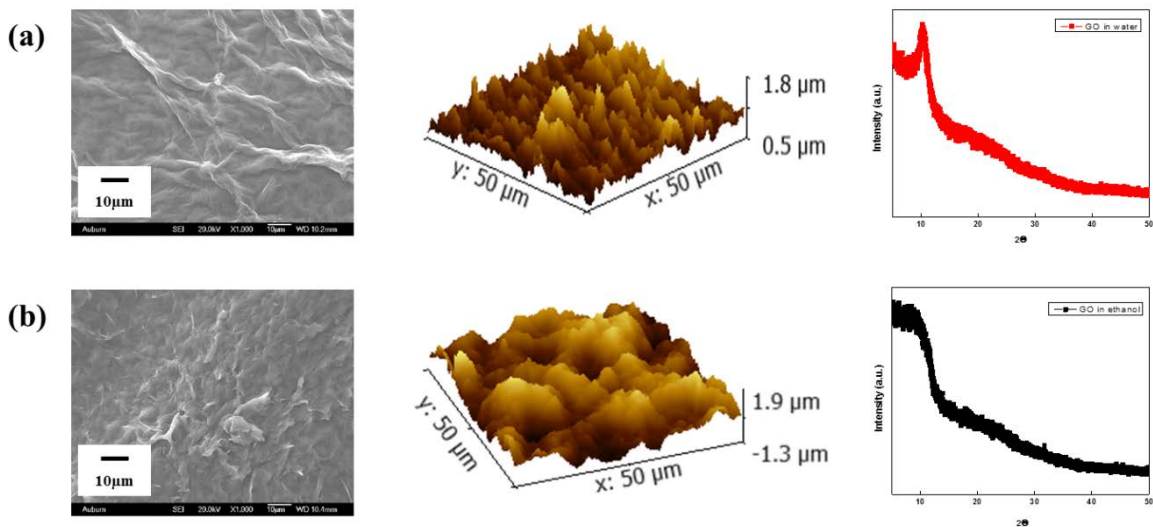
Figure 4.5. SEM, AFM and XRD results of dried GO dispersed in (b) water, (c) ethanol on the polyimide film.

To eliminate the effect of the fabric on the roughness, two types of GO solution dispersed in water and ethanol were dropped apiece on the flat polyimide film. GO has wrinkled morphology in both solvent because carboxyl and hydroxyl of GO cause van der Waals interaction[110]. Similar to the SEM images in figure 4.5, GO distributed in water was more uniformly constructed compared to GO in ethanol, in which GO flakes were non-uniformly crumpled. AFM also showed that the average roughness of water-based GO is smaller than that of ethanol-based GO where the number is 281.67 and 447.23 respectively. In this regard, the XRD result can be interpreted that the smoother GO peak in ethanol-based GO solutions is due to the randomly stacked and agglomerated GO nanoflakes by immediate evaporation of ethanol.

4.4. Gas sensing performance

	Nylon	Polyester	Cotton
(a)	(b)	(c)	
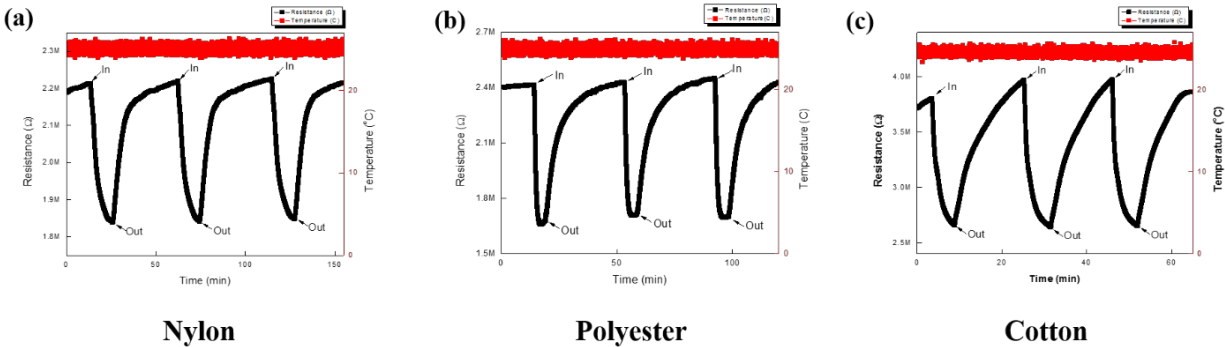
Figure 4.6. Resistance change profiles of the GO film constructed on PVC coated (a) nylon, (b) polyester and (c) cotton at room temperature under 100 ppm ammonia.

The ammonia gas sensing characteristics of GO films integrated on the fabric were conducted by measuring resistance change. Figure 4.6 shows the resistance profiles of GO fabric

60

sensor at room temperature with 100 ppm ammonia gas. The initial resistance of GO film was around 2 or 3 MΩ at room temperature, and its sensing behavior on ammonia showed n-type. The gas response was determined as the ratio of the resistance difference with or without detecting gas (ΔR) to that of in air (R_a). The average gas response of GO on 100 ppm ammonia was 0.16, 0.25, 0.35 to nylon, polyester, and cotton fabrics, which value is a comparable result of GO on flat substrates[111]. The sensing ability of fabric sensor was demonstrated; however, its sensing film was peeled off from the fabric substrate after bending. To increase adhesion between sensing film and fabric substrates, further investigation on coating properties of drop-casted GO solution onto the fabric was conducted by mixing two solvents with various concentrations. As shown in table 4.2, contact angle between GO solution and nylon fabric was gradually reduced with higher ratio of ethanol, showing good wettability. However, GO solution in over 50 vol% ethanol rapidly adsorbed into the fabric by passing through tiny pores of the woven fabrics, which ends up with disconnection of sensing material on interdigitated electrodes. With two concentration of ethanol, 0 vol% and 20 vol%, gas sensing properties were compared. Ammonia molecules with 100 ppm concentration were detected by both sensors at RT with 0.16 and 0.22 gas response from 0 vol% ethanol-based GO and 20 vol% ethanol-based GO respectively. However, huge difference appeared after mechanical bending. Adhesion between 0 vol% ethanol-based GO and hydrophobic nylon fabric was not strong enough to endure bending, resulting in detachment after 15° bending. On the other hand, 20 vol% of ethanol-based GO film showed high resistance to bending over 70°, and sensing response was almost maintained after 100 cycles of 70° bending. Balance between surface tension of the solution and capillary force of the fabric yield uniform stacking, resulting in high resistance for bending.

Table 4.2. Coating properties of drop-casted GO solution on nylon fabric.

Ethanol Vol %	0	20	50
Photograph			
Contact angle	110°	100°	80°
Time until 0° contact angle	5h	3h	30 min
Initial resistance	2~3 MΩ	2~3 MΩ	Over 100 MΩ
Gas response	0.16	0.22 > 0.2	-
Max bending angle	15~20°	70°	-
Resistance after 100 bending	Over 100 MΩ	9 MΩ	-

4.5. Conclusion

To manufacture sensing device on textile, various flexible and wearable substrates were examined from polyimide film to bare fabrics, and several low-temperature and non-corrosive fabricate processes were explored. In particular, interdigitate electrodes were fabricated on nylon, polyester, and cotton fabrics, and room temperature gas sensing of GO fabric sensor was demonstrated. Thin PVC film was coated on top of the fabrics to laminate rugged surface of the fabric for electrode connection. The interdigitated electrodes were successfully patterned by sputtering and silk-printing. To integrate GO on the fabric sensor platform, a facile solution method was used. Water and ethanol were compared as typical solvents to disperse GO. Water dispersed GO solution was uniformly constructed onto the fabrics, whereas ethanol dispersed GO solution was rapidly absorbed into the weave gap showing a state of agglomeration. To enhance adhesion between GO sensing film and hydrophobic fabrics, further investigation on coating properties were conducting by melding two solvents with various ratio. After drying the coated GO solutions, the morphologies of the dried GO films were investigated by comparing surface roughness. Gas sensing response of the GO on three types of fabrics, nylon, polyester, and cotton, was compared using 100 ppm of ammonia gas at room temperature. Improved adhesion between sensing film and hydrophilic fabric was obtained by tailoring wetting properties of solution where surface tension of solution and capillary force of fabric were balanced, resulting in uniformly stacked structure and high resistance of bending.

Chapter 5. Exploration of 2D Nanomaterials for Room Temperature Detection

5.1. Introduction

Two-dimensional (2D) nanomaterials have demonstrated great potential in the field of gas sensing due to their layered structures. Originating from their atomically thin layers, the 2D nanostructured materials manifest unique chemical and physical characteristics, which show great promise for sensing applications. The atomic-scale thickness of a 2D nanomaterial enlarges the surface-to-volume ratio, which provides more active surface area to react to analytes. In particular, the ability of 2D nanomaterials to identify gas analytes at room temperature offers the possibility of wearable gas sensors integrated onto a flexible substrate. Even though much attention has been focused on graphene and modified graphene oxide (GO) for sensing materials, pure GO, with abundant oxygen functional groups, has investigated as a practical material due to its capability of mass production. In addition, it has been well accepted that GO would be preferable to graphene to absorb gas molecules, since the surface functional groups, such as hydroxyl and epoxy, promote the interaction between gas and GO. Consequently, it seems intriguing to investigate pure GO's material properties and sensing performance at RT. Along with carbon-based materials, other 2D materials, including phosphorene and silicane, have been introduced as promising sensing materials for room temperature gas detection. Especially for 2D transition metal dichalcogenides (TMDs), inherent high surface areas and their unique semiconducting properties with tunable band gaps make them compelling for sensing applications. The fascinating electrical and optical properties of TMDs arise from the transition of an indirect band gap to a direct band gap as the

thickness changes from bulk to monolayer due to quantum confinement. Notably, contrary to GO, TMDs have few dangling bonds on the surface with a few of them on the edge. Consequently, sensing properties of these 2D nanomaterials were expected to different in terms of surface dangling bonds.

5.2. Materials characterization

- Graphene oxide (GO): First 2D material investigated for room temperature gas sensing was graphene oxide which is graphene sheet decorated with oxygen functional groups. Among 2D materials, GO is an attractive candidate as a sensing material due to its high electron mobility and excellent electron transport at room temperature as well as surface functional groups[44, 112].
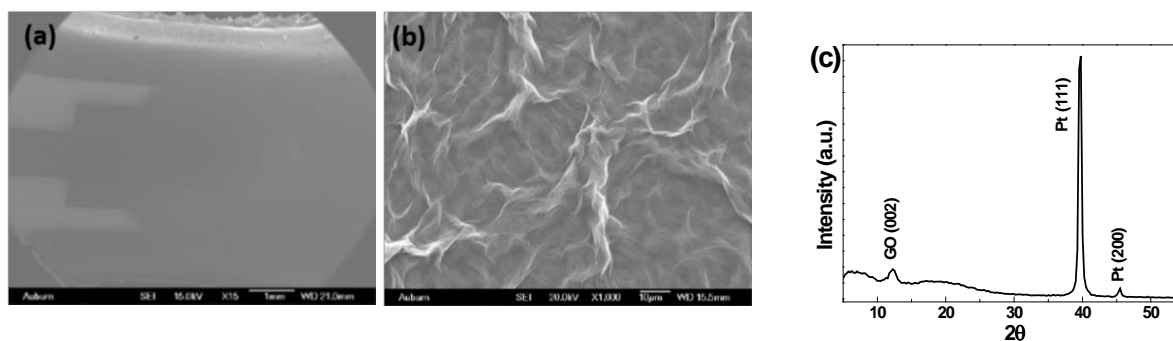
Figure 5.1. SEM images of 10 mg/ml graphene oxide (a) deposited on Pt electrode in polyimide film, (b) magnified view, and (c) XRD pattern of the graphene oxide film.

The GO sensor platform was fabricated on flexible polymer materials and characterized by SEM and XRD. Figure 5.1 (a) shows the morphology of the drop coated GO film on the interdigitated platinum electrodes of the polyimide film, and (b) shows the magnified view of the deposited GO in which GO fully covered interdigitated electrode. In magnified view of figure 5.1 (b), GO nanosheets have wrinkled or folded morphology. The functional groups, such as carboxyl and hydroxyl, of GO cause van der Waals interaction or hydrogen bonds. These bonds cause crumple the nanosheets to be folded and have corrugations [110]. To investigate its structural properties, XRD was conducted on the GO device. The XRD pattern shows that GO has a peak at around 10 ° of 2θ, which presents (002) faces, and the other two peaks corresponds to the platinum in the electrode. The peak position observed in GO can induce interlayer distance according to Bragg's law. The calculated interlayer distance of the GO is 8.10 Å (2θ = 10.9 °). The increased distance of GO compared to the typical value of 3.35 Å in graphite was caused by the repelling oxygen functional groups in graphite planes in the GO[113].
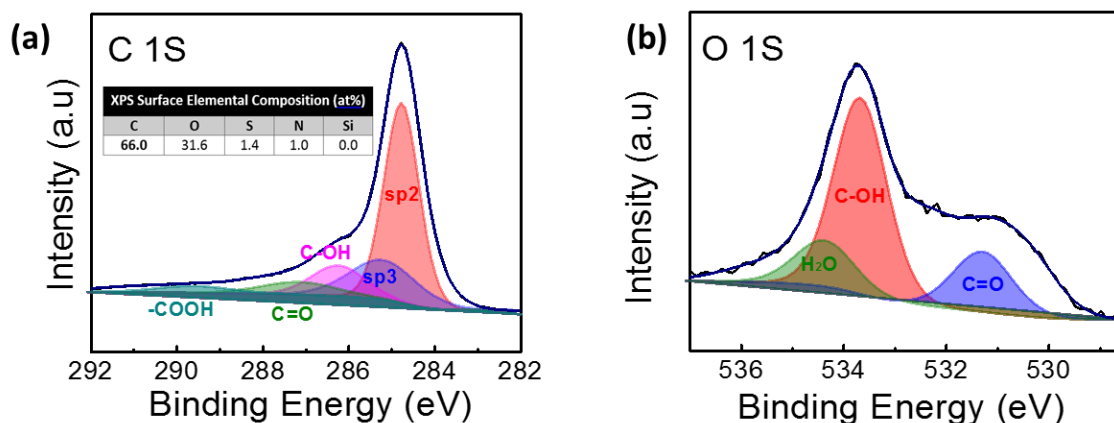
Figure 5.2. Survey XPS spectrum and surface stoichiometry from GO; high-resolution XPS spectrum over (a) the C1S region and (b) the O 1S region.

To analyze surface condition of the GO film, XPS was employed. The surface condition is an important aspect of the sensing mechanism. Figure 5.2 (a) shows the surface stoichiometry of GO where the elemental composition was listed. The C/O ratio of the GO was 2:1 which corresponds to the typical GO. For the comparison, it is reported that reduced GO has the C/O ratio to approximately 12:1[114]. Figure 5.2 (a) is the magnified XPS spectrum over the C1s region. It indicates that a considerable degree of oxidation of GO with oxygenated carbon atom, where the dominant functional group of the GO is C-O bond at 286.6eV. Importantly, figure 5.2 (b) shows the magnified O 1s region in which dominant oxygen functional groups on the surface of GO was hydroxyl.

- Molybdenum disulfide (MoS_2): Another 2D materials which have investigated as room temperature sensing material is MoS_2 in the family of TMDs. As introduced earlier, TMDs have unique physical and chemical properties such as tunable bandgap, from which intriguing performance can be expected. Prior to examine gas sensing performance, the material was characterized focusing on surface dangling bonds.
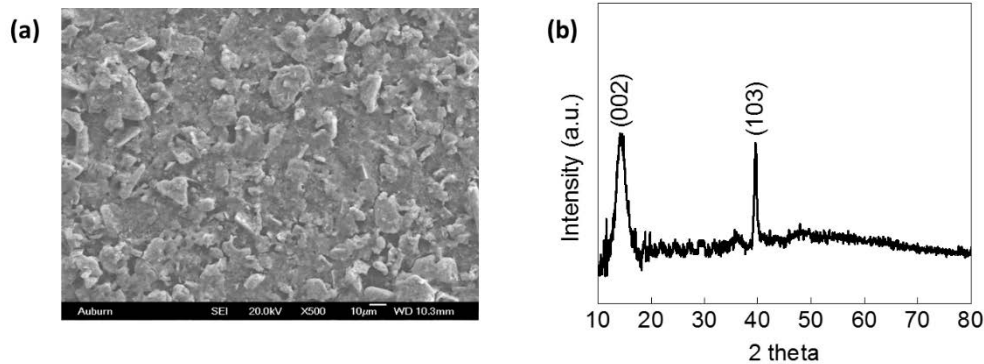
Figure 5.3. (a) SEM images and (b) XRD pattern of monolayer molybdenum disulfide film.

The monolayer MoS$_2$ Film was deposited by the solution process onto the polyimide film, and its morphology was observed by SEM. Figure 5.3 (a) clearly shows that many monolayer MoS$_2$ were well stacked in c-axis, which are different to the wrinkled morphology of GO. From the XRD peaks of MoS$_2$ in (002) face, the calculated interlayer distance of the MoS$_2$ is 6.13Å, which is consistent with theoretical value with few dangling bonds.

5.3. Gas sensing performance

- Graphene oxide (GO):
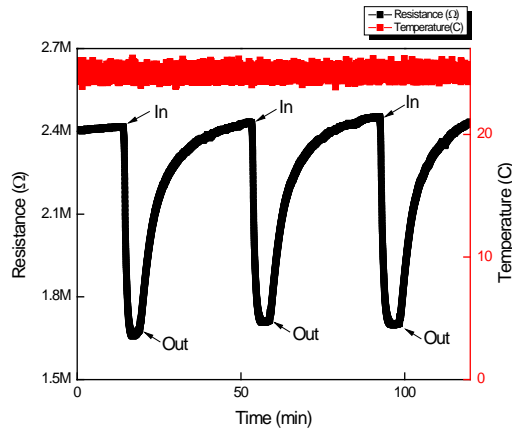
Figure 5.4. Gas sensing response of 10 mg/ml graphene oxide to 100 ppm of ammonia gas.

The gas sensing response of GO film to ammonia gas was investigated at room temperature as shown in figure 5.4. The initial resistance of the drop coated GO was 2~3MΩ at room temperature. Ammonia was found to be electron donor gas, and the sensing behavior of GO to

ammonia was n-type. When ammonia gas was introduced into the GO sensor system, the resistance was dropped and saturated. Then, GO's resistance was recovered to initial level when the ammonia gas was out as showing n-type behavior. Although r-GO has been known as a p-type material, GO has the ambipolar property depending on the number of functional groups. In our research, GO shows n-type sensing behavior to ammonia gas. The calculated gas response to ammonia gas is 0.3 which is similar value to literature as listed in table 2.4.
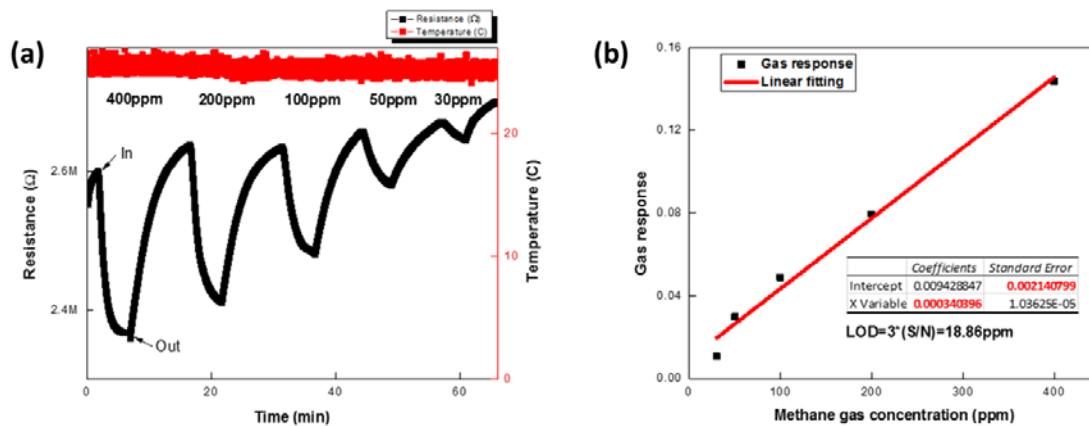
Figure 5.5. (a) Combined resistance profile of a GO sensor as a function of the methane concentration. (b) The relationship between gas response and methane concentration.

In this research, to demonstrate GO's ability to sense methane at room temperature, the gas sensing performance of 10mg/ml GO detecting methane gas was examined as a function of methane concentration. Unlike ammonia, methane is a difficult gas to be reacted due to its non-polarity and high enthalpy of four equivalent C-H bonding. Nitrogen balanced methane gas was injected as a targeted gas, and its concentration was adjusted from 400ppm to 30ppm. The initial resistance of the drop coated pure GO was 2~3 MΩ at room temperature depending on the

condition of each sample. Once methane gas was introduced into the GO sensor system, the resistance was dropped and saturated. Then, GO's resistance was recovered to the initial level, when the methane gas was not present, showing n-type behavior to methane gas. The same n-type sensing behavior of GO sensor was observed in all ranges of methane gas. The gas sensing mechanism of the GO sensor could be explained by gas reaction with the oxygen functional groups of the surface of the GO. Methane gas molecules react with the GO surface and replace the oxygen ions with electrons into the GO by means of the following Eq. (6):

$$CH_4 + \ 4O^-(ads) \rightarrow CO_2(gas) + 2H_2O + 4e \ \text{Eq. (6)}$$
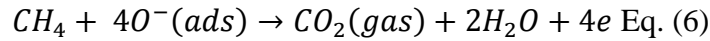
As an electron donor, methane gas transfers electron to GO, leading the resistance of GO decreases. Fundamentally, some studies reported that GO could be considered as ambipolar semiconductor due to the oxygen functional groups. GO has both a shallow donor level with low density of state and a deep acceptor level with high density of state[115]. In addition, methane gas has been noticed as electron donor gas which is confirmed by first-principles simulations based on density functional theory calculations[116]. As a result, the resistance of GO with poor n-type characteristic was dropped when electron donor gas introduced, then it was recovered without electron supply. Figure 5.5 (a) shows the collected data of GO sensing toward different methane concentrations of 400, 200, 100, 50, and 30 ppm at room temperature. For all concentration, the device showed n-type sensing behavior to methane. The GO device exhibited a high response to methane in a low concentration ranging from 30 ppm to 400 ppm. The performance of this device toward methane was greater compared to that of other various sensing materials operated at room temperature. [117] [118] [119]The reduced gas response was obtained by decreasing the methane gas concentration up to 30 ppm. In figure 5.5 (right), the graph shows the gas response of a GO sensor in terms of the

70

concentration of methane gas. The gas response was calculated in the same manner as the ratio of $(R_g - R_a)/R_a$, where R_g is the resistance of GO film under the target gas, and R_a is the resistance of GO film under the ambient air. The responses were varied from 0.0108 to 0.143 at 30 ppm and 400 ppm of methane, respectively. The limit of detection (LOD), the lowest concentration of target gas that can be distinguished from the common atmosphere[120], was also calculated based on the signal to noise ratio (S/N>3)[116] as shown in figure 5.5 (b). In this case, the theoretical LOD to methane gas was found to be 18.86 ppm at room temperature.

- Molybdenum disulfide (MoS$_2$):
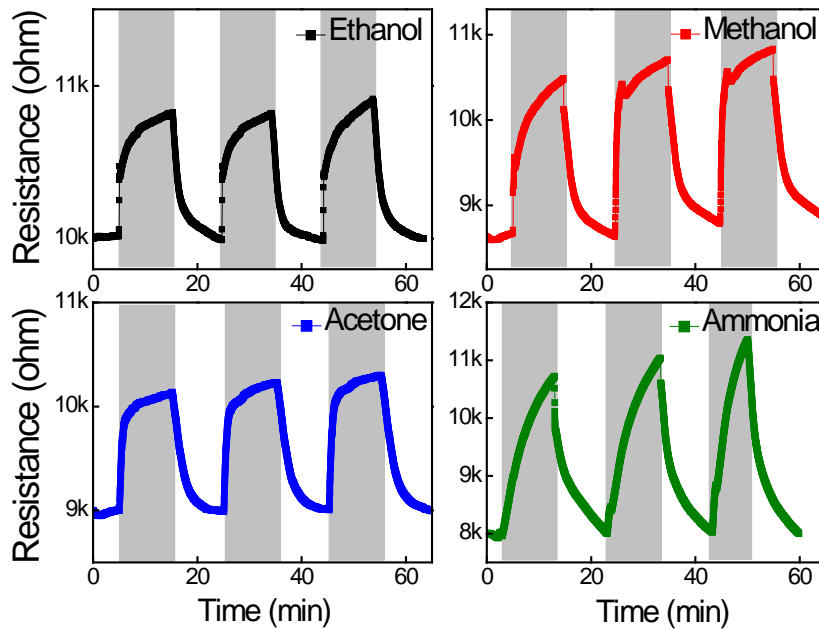
Figure 5.6. Gas sensing results of drop-casted monolayer MoS$_2$ film toward 100 ppm ethanol, methanol, acetone, and ammonia gas bubbling at room temperature.

The gas sensing response of drop-casted monolayer MoS_2 film to various reducing gases was investigated at room temperature as shown in figure 5.6. The initial resistance of the drop coated MoS_2 film was 8~10kΩ at room temperature. It is reported that reducing gases including ethanol, methanol, acetone and ammonia was found to be electron donor gas. When reducing gases were introduced into the MoS_2 sensor, the resistance was increased and saturated. Then, resistance of MoS_2 film was recovered when the analyte gases were out as showing p-type behavior. Although bulk MoS_2 has been known as a n-type semiconductor, monolayer MoS_2 film shows p-type sensing behavior[121]. Unlike GO in which oxygen functional groups are dominant role in sensing, the basic principle of gas sensing in 2D TMDs is mainly based on the charge transfer processes between gas molecules and the surface of sensing materials. Different from the conventional metal oxides, the 2D materials act as a charge acceptor or donor, resulting in the resistance (or conductance) change of the overall system. Once exposed to reactive gases, gas molecules are absorbed on the surface of 2D materials by the electrostatic force. The direction of electron charge transfer is determined by the type of reactive gas either reducing or oxidizing. The resistance of the sensing material is recovered up to its initial value due to desorption of gas molecules upon exposure to air. The amount of resistance modulation is determined by the charge affinity of reactive gas to release or withdraw electrons.
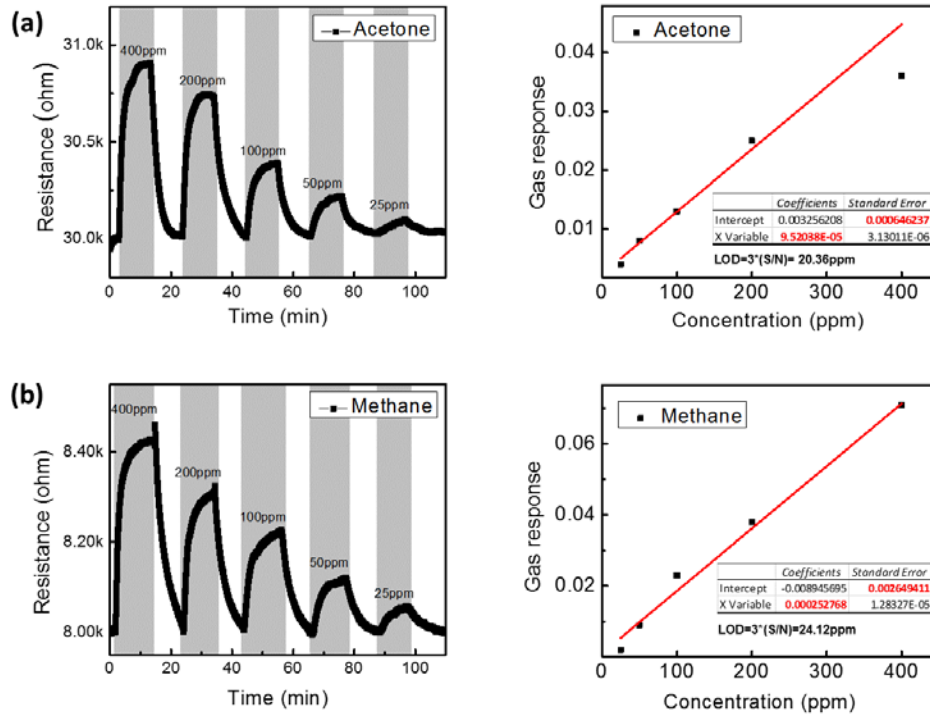
Figure 5.7. Combined resistance profile of a MoS_2 sensor as a function of the analyte concentration, and the relationship between gas response and analyte concentration in (a) acetone and (b)methane.

Figure 5.7 (a) shows the collected data of MoS_2 sensing toward different acetone and methane concentrations from 400 to 25 ppm at room temperature. For all concentration, the device showed p-type sensing behavior to acetone and methane (reducing gases). In figure 5.7 (a), the right graph shows the gas response of a MoS_2 sensor in terms of the concentration of acetone gas. The responses were varied from 0.004 to 0.036 at 25 ppm and 400 ppm of acetone respectively. The theoretical limits of detection (LOD) was also calculated based on the signal to noise ratio (S/N>3) as shown in figure 5.7 (b). In this case, the theoretical LOD to methane gas was found to be 20.36 ppm at room temperature. In a similar way, figure 5.7 (b) corresponds the gas response of a MoS_2 sensor in terms of the concentration of methane gas. The responses were varied from

73

0.002 to 0.071 at 25 ppm and 400 ppm of methane respectively. The theoretical limits of detection (LoD) to methane gas was found to be 24.12 ppm at room temperature.

Gas sensing properties of MoS_2 and GO were compared in terms of gas response, recovery time, long-term stability, and LoD in table 5.1. As to the sensing of ammonia with strong polarity, both materials detected with similar response. However, shorter recovery time and longer stability were obtained from MoS_2. Similarly, as to the sensing of methane with non-polarity, higher gas response and lower LoD were attained from GO, whereas shorter recovery time came from MoS_2. These different sensing properties of MoS_2 and GO can be understood by different sensing mechanism which associated with the existence of surface dangling bonds. As explained, sensing mechanism of MoS_2 is charge transfer with weak physisorption between MoS_2 and gas molecules. Kinetically, desorption process of MoS_2 was faster, which drives fast recovery and long-term stability. On the other hand, as for GO sensing mechanism, gas molecules mainly react with oxygen functional groups of GO such as hydroxyl with large adsorption energy. Accordingly, the higher gas response and lower LoD were driven and longer recovery time as a trade-off.

Table 5.1. Gas sensing properties comparison of MoS_2 and GO.

	Ammonia sensing		Methane sensing	
	GO	MoS_2	GO	MoS_2
Gas response	0.3	0.28	0.05	0.02
Recovery time	15 min	7 min	12 min	7 min
Stability/ LoD	2 weeks	3 months	18 ppm	24 ppm

5.4. Conclusions

Room temperature gas detection utilizing two-dimensional nanomaterial sensing materials was demonstrated using two representative 2D nanomaterials, graphene oxide (GO) and molybdenum disulfide (MoS_2). Commercially available GO and monolayer MoS_2 were drop-casted on flexible polyimide films, and their morphology and surface condition was studied. Using prepared film sensors, gas detection was successfully conducted at room temperature with various reducing gases under the ambient background atmosphere. The GO sensor detected ammonia and methane, while MoS_2 sensor sensed ethanol, methanol, acetone, ammonia, and methane at RT. GO showed n-type sensing behavior to reducing gases, whereas, monolayer MoS_2 showed p-type behavior. The dominant gas sensing mechanisms of GO and MoS_2 are quite different. In GO sensing, oxygen functional groups, such as hydroxyl, on the surface of GO are considered to play a critical role absorbing and interacting with analyte. On the other hand, a charge transfer mechanism is main mechanism in case of MoS_2, with a few surface bonding bonds. Due to surface functional groups, higher gas response and lower LoD was obtained from GO was higher than that of MoS_2 at the expense of incomplete recovery and short long-term stability. Sensing properties analysis of typical 2D nanomaterials based on their surface dangling bonds provide guidance for material selection depending on desired sensing properties.

Chapter 6. Introduction of 2D Titanium Carbide (MXenes) for Gas Sensing Application

6.1. Introduction

Prevention of illness at its early stage is the best treatment, and most people are interested in this approach since it essentially conduces to a healthy life. Early illness detection before the disease has worsened is likely to give more chances for treatment, which could contribute to an increased possibility of survival among patients[122]. One promising attempt for early stage prevention is continuous physiological monitoring of the human body from breath, heart rate, and skin.[8, 123] It is noticeable that around 200 compounds have been detected in human breath, and some of them signal the physical condition of the body[124]. For example, acetone is produced from diabetic patients, and ammonia was measured in patients with lung diseases[125-126]. Accordingly, utilizing the detection of gases with consistent breath analysis will be a practical health care approach in many aspects including cost and usability. To be more pragmatic, sensors should be equipped with some other functionalities such as portability and wearability. Many researchers have endeavored to develop electronics with such functions. The portable and wearable electronic hardware should have the flexibility for a natural fit. Furthermore, the system should be able to operate at low temperature without additional power supply for practical deployment[8, 108]. However, common gas detection devices are fabricated on solid substrates such as silicon wafers and indium tin oxide (ITO) coated glass and thus cannot be integrated into wearable electronics. In addition, most commercialized metal oxide sensors comprising of SnO_2, ZnO or NiO operate at elevated temperature over 100°C, which critically limits their adaptation to wearable monitoring

system[26, 127]. Therefore, it is essential to explore new material for excellent room temperature sensing ability with manufacturability on flexible substrates.

Two-dimensional (2D) materials such as graphene, transition metal dichalcogenides, and recently transition metal carbides and their hybrids have shown promising properties for various applications such as sensors and energy storage/conversion[8-11]. Among the many 2D materials that are reported in recent years, a new family of 2D materials, which are collectively referred to as MXenes, 2D transition metal carbides, nitrides, and carbonitrides. MXenes show unique physical and chemical properties and high potential for applications ranging from energy storage to water purification to gas sensors[66, 128]. Since their discovery in 2011, around 19 different MXenes have been successfully synthesized. The recent discovery of ordered, double transition metals MXenes will probably lead to the synthesis of a larger number of this interesting family of materials[66-67]. $Ti_3C_2T_x$ is the first discovered and well investigated material of the MXenes. $Ti_3C_2T_x$ is exfoliated from Ti_3AlC_2 MAX phase, a ternary carbide with a hexagonal closed-packed structure, by selectively etching Al atoms[68-69]. The M-A bonds in the MAX phases are chemically more reactive than M-X bonds, which makes the selective etching of A-layer atoms possible. In the case of Ti_3AlC_2, removal of Al atoms in aqueous hydrofluoric (HF) acid solutions results in weakly bonded $Ti_3C_2T_x$ layers that can be further separated through intercalation of large organic molecules like dimethyl sulfoxide (DMSO)[70]. It is also shown that $Ti_3C_2T_x$ can be synthesized and directly delaminated through etching with a mixture of LiF salt and HCl acid[71]. This method eliminates the use of hazardous HF and intercalation of large organic molecules, resulting in facile synthesis process for delaminated MXene solutions[71]. In both cases, the surface of $Ti_3C_2T_x$ is mostly terminated by oxygen, hydroxyl, and fluorine groups, and the synthesis method has a great influence on the ratio of these groups on the surface of synthesized MXene[69]. For simplicity, the

existence of these different functional groups is shown with T_x in MXenes formula, i.e. $Ti_3C_2T_x$. According to the Density functional theory (DFT) calculations, the type and concentration of these surface terminations largely effects on the properties of MXenes, through which MXenes can be easily tailored in compliance with various applications[29, 72-74].

6.2. Material characterization
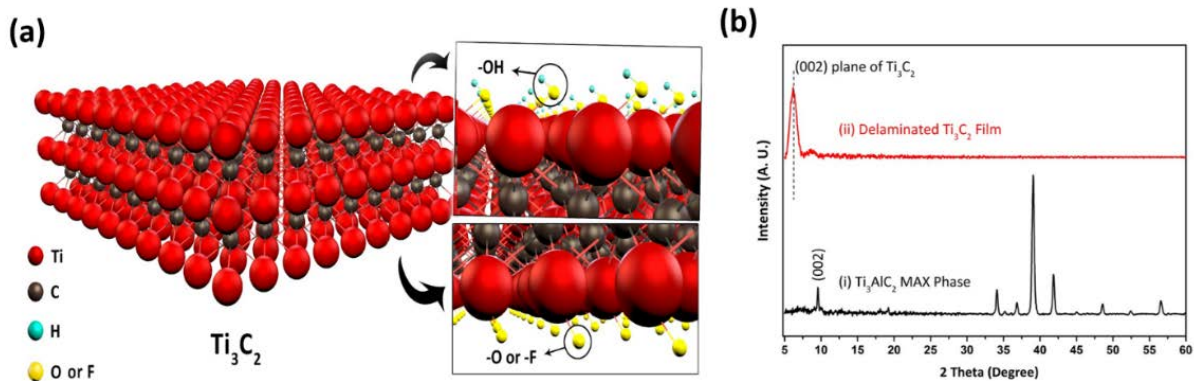
Figure 6.1. (a) A schematic representation of $Ti_3C_2T_x$ structure and different functional groups on the surface of $Ti_3C_2T_x$ nanosheets and (b) XRD pattern of (i) Ti_3AlC_2 before etching and (ii) delaminated $Ti_3C_2T_x$ film after selective removal of Al from MAX phase structure showing disappearance of MAX phase peaks and the shifting of (002) plane to lower angles.

Figure 6.1 (a) shows a schematic representation of a 2D $Ti_3C_2T_x$ structure and its surface functional groups, where two layers of carbon are sandwiched between three layers of titanium. With synthesis method used in this work we expect the surface of nanosheets to be randomly terminated with -OH, -O, and -F functional groups[74]. XRD patterns of Ti_3AlC_2 MAX phase and

the $Ti_3C_2T_x$ film are shown in figure 6.1 (b). Due to the complete removal of Al and successful delamination of $Ti_3C_2T_x$, all the peaks related to Ti_3AlC_2 MAX phase disappeared after etching, expect the peak corresponding to the (002) plane. The (002) peak is shifted toward the lower angles indicating an increase in the d-spacing and c-lattice parameter (C-LP) of the produced $Ti_3C_2T_x$ compared to the original Ti_3AlC_2 MAX phase, which is in good agreement with previously reported results in the literature[14].
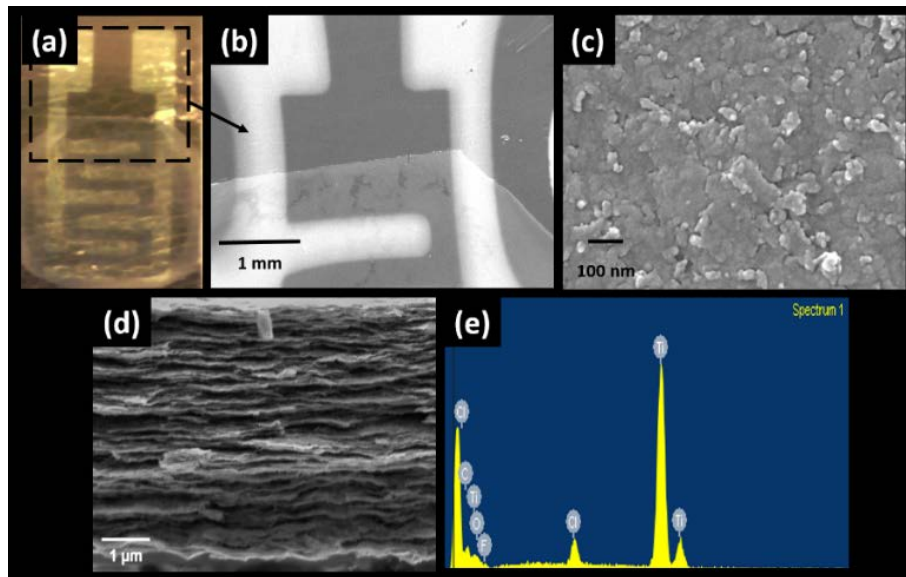
Figure 6.2. Morphological characterization of $Ti_3C_2T_x$ film (a) Optical image of the overall $Ti_3C_2T_x$ sensor platform, (b)SEM micrograph of the dried $Ti_3C_2T_x$ film on interdigital platinum electrodes deposited on a flexible polyimide film, (c) magnified view of coated $Ti_3C_2T_x$ film, (d) cross-section view of the film and (e) EDS analysis of the film.

Figure 6.2 (a) shows the optical image of the overall $Ti_3C_2T_x$ sensor platform with a circular shape of Ti_3C_2 droplet. Figures 6.2 (b, c) show the morphology of the drop casted $Ti_3C_2T_x$ film on the interdigitated platinum electrodes. The SEM images show a uniform deposition of the delaminated $Ti_3C_2T_x$ after solution casting. The thickness of the coated films was measured to be around 30 nm. It was also observed that the deposited $Ti_3C_2T_x$ films had fully covered the 400 µm gap of the interdigitated electrodes, electrically connecting the electrodes. Figure 6.2 (d) shows a cross-sectional SEM image of a $Ti_3C_2T_x$ film produced through vacuum filtration of the same $Ti_3C_2T_x$ solution used for the gas sensing device fabrication. The observed layered structure is due to the stacking of many individual layers of $Ti_3C_2T_x$. Delamination of $Ti_3C_2T_x$ to 2D sheets results in their increased surface to volume ratio, which in principle should contribute to a large gas sensing response for 2D $Ti_3C_2T_x$. In figure 6.2 (e), the EDS analysis of $Ti_3C_2T_x$ confirmed selective removal of Al from the structure. A small amount of chlorine was detected with EDS due to the remaining residues etching solutions.
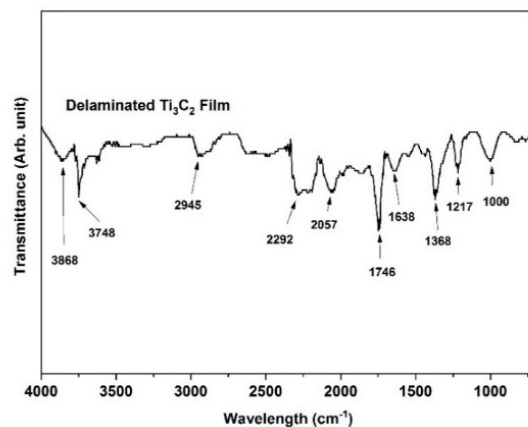
Figure 6.3. FTIR spectrum of the delaminated $Ti_3C_2T_x$.

Because chemi-resistive gas sensing is based on surface reactions, FTIR was conducted to observe the surface condition of delaminated $Ti_3C_2T_x$ film. As shown in figure 6.3, the dips at 3868, 3748, and 2945 cm^{-1} mostly correspond to hydroxyl groups, the dips at 2292 and 2057 cm^{-1} correspond to hydrogen bonding due to the presence of oxygen groups, the dip at 1746 and 1635 cm^{-1} corresponds to C=O bonding, the dip at 1368 cm^{-1} is due to the presence of molecular water (O-H), and the dips at 1217 and 1000 cm^{-1} correspond to oxygen group vibrations and possible C-F vibrations as also presence of fluorine (F) was suggested by our EDS results[129-131]. According to our FTIR data and the previous reports in the literature[132], oxygen and hydroxyl groups are the dominating functional groups on the surface of $Ti_3C_2T_x$. The MXenes that are produced by etching in LiF-HCl solutions have much less F terminated surfaces compared to the ones produced by etching in concentrated HF[66, 74]. Therefore, due to low concertation of fluorine, no sharp and strong peaks corresponding to presence of F was detected in our FTIR studies. The presence of abundant oxygen and hydroxyl groups on the surface of $Ti_3C_2T_x$ produced by this method might be favorable for gas sensing performance[133].

81

6.3. Gas sensing performance
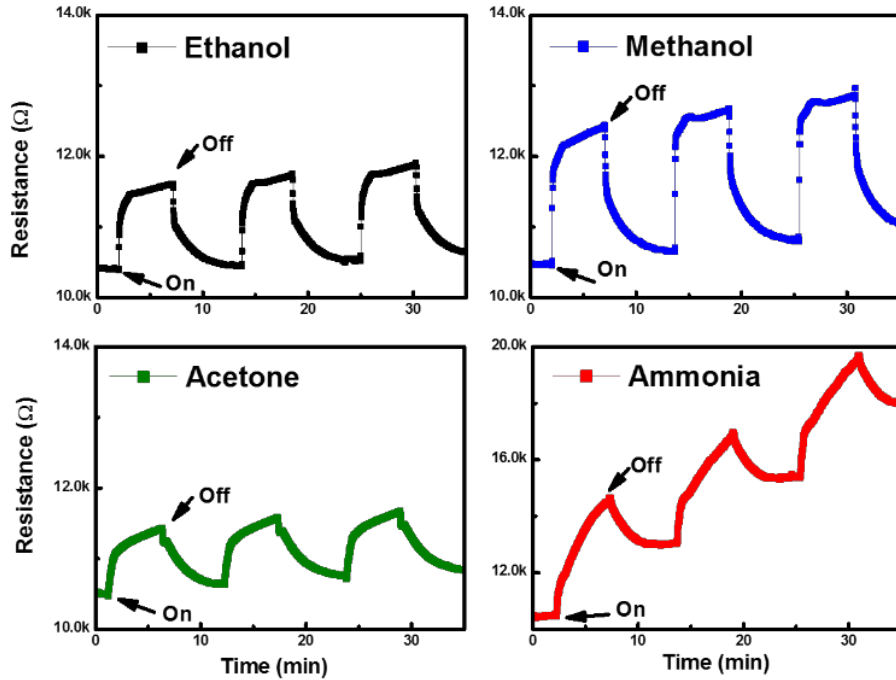
Figure 6.4. Gas sensing results of a device based on $Ti_3C_2T_x$ toward 100 ppm ethanol, methanol, acetone, and ammonia gas bubbling at room temperature (25°C).

We demonstrated that a sensor based on $Ti_3C_2T_x$ MXene films fabricated on flexible polyimide substrates can successfully detect various 100 ppm polar gases at room temperature. Figure 6.4 shows the dynamic gas sensing behavior of the $Ti_3C_2T_x$ device for 100 ppm ethanol, methanol, acetone and ammonia gas under ambient atmosphere. The initial resistance of $Ti_3C_2T_x$ film was around 10 kΩ at room temperature, and its thickness was 30 nm. Theoretically $Ti_3C_2T_x$ is considered to be metallic, however, it is reported that its electrical property can be tuned to semiconductive properties with surface terminations[133-134]. The surface functional groups could

change the metallic MXene to a narrow bandgap semiconductor[66]. Specifically, the presence of functional groups causes dipole polarization of the surface and decreases electrical conductivity to the semiconductor level[135], which is able to achieve gas detection in a chemi-resistive sensor. During the experiment, the $Ti_3C_2T_x$ sensor was periodically exposed to four types of 100 ppm gases for 5 minutes followed by a flow of clean air where nitrogen and oxygen gas were at 80 sccm and 20 sccm to recover the base resistance of the sensor. Upon the introduction of all ethanol, methanol, acetone and ammonia gases, the resistance of the $Ti_3C_2T_x$ film was increased, and it was decreased without the gases, showing a p-type sensing behavior. This procedure was repeated three times for each gas, and the resistance change was quite reproducible.
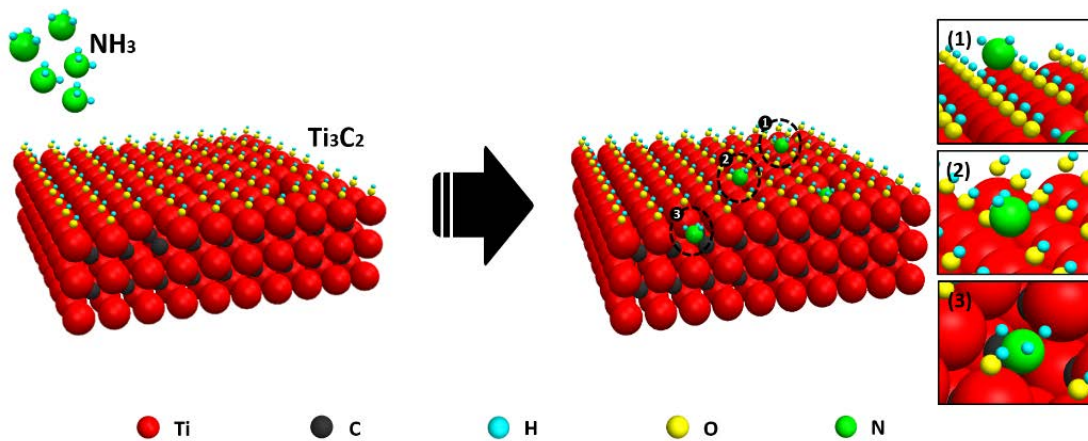
Figure 6.5. A schematic illustration of a possible gas sensing mechanism of the $Ti_3C_2T_x$ MXene for NH_3 gas.

The sensing performance of the fabricated device is attributed to the effective adsorption/desorption of the sensing species on the surface of $Ti_3C_2T_x$ 2D sheets[75-76]. The process of adsorption/desorption leads to the change in the electrical condition of the $Ti_3C_2T_x$ surface as illustrated in figure 6.5. In general, target molecules are adsorbed on the surface of a sensing material with two types of adsorptive interactions, depending on the reaction types. For MXenes, gas absorption can take place at active defect sites of the $Ti_3C_2T_x$ surface, and it can also result from the interactions with surface functional groups[12]. With functional groups, gas absorption is induced by dispersion forces such as hydrogen bonds, and it leads to relatively small resistance changes due to its weaker intermolecular force. On the other hand, gas absorption might arise from replacement surface functional groups with gas molecules, which causes a charge carrier transfer between the adsorbent and the adsorbate gas[136], resulting in a significant resistance change of the $Ti_3C_2T_x$ film.

We believe that the sensing mechanism of a $Ti_3C_2T_x$ sensor involves absorption of the sensed gases by both defects and functional groups. Some sensing species are bonded on the structural defects of the $Ti_3C_2T_x$ nanosheets, and some are bonded and interacted with surface terminations such as -O and –OH. In our experiments, all adsorbate gases such as ethanol, methanol, acetone, and ammonia gas have been reported as electron donors gases[29], and the $Ti_3C_2T_x$ film showed a p-type sensing behavior against all four gases. The p-type semiconducting property of the $Ti_3C_2T_x$ is possibly attributed to the adsorbed molecules such as water and oxygen which were mostly introduced during the Al etching process, and they would play the role of a p-type dopant for $Ti_3C_2T_x$[137-138]. In details, electron donor molecules are absorbed on the active sites of $Ti_3C_2T_x$ nanosheets mainly by dispersion forces between the polarized gas molecules and partially charged functional groups or defects. If the adsorbate gas molecules are absorbed by

functional groups such as hydroxyl, their bonding would be stronger through hydrogen bonds and the larger binding energy[43]. Thus, the electrons can be transferred from adsorbate gas to the $Ti_3C_2T_x$, and the concentration of majority charge carrier of the $Ti_3C_2T_x$ film decreases, resulting in resistance increments in the $Ti_3C_2T_x$ device. In figure 6.5, the electron transfer process of $Ti_3C_2T_x$ film towards NH_3 gas can be possibly addressed according to two possible reactions depending on the types of surface termination. The chemical species of the $Ti_3C_2T_x$ surface would react with NH_3 by the following routes, specifically, -O in Eq. (7) [139], and -OH in Eq. (8) [140].

$$2NH_3 + 3O^- \rightarrow N_2 + 3H_2O + 3e^- \quad \text{Eq. (7)}$$

$$NH_3 + OH^- \rightarrow NH_2 + H_2O + e^- \quad \text{Eq. (8)}$$
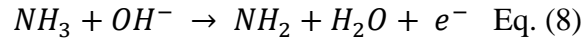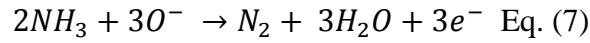
NH_3 gas molecules can be absorbed on the surface functional groups of $Ti_3C_2T_x$ such as O^- and OH^-. Thus, electron would be generated through Eq. (7) and (8), leading to a hole-electron recombination followed by an increase of electrical resistance.
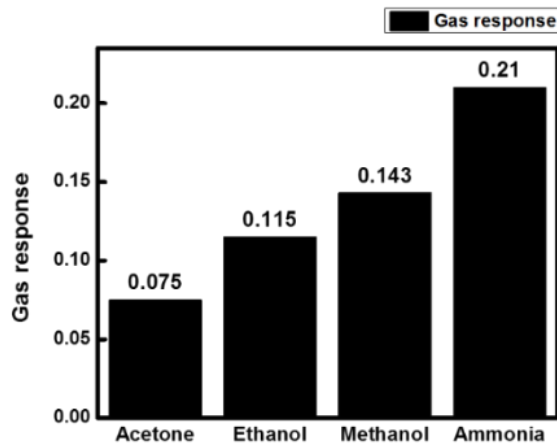
Figure 6.6. The calculated average gas response for each gas investigated in this study.

Figure 6.6 compares the gas response of the Ti$_3$C$_2$T$_x$ sensor to four different types of gases by averaging three repeated gas responses. The gas response was calculated as the ratio of ($R_g -$ $R_a)/R_a$, where R_g is the resistance of Ti$_3$C$_2$T$_x$ film under 100 ppm target gas, and R_a is the resistance of Ti$_3$C$_2$T$_x$ film under the ambient air. As shown in figure 6.6, the average gas response of Ti$_3$C$_2$T$_x$ was 0.210, 0.143, 0.115, and 0.075 for ammonia, methanol, ethanol and acetone, respectively. In our experiments, the Ti$_3$C$_2$T$_x$ sensor detected all of the tested VOC gases with the highest response with ammonia gas and the lowest with acetone gas. Yu et al.[75] have previously simulated a similar behavior for Ti$_2$CT$_x$ MXene based on theoretical calculations. In their work, DFT showed that the absorption energy of NH$_3$ is stronger than other polar molecules such as CH$_4$, CO, CO$_2$, and NO$_2$, therefore Ti$_2$CO$_2$ monolayer could sense only NH$_3$ among all considered gases. With a large absorption energy, NH$_3$ is easily absorbed to the functional group of the Ti$_3$C$_2$T$_x$ surface, which significantly increases resistance. However, it also caused the base resistance drift and retarded recovery time as maintained a strong bonding between adsorbent and adsorbate as shown in figure 6.6[76].
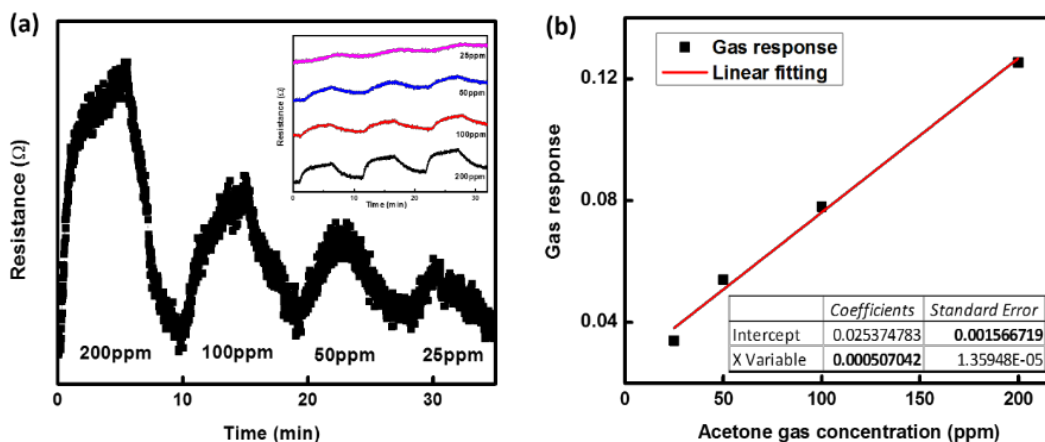
Figure 6.7. (a) Combined resistance profile of a $Ti_3C_2T_x$ sensor as a function of the acetone concentration. (b) The relationship between gas response and acetone concentration.

Since the $Ti_3C_2T_x$ based device has the lowest gas response to acetone gas among the four studied gases, gas sensing of the device was tested as a function of acetone concentration. Figure 6.7 (a) shows gas sensing results of a $Ti_3C_2T_x$ device toward four different acetone concentrations of 200, 100, 50, and 25 ppm at room temperature. For all cases, the device showed a p-type sensing behavior. The $Ti_3C_2T_x$ device exhibited a high response to acetone in a low concentration ranging from 25 ppm to 200 ppm, and the reactions were reproducible after testing for 3 times as shown in figure 6.7 (a). The performance of this device toward acetone was greater compared to that of other various sensing materials operated at high temperature[29, 141]. The gas response was reduced as the acetone gas concentration decreased to 25 ppm as shown in figure 6.7 (a). The average gas response of a $Ti_3C_2T_x$ sensor was calculated in terms of the concentration of acetone gas in figure 6.7 (b). The responses were varied from 0.034 to 0.125 at 25 ppm and 200 ppm of acetone, respectively. The limits of detection (LOD), the lowest concentration of target gas that can be distinguished from the common atmosphere[120], was also calculated based on the signal to noise

ratio (S/N>3)[116] as shown in figure 6.7 (b). In this case, the theoretical LOD to acetone gas was found to be 9.27 ppm at room temperature, and this value is lower than or comparable to other reported sensors based on 2D material such as graphene and MoS_2[142-143]. Accordingly, the LOD of the $Ti_3C_2T_x$ sensor to other gases such as ethanol, methanol, and ammonia should be lower with higher gas response, which suggests $Ti_3C_2T_x$ is a promising gas sensing material.

6.3. Conclusions

The capability of $Ti_3C_2T_x$ to sense an array of VOC gases at room temperature has demonstrated. The synthesized $Ti_3C_2T_x$ nanosheets were integrated on flexible polyimide films with a facile solution casting method, and their surface chemistry was investigated to study the surface reaction. The $Ti_3C_2T_x$ sensor successfully detected all the tested VOC gases such as ethanol, methanol, acetone, and ammonia at room temperature and showed a p-type sensing behavior. The $Ti_3C_2T_x$ sensor was found to have a high sensing response to ammonia due to its large absorption energy. The possible sensing mechanism of the sensor was also proposed in terms of the majority charge carrier transfer through the interaction between sensing species and the sensing material. This novel $Ti_3C_2T_x$ gas sensor will be a new generation of versatile sensors for futuristic wearable electronics with comparable performance to other 2D material sensors.

Chapter 7. Introduction of 2D Vanadium Carbide (MXenes) for Gas Sensing Application

7.1. Introduction

High-performance gas sensing technologies are critical for many applications such as environmental monitoring, industrial safety, food safety, and smart home systems, due to the potential environmental, health, and explosive hazards of various gases[144]. For example, in the field of green renewable energies, hydrogen and methane are widely utilized as fuels to produce electricity through fuel cell systems, which are becoming increasingly commercialized.[145-146] However, explosion hazard of highly pressurized hydrogen or methane and their flammable nature are serious concerns for the storage and delivery of these gases[147-149]. Therefore, the development of reliable gas-monitoring sensors that can detect very low limits (trace amount) of hydrogen and methane leakage is crucial to overcome the safety challenges and prevent catastrophic incidents. To achieve such levels of sensitivity, gas sensors should establish a rapid and accurate detection and maintain low operating temperature to avoid high power consumption and prevent inadvertent triggering of explosions[150-151]. However, the inert properties of these non-polar gases limits their interaction with conventional sensing materials resulting in their more difficult detection, particularly when they are present in trace amounts[152].

Two-dimensional (2D) materials are among the most promising materials for future sensing applications because of their characteristic chemical and physical properties that usually arise from their tunable and highly accessible surfaces[33, 153]. Unlike conventional metal oxides that are widely used in sensing industries, utilization of 2D materials such as graphene and transition

metal dichalcogenide (TMDs), has enabled the realization of low-temperature gas sensors.[90, 154] In particular, the high surface area to volume ratio of 2D materials and the ability to tailor them into desired structures with specific properties have resulted in devices with significantly improved sensing performances that can deliver a much faster and higher magnitude gas response even for trace amounts of gases[52, 155].

In the past few years, various 2D materials have been investigated as room temperature gas sensors[137, 156]. Recent studies in this direction include the demonstration of excellent properties of a family of 2D transition metal carbides and nitrides, called MXenes, as room temperature gas sensors[7, 157]. MXenes are synthesized by selective etching of metal atoms from the structure of MAX phases, a family of layered ternary carbides and nitrides[68-69]. The etching process is usually done in fluoride containing aqueous acidic solutions and results in termination of the surface of the produced MXenes with O, OH, and/or F functional groups[69, 158]. These surface functional groups are shown as T_x in the MXene formula ($M_{n+1}X_nT_x$, where M is a transition metal, X is carbon or nitrogen, and n can be 1, 2 or 3) [69, 158]. To date, 20 different MXene compositions have been experimentally synthesized and many more are theoretically predicted[158]. The diverse physiochemical properties of MXenes stemming from their versatile compositions as well as their functionalized and tunable surface chemistry has rendered these materials as promising candidates for a range of applications such as energy storage devices[78, 159-160], polymer hybrid and composite materials[161-163], electromagnetic interference shielding[128], and catalysis[164-165], to name a few. Recently, we demonstrated room temperature gas sensing capability of $Ti_3C_2T_x$ MXene[7]. The high signal-to-noise ratio of $Ti_3C_2T_x$ and its low limits of detection toward different gases[7, 157] provide a great promise for the development of high-performance and sensitive room temperature gas sensors. Alongside $Ti_3C_2T_x$, theoretical studies have suggested high sensitivity and selectivity of

several other MXene compositions, particularly, 2D flakes of Ti_2CT_x and V_2CT_x, for gas sensing applications[75]. In this direction, grafting responsive polymers on multilayered V_2CT_x was reported as a method to make MXenes-based hybrid materials with CO_2 and temperature dual-sensitivity[82]. However, to date, there has been no experimental report on gas sensing properties of V_2CT_x MXene.

7.2. Material characterization
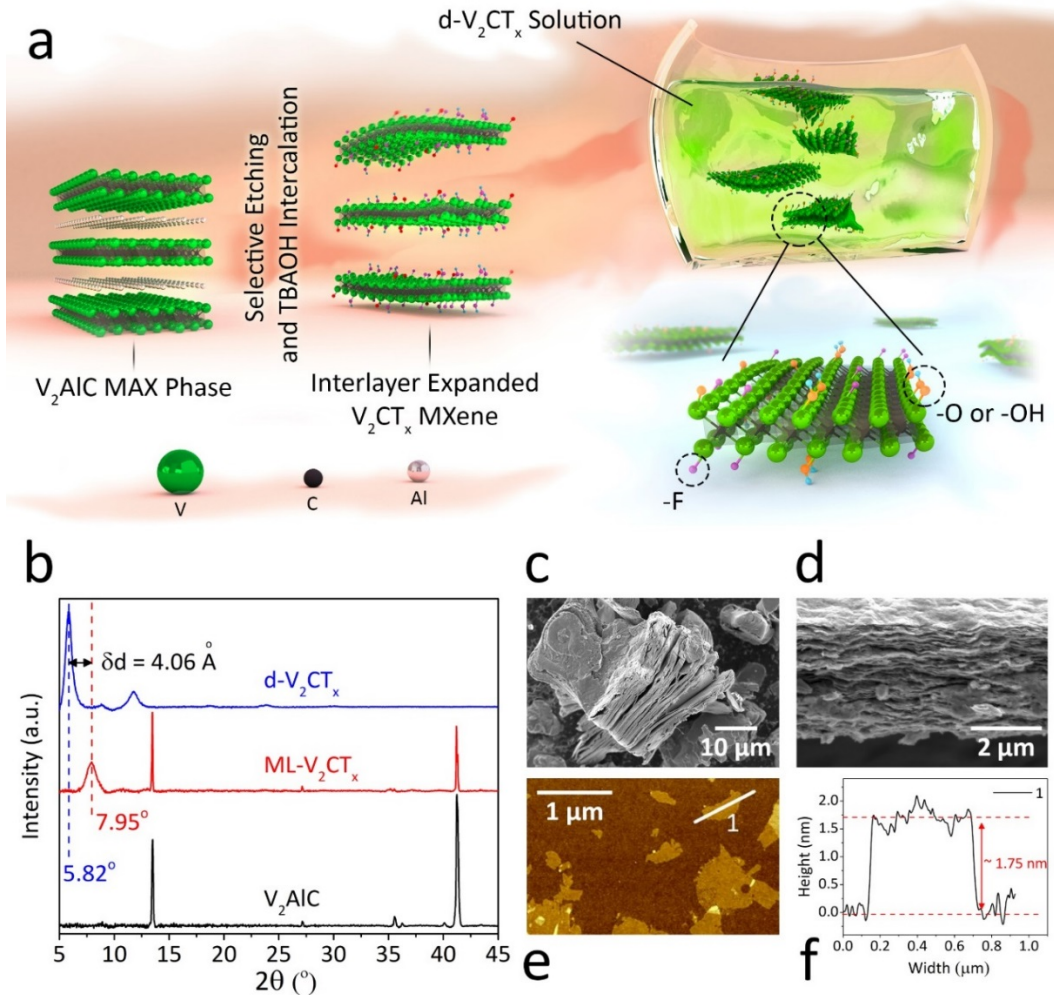
Figure 7.1. (a) Schematic illustration of the synthesis and delamination of V_2CT_x MXene showing the structure V_2AlC MAX and the resulting surface-functionalized V_2CT_x MXene. (b) XRD patterns of V_2AlC MAX phase and ML-V_2CT_x and d-V_2CT_x MXenes. After etching, a peak at around 7.95º appeared in the XRD pattern of the ML-V_2CT_x, corresponding to (0002) planes of MXene. Complete delamination of V_2CT_x after TBAOH intercalation, resulted in a downshift of (0002) peak to ~5.82º corresponding to 4.06 Å increase in the d-spacing of MXenes. (c) SEM

image of the ML-V_2CT_x. (d) SEM image of d-V_2CT_x films produced by vacuum filtration. (e) and (f) AFM image and the corresponding height profile of d-V_2CT_x flakes.

Figure 7.1 (a) schematically shows the synthesis method used to prepare d-V_2CT_z MXene. First, V_2AlC MAX phase was treated in hydrofluoric acid (HF) solution to selectively etch Al atoms from its structure. After completion of the etching process, the resulting powder is multilayered (ML) V_2CT_z that cannot be directly delaminated to 2D MXene flakes. To reduce the interactions between individual MXene layers and delaminate V_2CT_X, the ML-V_2CT_x was intercalated by tetra n-butyl ammonium ions (TBA$^+$) as explained in the experimental section. The intercalated MXene powders were dispersed in water and the dispersion was shaken by hand to complete the delamination process and prepare a stable solution of d-V_2CT_x, which was directly used for device fabrication. As shown in figure 7.1 (b), for the films fabricated using d-V_2CT_x, the XRD peak corresponding to (0002) planes of MXenes shifts to ~ 5.82° (from 7.95° for the ML-V_2CT_x), corresponding to 4.06 Å and 8.12 Å increase in the d-spacing and c-lattice parameter (c-LP), respectively. All residual MAX phase peaks were also diminished in the XRD pattern of the d-V_2CT_x films which further confirms successful delamination and absence of any residual and unreacted MAX phase impurities in the final d-V_2CT_x dispersion. Figure 7.1 (c, d) show scanning electron microscopy (SEM) images of the ML-V_2CT_x particles and cross-section of d-V_2CT_x films, respectively. SEM images present a typical accordion-like structure for ML-V_2CT_x and stacked layered structure for the delaminated MXene films. Atomic force microscopy (AFM) studies of samples prepared by drop casting of an aqueous dispersion of d-V_2CT_x on Si substrate showed that produced MXenes are mostly single-layer flakes with a thickness of ~1.75 nm as shown in figure 7.1 (e, f).

93
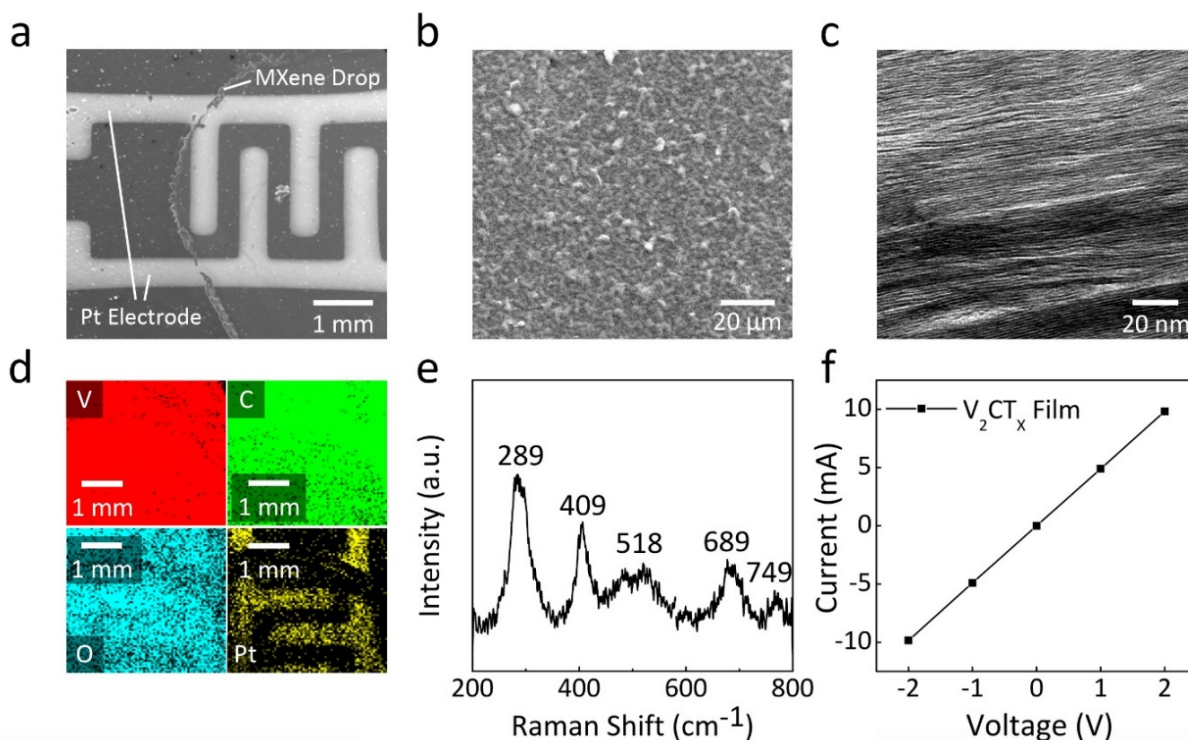
Figure 7.2. Morphology, structure and electrical characterization of V_2CT_x films. (a) Scanning electron microscopy (SEM) image of the V_2CT_x film deposited on interdigitated platinum electrodes by drop casting. (b) Magnified top view of a V_2CT_x film. (c) Transmission electron microscopy (TEM) image of the cross-section of a V_2CT_x film. (d) Energy-dispersive spectroscopy (EDS) mapping of a V_2CT_x film. (e) Raman spectroscopy of V_2CT_x film. (f) I-V measurement plot of a V_2CT_x film by two-electrode method.

Figure 7.2 shows a summary of various structural and spectroscopic analyses and electrical characterization performed on the V_2CT_x films. The SEM image of a V_2CT_x sensor fabricated by drop casting of one droplet of the d-V_2CT_x dispersion onto interdigitated platinum electrodes is shown in figure 7.2 (a). The hydrophilic nature of V_2CT_x flakes, resulting from the presence of -O and -OH surface functional groups on the surface of MXene flakes, enables the uniform deposition

94

of MXene films on the polyimide substrate[165]. The corresponding high magnification view of the fabricated V_2CT_x film is shown in figure 7.2 (b). The sensor platform was uniformly coated with d-V_2CT_x and the flakes had randomly networked and covered the 400 µm gap of the interdigitated platinum electrodes, electrically bridging the two electrodes. The cross-sectional TEM image of the deposited V_2CT_x film in figure 7.2 (c) shows that that individual MXene layers are uniformly stacked onto each other in the film. This ordered stacking of MXene flakes is very similar to what is usually observed for the films produced by vacuum filtration. Therefore, the deposited MXene films could show good in-plane and transversal electrical conductivity between the two platinum electrodes of the device. AFM measurements showed that the thickness of the deposited V_2CT_x film was ~200 nm. The EDS analysis of deposited V_2CT_x film as shown in figure 7.2 (d) confirmed the presence of vanadium, carbon, and oxygen and absence of aluminum. Figure 7.2 (e) shows the result of Raman spectroscopy of a deposited V_2CT_x film. The observed Raman spectrum showed a good agreement with the previously reported Raman data in the literature[166]. The peaks at 289 cm^{-1} (E_g) and 409 cm^{-1} (A_{1g}) correspond to in-plane and out-of-plane vibration of V atoms, respectively. The small deviation of the peak positions from the theoretical values[166] is believed to be due to the presence of the surface functional groups as they can significantly affect the normal-mode frequencies by weakening the vibration of the V atoms[166]. Additionally, the two humps in high frequencies can arise from the randomly stacked V_2CT_x film with intrinsic defects. Good electrical conductivity between the V_2CT_x film and platinum electrodes was verified using two-electrode I-V measurement. Figure 7.2 (f) shows the I-V polarization plot of the V_2CT_x based sensor in the range of -2V to 2V. The contact between V_2CT_x film and platinum electrodes showed an ohmic-behavior.
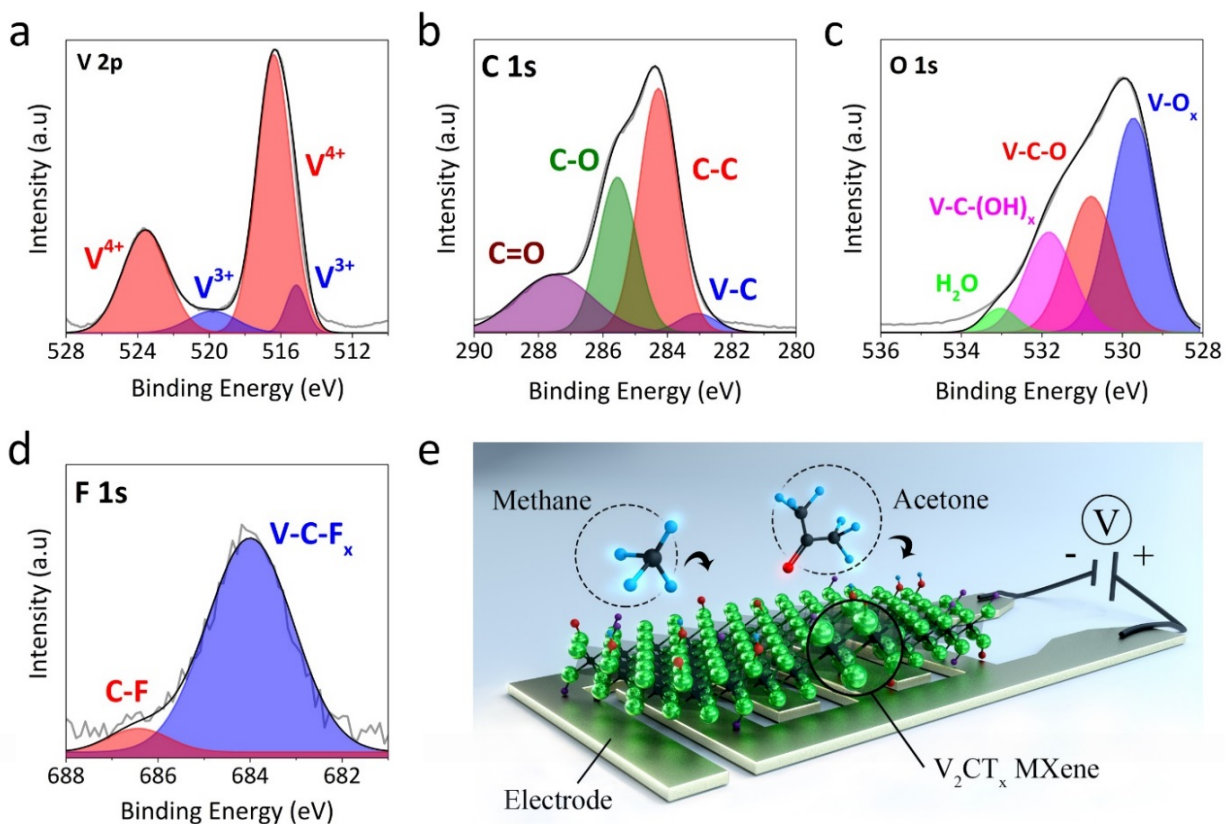
Figure 7.3. High Resolution XPS spectra of V_2CT_x. (a) V 2p region, (b) C 1s region, (c) O 1s region, and (d) F 1s region. (e) Schematic drawing showing the suggested sensing mechanism for the V_2CT_x gas sensor.

Surface chemistry can significantly impact the physical and chemical characteristics of a material, which are directly associated with the sensing properties[90]. The surface of MXene flakes after etching and delamination becomes very active due to the presence of the F, O, and OH surface groups[167]. To investigate the types and relative amounts of the functional groups on the surface of d-V_2CT_x, X-ray photoelectron spectroscopy (XPS) was carried out on the deposited V_2CT_x films. As shown in figure 7.3, XPS analysis confirmed the presence of V, C, O, and F elements. The

specific quantities of these surface groups are strongly dependent on the synthesis method[168]. In figure 7.3 (a), a high-resolution spectrum of the V 2p region shows the presence of vanadium, mostly in its V^{4+} oxidation state at a binding energy of 516.39 eV, in a good agreement with previous reports in the literature[78, 169]. The high valance state of vanadium in the V_2CT_x has been cited to be because of the presence of oxygen-containing surface groups and an oxide monolayer at the surface of MXene layers[78, 169]. Also, a very small amount of V^{3+} species was present at 515.3 eV. Figure 7.3 (b) shows the deconvolution of the XPS spectrum for the C 1S region. We attribute the presence of C-C and C-O components in the C 1S spectra to the adventitious contamination which are usually observed in the spectral of MXenes[73]. The C-C components corresponding to the V_2C lattice was observed at 283.07 eV. Its intensity, however, is very low due to the presence of carbon contaminants as well as oxycarbide terminations on the surface of MXenes[73]. O 1s XPS region and its corresponding deconvolution are shown in figure 7.3 (c). XPS analysis showed peaks related to V-O, V-C-O, V-C-(OH)$_x$, and H_2O components. These components can be related to the oxygen and hydroxyl functional groups, interlayer water, and possible vanadium oxide (VO_x) species present as the result of partial surface oxidation of MXenes[169-171]. V_2CT_x MXene, particularly in its delaminated form, might be partially oxidized at its surface in ambient atmospheres and form vanadium oxide and oxycarbide surface layers[69, 169]. The F 1s region of the XPS spectrum (Figure 7.3 (d)) showed F components related to fluorine termination of MXenes as well as residual carbon-fluoride bonds at 683.99 eV and 686.43 eV, respectively. Similar to our previous work on $Ti_3C_2T_x$ MXene, we suggest that the oxygen terminal groups on the surface of V_2CT_X flakes significantly contribute to the function of the receptor as shown schematically in figure 7.3 (e). Generally, surfaces terminated with hydrophilic groups are more favorable for the adsorption of ionic species than those having hydrophobic groups. Accordingly, the presence of

fluorine groups on the surface of MXene is not desirable for the absorption of gas molecules[81]. However, the XPS analysis revealed that the amount of fluorine in the synthesized V_2CT_x flakes was considerably lower compared to oxygen (1.02 atomic % of F 1S photoemission compared to 38.76 atomic % of O 1S photoemission). It is noteworthy that previous studies by ^{1}H nuclear magnetic resonance spectroscopy (NMR) have verified the presence of hydroxyl groups on the surface of V_2CT_x MXenes[172]. The contents of -O and -OH functional groups on the surface of V_2CT_x MXene was significantly higher than -F terminations, minimizing the possible negative effects arising from the presence of -F groups. We believe that the -O and -OH functional groups can be considered as the main contributors to the high gas adsorption capability of V_2CT_x.

7.3. Gas sensing performance
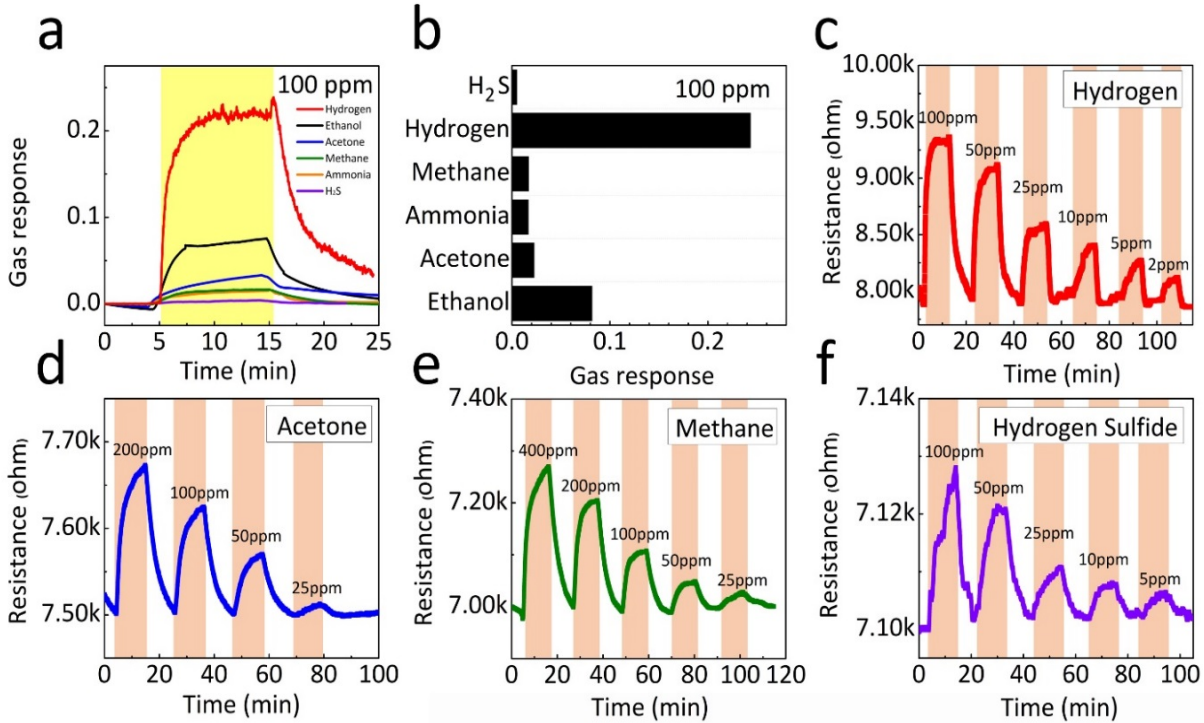
Figure 7.4. Gas sensing properties of a V_2CT_x sensor at RT (23 °C). (a) The compiled resistance variation and (b) gas response toward 100 ppm of hydrogen, ethanol, acetone, methane, ammonia, and hydrogen sulfide at RT. Real-time sensing response of V_2CT_x gas sensors at varying concentrations of (c) hydrogen, (d) acetone, (e) methane, and (f) hydrogen sulfide.

The gas sensing properties of a V_2CT_x sensor toward various gases were investigated at room temperature (23 °C). After stabilizing the baseline, the V_2CT_x film was exposed to the analyte for 10 min which is shaded in figure 7.4 (c-f) and followed by a flow of synthetic air for the recovery. The initial resistance of a deposited V_2CT_x film with 200 nm thickness was around 7-10

99

kΩ at RT. The measured base resistance of the deposited V_2CT_x films suggests its semiconductive property probably due to the effects of surface functional groups and the contact resistance between the individual flakes[80, 173]. Figure 7.4 (a) shows that the compiled resistance changes of the V_2CT_x film toward 100 ppm of hydrogen (H_2), ethanol (CH_3CH_2OH), acetone (CH_3COCH_3), methane (CH_4), ammonia (NH_4), and hydrogen sulfide (H_2S) chemical species at RT. The resistance of the V_2CT_x sensor was increased for all reducing analytes and recovered after stopping the gas injection. The sensing mechanism of this new material is still under the debate. For several sensing materials with high metallic properties, different sensing mechanism might be expected[157]. However, we believe that our V_2CT_x sensor with several kΩ base resistance showed p-type sensing characteristic by the charge transfer between surface terminal groups of V_2CT_x and analytes, as proposed in our previous MXenes gas sensor study[7]. The response of the device to analyte gases depends on the adsorption and desorption kinetics of the sensing species on the surface of the functionalized V_2CT_x film. The oxygen-containing functional groups such as hydroxyl on the surface of the V_2CT_x film can be responsible for physical or chemical interaction between the adsorbent and the adsorbate, which results in the observed modulated resistance of the system. For instance, computational studies have revealed that methane, which is more stable than H_2, can be absorbed physically on the surface of oxygen-terminated MXenes at RT[174].

To examine the sensing response comparatively, gas responses of the V_2CT_x sensing devices toward 100 ppm of various reducing gases were averaged out in figure 7.4 (b). The gas response was defined as the relative ratio of ($\frac{|R_g - R_a|}{R_a}$) where R_g is the resistance of V_2CT_x film under the exposure with an analyte and R_a is the resistance of V_2CT_x film under synthetic air flow. The typical gas response of the V_2CT_x film was calculated to be 0.0816, 0.0226, 0.0166, 0.0167,

0.2435, 0.005 for ethanol, acetone, ammonia, methane, hydrogen, and hydrogen sulfide, respectively, under ambient humidity (52 %). Among these analytes, the highest gas response was obtained for hydrogen showing excellent selectivity, and second highest was from ethanol. Compared to sensors fabricated using $Ti_3C_2T_x$ MXene in our previous work, the overall gas sensing response of V_2CT_x MXene was slightly better toward the four tested volatile organic compound (VOC) gases of ethanol, methanol, acetone, and ammonia.[7] This may be related to the difference in binding strength of the gases on the functionated V and Ti atom layers on the surface of these MXenes. DFT calculations have shown that the binding strength of various gases (H_2, H_2O, H_2S, N_2, NH_3, NO, NO_2, CO, CO_2, and SO_2) on O-functionalized V_2C is stronger than that of O-functionalized Ti_2C MXene, which has the same surface structure as O-functionalized Ti_3C_2 .[175] In addition, the selectivity of the two different carbides is quite different. Ti_3C_2T shows a high response to ammonia,[7] while V_2CT_x showed more selectivity toward hydrogen. Since the two MXenes have similar surface terminations the higher selectivity of the V_2CT_x device toward hydrogen is likely related to its surface transition metal (V atoms), which is in a good agreement with the selective detection of gas sensors based on vanadium oxide and V-doped metal oxides towards hydrogen[176-178]. Assuming same random surface termination of two MXenes, it should be highlighted that constituent elements of MXenes strongly influence on bonding strength, resulting in selectivity. Figure 7.4 (c-f) show the gas sensing performance of the V_2CT_x device with decreasing concentrations of hydrogen (2 – 100 ppm), acetone (25 – 200 ppm), methane (25 – 400 ppm), and hydrogen sulfide (5 – 100 ppm). The positive gas response was maintained toward four analytes at all ranges of concentration, and their response was gradually decreased when the concentration reduced to lower values. It should be highlighted that the V_2CT_x sensing device demonstrates the capability to detect trace amounts of VOC gases and non-polar gases at RT

without any additional surface treatment or novel metal decoration. In particular, our results show the superior sensing capability and response of V_2CT_x compared to other 2D materials detecting hydrogen[179-180] and methane[181] gases at RT.
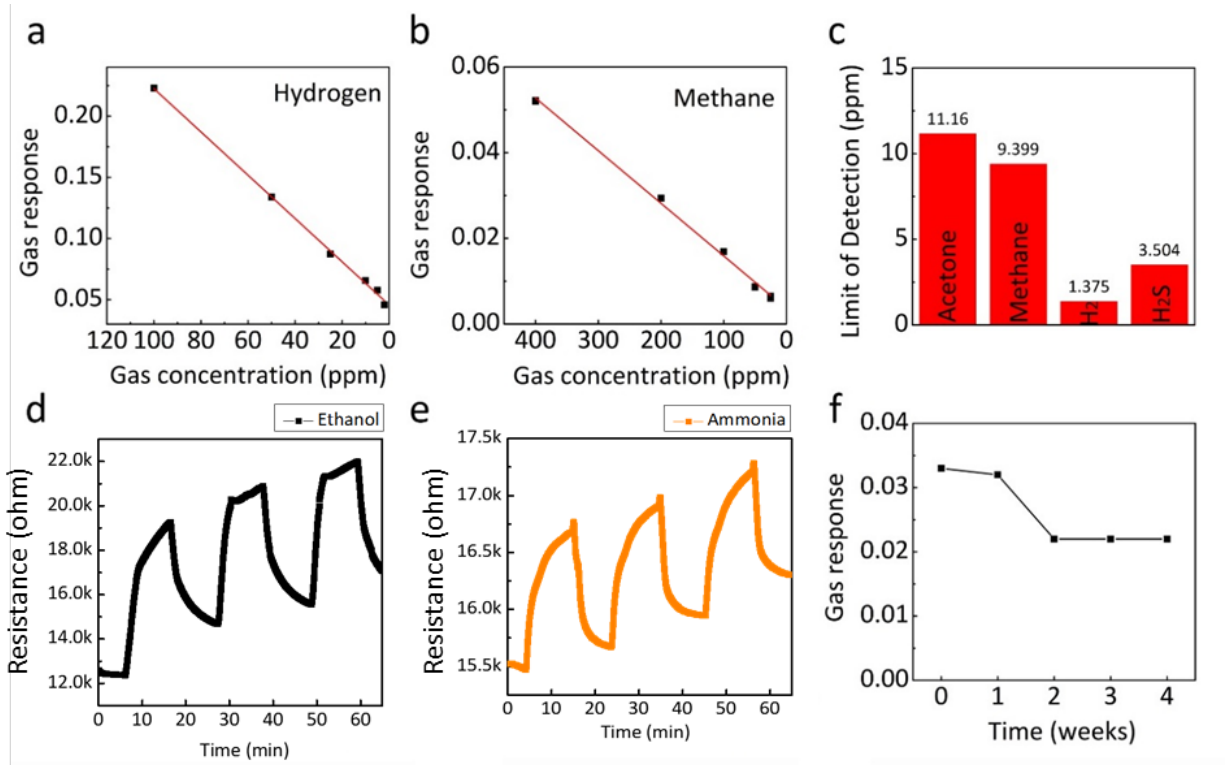
Figure 7.5. Relationship between gas response and concentration of (a) hydrogen (6-200 ppm) and (b) methane (25-400 ppm) analytes at RT (23 °C). (c) Theoretical Limit of Detection (LoD) based on signal-to-noise (S/N) ratio of 3. Its reproducibility under the ambient humidity toward (d) ethanol and (e) ammonia. (f) Gas response variation of a V_2CT_x sensor to ammonia at RT over a month under ambient condition.

We also investigated V_2CT_x sensor's limit of detection (LoD) described as the lowest concentration of analyte that can be reasonably differentiated from the noise, toward hydrogen,

acetone, methane, and hydrogen sulfide analytes. Average gas response at each concentration was calculated, and then the theoretical LoD was also computed with the signal-to-noise ratio (S/N>3). Figure 7.5 (a,b) exhibit the gas response of V_2CT_x film and linear fitting drawn as a function of gas concentration toward hydrogen and methane, respectively. In the same way, the relationship between gas response and the concentration of acetone (25 – 200 ppm) and hydrogen sulfide (5 – 100 ppm) is calculated. As shown in figure 7.5 (c), the theoretical LoD of V_2CT_x film toward acetone, methane, hydrogen, and hydrogen sulfide at RT was found to be 11.16, 9.39, 1.375, and 3.504 ppm, respectively. It should be noted that the sensitive detection of methane at RT has been rarely achieved with other materials before. This is because methane is an extremely difficult analyte to detect at RT owing to its non-polarity and high enthalpy of the C-H bonds[149]. Nevertheless, it is noticeable that our V_2CT_x gas sensor can identify non-polar gases within single ppm ranges at RT. Table 7.1 compare the performance of V_2CT_x with the state-of-the-art gas sensors based on other materials tested at RT for detecting methane and hydrogen. For both hydrogen[150, 182-187] and methane[118, 135, 149, 188-191] analytes, the LoD of V_2CT_x gas sensor is either lower than or comparable with gas sensors fabricated with carbon-based materials, vanadium oxide, or 2D transition metal dichalcogenides (TMDs). These results indicate that V_2CT_x is highly attractive as an RT sensing material over others (such as metal oxide hybridized TMDs and novel metal decorated carbon-based materials). Further enhancement of the sensing properties of the 2D V_2CT_x gas sensor should be possible by hybridization of MXenes with metal oxide and novel metal particles which might enable an extremely low level of detection (ppb or ppt) of non-polar analytes. Moreover, 2D V_2CT_x gas sensor showed high ambient stability and reliable sensing performance for a long period. Its reproducibility under the ambient humidity was also confirmed without degradation as shown in figure 7.5 (d,e). The absence of structural changes and degradation of

V_2CT_x MXene upon gas absorption, suggests its reusability for gas sensing applications. For example, as it is shown in figure 7.5 (f), over a month of operation, the gas response and functionality of the V_2CT_x device were maintained almost the same under ambient atmosphere. This also suggests that once V_2CT_x is deposited and dried, its oxidation would be subsided due to the absence of water which is a known mild oxidant of MXenes[192].

Table 7.1. State-of-the-art performance of the empirical limit of detection (LOD) for room temperature sensors based on other sensing materials toward hydrogen and methane.

Analyte	Sensing material	Empirical Limit of Detection (LoD)	Working temperature (°C)	Reference
Hydrogen	V_2CT_x MXene	2 ppm	RT	This Work
	Pd decorated Carbon nanowires	10 ppm	RT	182
	rGO/GaN	20 ppm	RT	183
	GO/Porous Silicon	200 ppm	15	150
	WS_2 - Pd composite	10 ppm	RT	184
	Pd-SnO_2/MoS_2 ternary hybrid	30 ppm	RT	185
	Pd functionalized MoS_2	50 ppm	RT	186
	UV-Activated MoS_2	500 ppm	RT	187
Methane	V_2CT_x MXene	25 ppm	RT	This Work
	Graphene /Polyaniline Nanocomposite	10 ppm	RT	118
	MWCNT/Vanadium filling	20 ppm	RT	188
	Vertical graphene/ SnO_2	1000 ppm	RT	189
	GO	10000 ppm	RT	149
	rGO/ SnO_2	10000 ppm	RT	149
	VO_2 nanorods	100 ppm	RT	190
	Au-decorated vanadium oxides (VO_x)	500 ppm	RT	193
	Pt-decorated vanadium oxide (VO_x)	500 ppm	RT	191

RT = Room temperature, rGO = reduced graphene oxide, MWCNT = Multi-Walled Carbon Nanotube.

7.4. Conclusions

In summary, we have demonstrated 2D V_2CT_x gas sensors with outstanding gas sensing performance and ultrahigh sensitivity toward non-polar gases at RT. Single/few-layers V_2CT_x MXene flakes synthesized through a selective etching and intercalation process were drop-casted on polyimide sensor platforms. The fabricated 2D V_2CT_x gas sensors were able to detect trace amounts of various gases including non-polar gases such as hydrogen and methane. The theoretical LoD for hydrogen was 1 ppm and that of methane was 9 ppm at RT, which is the lowest among the reported values for all 2D materials and vanadium-based metal oxides prepared without any treatment. We suggest that the excellent gas sensing performance of the 2D V_2CT_X device is related to the surface oxygen functional groups present on the surface of V_2CT_X nanoflakes. Through the comparison of sensing properties with $Ti_3C_2T_x$, it concluded that transformation of ordered structure and constituent elements of MXenes play an important role in interaction between analyte and MXenes showing outstanding selectivity and LoD toward non-polar gases, which was comparable to other graphene relatives and TMDs. Our work can lead to new gas sensor devices based on MXene materials for a safe and ultrahigh sensitive detection of non-polar analytes at RT.

Chapter 8. Investigation of Hybrids Constituting of 2D Nanomaterials and Metal Oxides

8.1. Introduction

In accordance with wearable applications, 2D nanostructured materials have been explored as alternative materials instead of metal oxide. Due to their distinct physical and chemical characteristics, 2D nanostructured materials have successfully decreased the sensing temperatures up to room temperature (RT, 25 °C) and their sensing performance has been progressed[30, 194]. Among many 2D nano-materials, there has been much research toward graphene and graphene oxide (GO) for gas sensing applications owing to their large specific surface area and potential binding sites[40-41]. Modified GO has been more frequently utilized than pure GO. Since oxygen functional groups of GO play a role of both reaction sites and reduction electrical conductivity, the number normally has been balanced through reduction processes[43, 195-196]. GO or reduced GO (rGO) has demonstrated RT sensing ability with good sensing performance. However, the GO sensors operating at RT show the major drawbacks of the sluggish or irreversible recovery and lack of long-term stability, which should be further refined[43].

One approach to improve the performance of GO sensor was to incorporate GO with metal oxides[197-198]. Similar to metal oxide composites, hybridizing 2D material and metal oxide can be postulated to have syntagmatic benefits for sensing performance. By compositing GO and metal oxide nanoparticles, synergistic effects combined from each material might be facilitated, resulting in enhanced gas sensing performance as well as reduced cost[29]. Recent literatures have studied various metal oxide nanoparticles as a second material in the graphene matrix, and the

106

representative metal oxides are SnO_2, ZnO and WO_3[86, 199]. Depending on the choice of the second material, diverse sensing performances such as gas response and selectivity were improved. However, a clear explanation of the sensing behavior of the composite has not been established[199]. Therefore, the further study should be implemented to understand the sensing mechanism and physics behind performance improvement. Although the photocatalysis of GO/TiO_2 has been well-investigated[200-201], relatively less effort has been dedicated to the investigation of gas sensing properties of GO and TiO_2 hybridization. Few papers have been reported on RT gas sensing results of rGO decorated TiO_2 through hydrothermal method[97-98]. Furthermore, few studies have investigated the gas sensing properties of GO/TiO_2 composite combined with photocatalytic effect. Hence, it would be worthwhile to explore the gas sensing properties of the GO/TiO_2 composite in company with the photocatalytic effect of TiO_2.

8.2. Material characterization
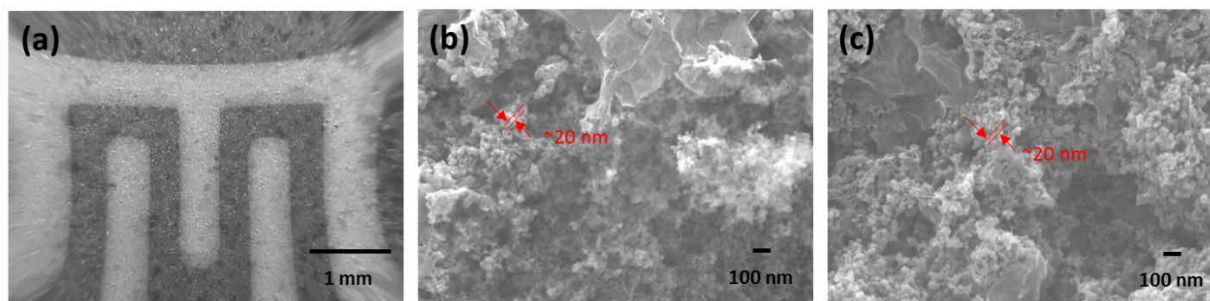
Figure 8.1. SEM images of GO/TiO_2 composite in (a) low magnified view and high magnified view (b) before UV irradiation and (c) after 2 hours UV irradiation.

The morphology of the hybridized GO nanoflakes and TiO_2 nanoparticles was observed by SEM. Figure 8.1 (a) shows the dried film of GO/TiO_2 composite after drop casting onto the sensor platform of the polyimide film. The two mixed materials uniformly filled up the gap of the interdigitated electrode. In a magnified view of (b), it is observed that GO nanoflakes and TiO_2 nanoparticles were tangled. The size of TiO_2 nanoparticles was confirmed to be around 20 nm. The wrinkled morphology of GO sheets was due to sp^3 bonding of the oxygen-containing groups on the GO surface. Figure 8.1 (c) shows the magnified view of GO/TiO_2 composite film after 2 hours UV treatment in solution. The randomly mixed GO nanoflakes and TiO_2 particles from UV treated composite showed similar morphology with the sample before UV irradiation. When GO is coupled with TiO_2, the carboxyl group on the GO surface could bond with the hydroxyl group on the TiO_2 surface, and the charge transfer under UV irradiation could result in photoreduction of GO[114]. The combination of GO and TiO_2 was sustained after UV irradiation, which suggests that the coupled structure is unaffected by UV energy[202]. Besides, the size of TiO_2 nanoparticles was not grown or congregated, which is usually observed by heat processes[203].
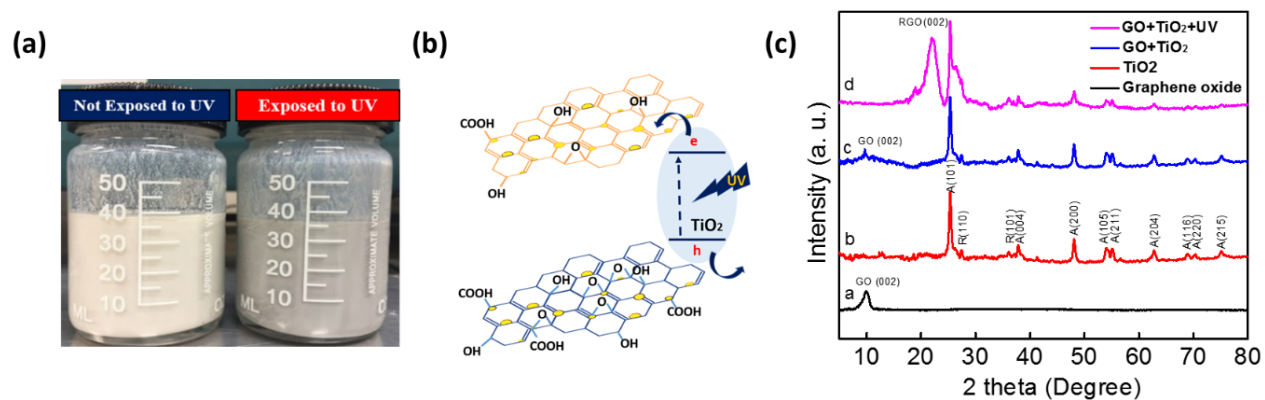
Figure 8.2. (a) the photograph of GO/TiO$_2$ composite before and after UV exposure. (b) the schematic diagram of GO/TiO$_2$ composite under the UV effect. (c) XRD spectra of the prepared a) GO, b) TiO$_2$, GO/TiO$_2$ composite c) before, and d) after UV exposure.

Figure 8.2 (a) is the photograph of the composite solution where GO nanosheets were mixed with TiO$_2$ nanoparticles in ethanol. The left bottle is the mixed solution before UV irradiation, and the right bottle is that after 2 hours UV irradiation. Since both TiO$_2$ and GO carry surface charge in suspension, they can easily disperse in the solution and be stable for several hours. After several days, the mixture sank especially for the UV treated solution. However, it can be suspended again by mild ultra-sonication or stirring. After UV exposure, the obvious change in color from white to gray was observed, which indicates that GO was photo-catalytically reduced(rGO). This color difference originates from the restoration of sp^2 bonds from sp^3 bonds by removing oxygen functional groups on the surface of GO nanosheets[204]. Figure 8.2 (b) presents the photocatalytic reduction mechanism of GO with TiO$_2$ nanoparticles under the UV irradiation. When UV light, which has a photon energy larger than the band gap of TiO$_2$, was exposed to the composition solution, electrons and holes in TiO$_2$ nanoparticles were separated. In the presence of

ethanol, the holes are transferred to ethanol, which generates ethoxy radicals of ethanol. Corresponding electrons are crossed to GO, eliminating certain amounts of oxygen functional groups[205]. The following Eq. (9,10) indicate the photocatalytic reduction process[202].

$$TiO_2 + hv \rightarrow TiO_2(h + e) \; in \; C_2H_5OH$$

$$\rightarrow \; TiO_2(e) + \; C_2H_4OH^{\cdot} + \; H^+ \; \text{Eq. (9)}$$

$$TiO_2(e) + GO \; \rightarrow \; TiO_2 + rGO \; \text{Eq. (10)}$$
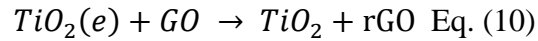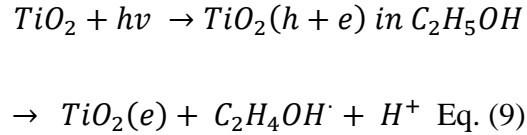
The successful photo-reduction of GO with the presence of photocatalyst was confirmed by X-ray diffraction (XRD) in figure 8.2 (c). A distinct peak of GO ($2\Theta = 10°$)[206] and anatase/rutile TiO_2 (JDPDS 21-1272, 21-1276) are clearly observed in figure 8.2 (c). In the XRD pattern of TiO_2, the average size of nanoparticles calculated from the Scherrer equation (FWHM = 0.136°) was about 23 nm, which is consistent to SEM result. For simple mixture of GO and TiO_2, each peak from GO and TiO_2 were collectively shown, however, the typical peak of GO seems a small hump due to crystallized peak of TiO_2. After UV exposure to GO and TiO_2 solution, a new diffraction peak belonging to rGO is observed at $2\Theta = 24°$, and a peak of GO centered at $2\Theta = 10°$ disappeared[207]. This result indicates that the UV treatment can be an effective method for the reduction of GO to rGO.
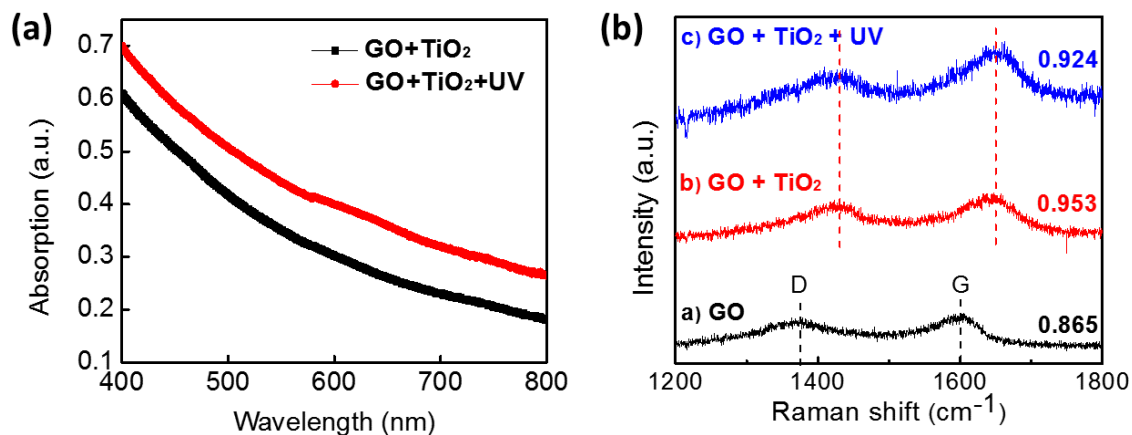
Figure 8.3. (a) UV-vis absorption spectra of GO/TiO$_2$ composite before and after UV irradiation. (b) Raman spectra of a) GO, b) GO/TiO$_2$ composite, and c) GO/TiO$_2$ composite with UV irradiation.

UV-visible (UV-vis) spectroscopy and Raman were employed to further investigate the effect of UV by characterizing of the composite. Figure 8.3 depicts the UV-vis spectra of the composite with the absence and presence of UV irradiation in the range of 400 nm to 800 nm. For both samples, UV absorption was decreased as the wavelength increased. With UV treated solution, absorption spectra were generally increased in the whole range. This indicates that the electronic conjugation was restored in the graphene sheet, which corresponds to the color change of the sample where UV treated composite looked darker in figure 8.3 (a). Figure 8.3 (b) shows the Raman spectra of a) GO, b) GO/TiO$_2$ composite, and c) GO/TiO$_2$ composite after UV irradiation. Raman spectroscopy can reveal information regarding the local structure of the composite and the quality of carbon structure. The main feature in the Raman spectra of graphene composite was assigned in the D band at 1375 cm^{-1} and G band at 1598 cm^{-1}[208]. Normally, the G band corresponds

to graphite structure as attributing to in-plain vibration of sp^2 bonded carbon domain[209]. The D band is contributed to sp^3 hybridized carbon bonds mostly due to the presence of structural defects as suggesting disordered crystalline carbon structure[210]. In this regard, the intensity ratio of the D band to the G band can describe an extension of the disorder or defects in carbon domain. In figure 8.3 (b), the value of I_D/I_G ratio is 0.865 in GO, 0.953 in the composite, and 0.924 in UV treated composite. In GO film, oxygen functional groups along with defects impute to sp^3 hybridization on sp^2 graphene matrix. Compared to the ratio of pure GO, the I_D/I_G ratio of the composite increased, which indicates that the composite has more sp^3 hybridized bonds. The increase might be associated with the introduction of TiO_2 nanoparticles. Possibly, when incorporating GO with TiO_2, some TiO_2 nanoparticles might create Ti-O-C bonds in GO plain, resulting in increased I_D/I_G ratio[210]. After UV irradiation, I_D/I_G ratio was decreased more compared to that without UV since the sp^2 bonds of GO were restored by photocatalysis of TiO_2. Along with UV-vis result, this confirmed that GO was photo-reduced by TiO_2 catalysis and the surface condition of the composite was modified. Meanwhile, the peak shift of both D and G bands were obviously observed after hybridizing GO and TiO_2 as shown in figure 8.3 (b). It is indicated that a peak shift can be observed when materials are under the stress and that a blue shift (higher wavenumber) can be induced by compression[200, 211]. As a result, blue shift of the bands can be interpreted that carbon atoms in GO are under the compression due to structural change induced by TiO_2 nanoparticles[212]. Correspondingly, the length of chemical bonds in GO can be modified by adding TiO_2 into GO. However, D and G band position were similarly maintained after UV treatment, which depicts no further structure change and chemical bonds.

8.3. Gas sensing performance
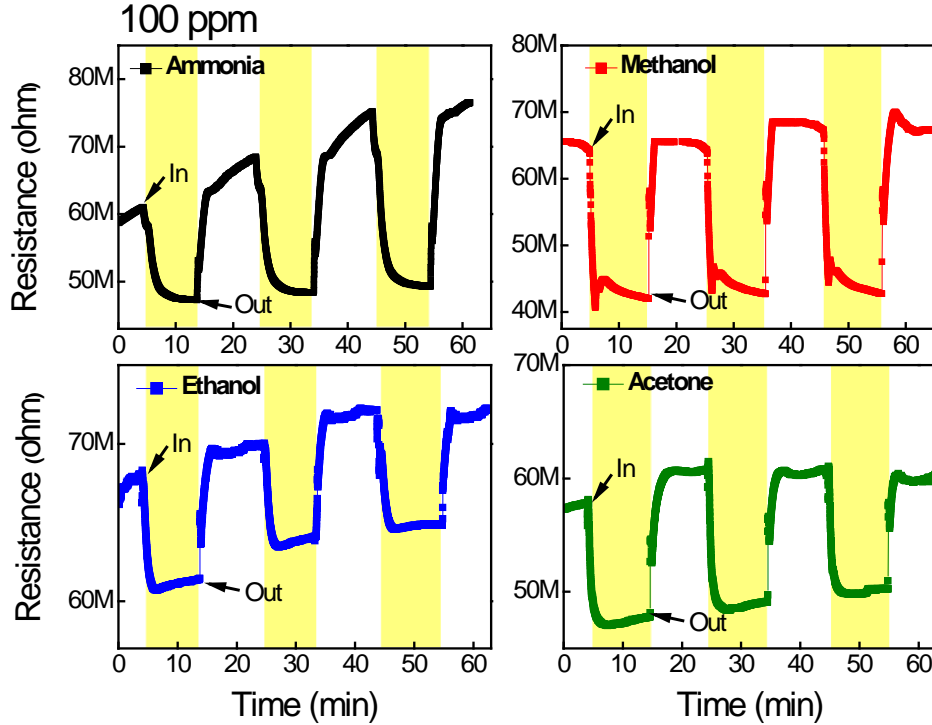
Figure 8.4. Gas sensing results of GO/TiO$_2$ composite film without UV irradiation toward 100 ppm ammonia, methanol, ethanol, and acetone gas bubbling at room temperature (25 °C).

The gas sensing properties of GO/TiO$_2$ composite were investigated in figure 8.4. This film was simply fabricated by powder mix in the solvent without any further treatment. Various reducing gases such as ammonia, methanol, ethanol, and acetone gases were introduced with the concentration of 100 ppm, and the gas sensing behavior of the composite was explored at RT. For the gas sensing test, the composite film was periodically exposed to target gases for 10 minutes followed by a flow of ambient air where 40 sccm of nitrogen and 20 sccm oxygen were mixed. As

113

shown in figure 8.4, the initial resistance of the composite was very high ranging from 60~70 MΩ because of the insulating property of TiO_2 at RT. The hybridized film exhibited n-type sensing behavior to the reducing gases. Upon introducing the target gas, the resistance of the film was dropped and then recovered to the initial resistance without the gas as showing n-type sensing behavior. Considering the RT sensing ability of 2D nanomaterial and the insulating property of metal oxide, it is expected that GO would play a role of dominant sensing material and networking TiO_2 nanoparticles[97]. On the other hand, TiO_2 might play a catalytic role to attract gas molecules by lowering the activation energy[97, 213]. Detecting methanol, ethanol, and acetone with high response can be attributed to the catalytic effect of TiO_2, while only ammonia was identified by pure GO film.
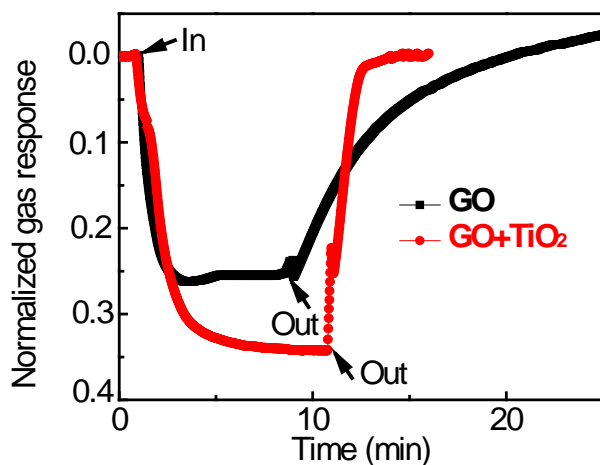
Figure 8.5. Comparative gas sensing results of pure GO and GO/TiO_2 composite toward 100 ppm ammonia gas bubbling at room temperature (25 °C).

To evaluate the gas sensing performance of the GO/TiO₂ composite, gas sensing results were compared to pure GO film in figure 8.5. The gas response was calculated as the ratio of $|R_a - R_g|/R_a$, where R_g is the resistance of the film under the target gas, and R_a is the resistance of the film under the ambient air. The gas response of pure GO film was found to be 0.23, and that of the GO/TiO₂ composite was 0.38. By combining 2D nanomaterial with metal oxide nanoparticle, the gas response against ammonia was improved. The recovery time of the composite was also compared to that of pure GO against ammonia gas. It was defined as the time to recover 90 % of resistance before gas injection. As shown in figure 8.5, the recovery time of GO towards ammonia is around 15 minutes, whereas that of the composite is 2 minutes. Even though the base resistance drift of both films existed, recovery time was obviously reduced in the composite structure. The enhanced response and reduced recovery time of the composite can be attributed to the creation of n-n junction at the interface and the catalytic sensitization of TiO₂ nanoparticles[214].
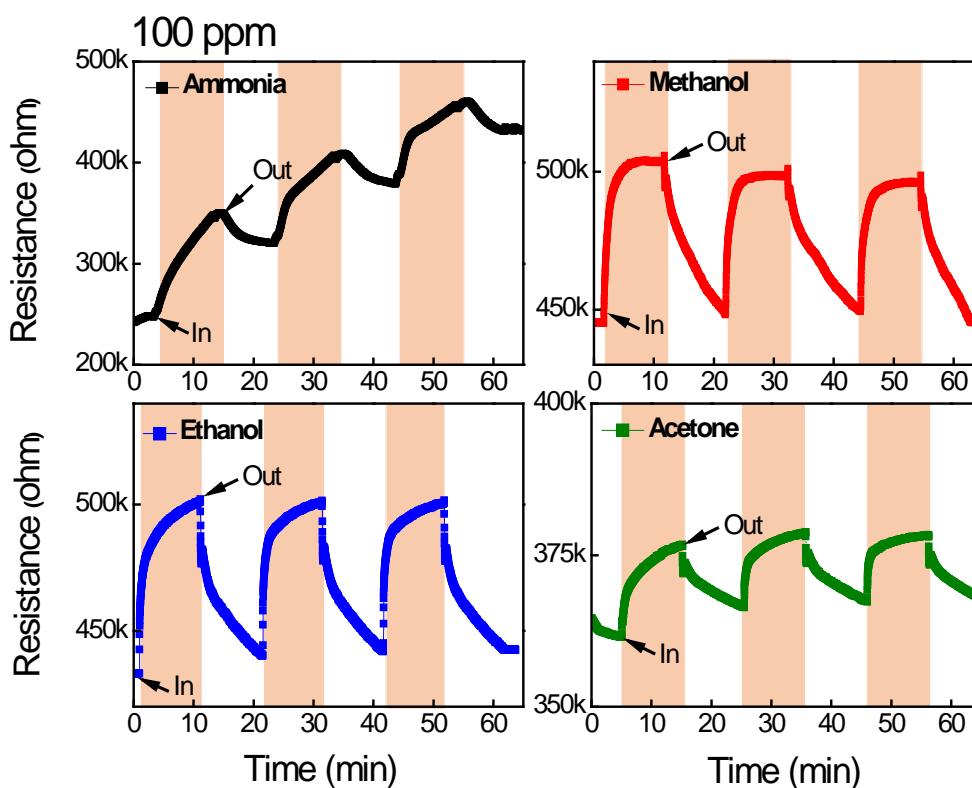
Figure 8.6. Gas sensing results of UV irradiated GO/TiO$_2$ composite toward 100 ppm ammonia, methanol, ethanol, and acetone gas bubbling at room temperature (25 °C).

During the fabrication process, UV light was irradiated to the composite solution for 2 hours, then the gas sensing properties of the dried TiO$_2$/GO composite film were investigated. The same reducing gases with the concentration of 100 ppm were utilized, and the sensing properties of the UV treated composite were explored at RT in figure 8.6. Since GO in the composite was photocatalytic reduced by UV irradiation, the initial resistance of the composite dropped to a 300-400 kΩ range. In contrast to the composite sample, the UV-treated sample exhibited p-type gas sensing behavior to the same reducing gases due to GO reduction. In the reverse way of n-type

sensing behavior, the resistance was increased when target gas was injected and then decreased

when it disappeared. In the middle of the two conditions, the 1hour UV treated composite sensor

did not react to any target gases, and this originates from the cancellation of the opposite sensing

behavior during n-p transition. Such sensing behavior transition provides empirical evidence for

ambipolar characteristic of GO or rGO[215-216]. By controlling the oxygen functional groups, GO can

have either a p-type or n-type sensing behavior[44, 216]. Furthermore, the sensing behavior conversion

concludes that the dominant sensing material of the composite at RT would be GO or rGO, and

TiO_2 acted as reactive sites to improve sensing performance.
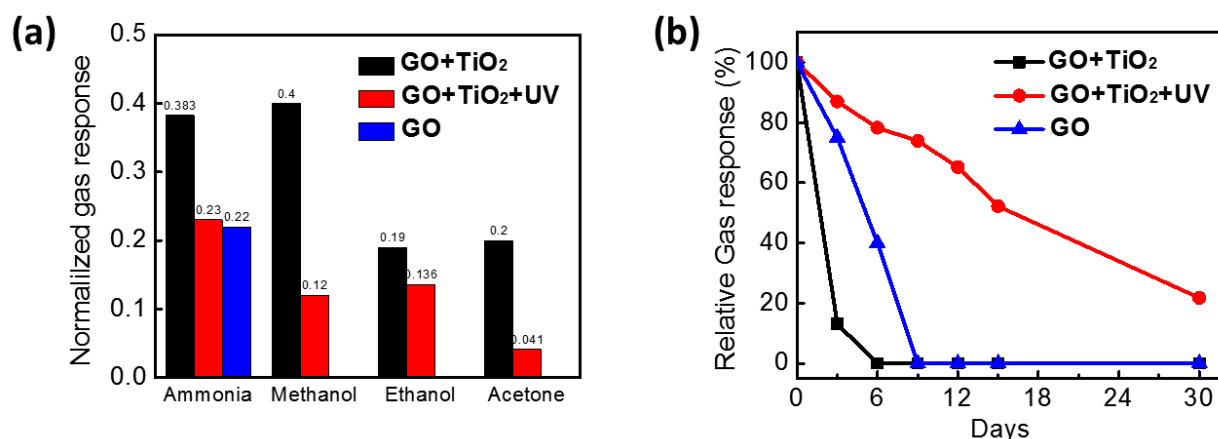
Figure 8.7. (a) The compiled gas response and (b) the long-term response of UV treated and non-

treated GO/TiO_2 composite film to ammonia gas.

The gas sensing performance of the hybridized samples was evaluated by incorporating the

photocatalysis effect. The gas response of the GO/TiO_2 composite to various gases was calculated

and plotted in figure 8.7 (a). The gas responses of the composite to ammonia, methanol, ethanol,

and acetone were 0.383, 0.4, 0.18, and 0.2 respectively. These value of gas response toward VOCs were higher than pure GO, rGO and novel metal decorated rGO due to synergistic effect of hybridization[41, 217-218]. In case of UV treated composite, the general gas responses to reducing gases decreased to 0.2, 0.12, 0.136, and 0.041. It has been well studied that the oxygen functional groups such as hydroxyl and epoxy groups of GO are essential to possess high gas response to target gases because they can easily absorb the gas molecules[30]. Since the number of oxygen functional groups on GO nanosheets was reduced from photo-reduction, the chance of interaction between functional groups and target gases was decreased resulting in lower gas response. Although the overall gas response of the photo-reduced composite was reduced compared to pure composite, this result is quite comparable to pure GO film. Figure 8.7 (b) presents the long-term stability of both composite gas sensors over a month. The GO/TiO$_2$ composite showed high gas response to ammonia than the UV treated composite, however, it maintained the function for a short time. The initial resistance of the composite sample was 70 MΩ at first and increased to over 100 MΩ after 3 days, resulting in no response to gases. The increased resistance is due to the fast oxidation of the composite as showing susceptibility to humidity. On the other hand, the UV-treated composite demonstrated that the sensor was able to work over a month at RT. Even though the response to ammonia gradually declined for a month, the response was reliable. This improvement might be due to the controlled amount of oxygen functional groups which easily reacted with water molecules in ambient atmosphere.

(a) Before contact

$\phi > 4.4\text{eV}$

$\phi = 4.2\text{eV}$

$\chi = 4.0\text{eV}$

Transfer

e e e e e E_{CB}

E_F

e e e e e E_{CB}

E_F

GO

E_{VB}

E_{gap} : 0.5eV

TiO$_2$

E_{VB}

E_{gap} : 3.2eV

(b) After contact

Depletion layer

E_{CB}

E_F

E_{VB}

e e e e e

GO

e e e e e E_{CB}

E_F

Accumulation layer

TiO$_2$

E_{VB}

(c) During UV irradiation

Depletion layer↑

E_{CB}

E_F

E_{VB}

e e e eee e

GO

e e eeee E_{CB}

E_F

Accumulation layer ↑

TiO$_2$

E_{VB}

h h hhh hh

(d) After UV irradiation

Depletion layer↓

E_{CB}

E_F

E_{VB}

rGO

h h h h

e e E_{CB}

E_F

TiO$_2$

E_{VB}
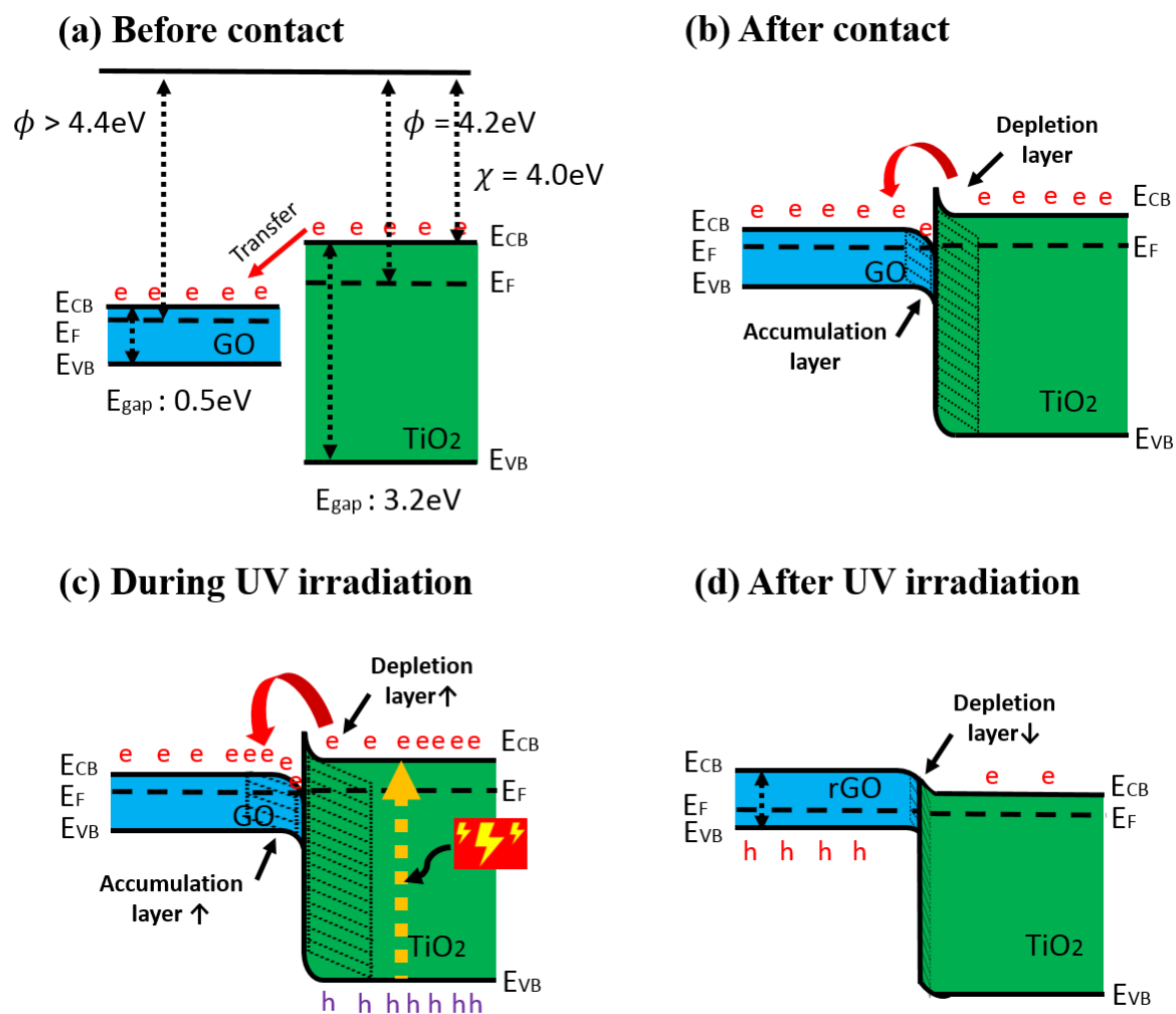
Figure 8.8. The proposed band diagram of GO/TiO$_2$ composite (a) before contact, (b) after contact, (c) during UV irradiation, and (d) after UV irradiation. (e: electron, h: hole)

The improved gas sensing performance of the composite could be attributed to the synergistic effect of GO and TiO$_2$ nanoparticles. Figure 8.8 (a,b) illustrates the proposed band diagram of GO/TiO$_2$ composite before and after contact. It is reported that the work function of graphene is 4.4 eV[200] and oxidation increases the work function of carbon-based materials such as

CNT and fullerene, as well as graphene[219]. In this work, the work function of GO was speculated to be higher than 4.4 eV, and it was estimated to be around 4.7 eV[220]. Contact between GO nanosheets and TiO_2 nanoparticles formed an n-n junction at the interface, and charge carriers were transferred from TiO_2 to GO. This resulted in an accumulation layer and a depletion layer as illustrated in Figure 8.8 (b)[221]. Due to the Schottky barrier, the depletion layer of TiO_2 was thicker, and the number of electrons in GO was increased at the interface. At RT, the main contribution of the resistance change in the composite sample was caused by the reaction between oxygen functional groups on GO and gas molecules. However, with excessive electrons transferred to GO, the electrostatic force, such as Van der Waals force, may enhance physisorption of the polar gases, which leads to enhanced gas response and faster recovery time compared to pure GO film. In addition, negatively charged oxygen adsorbates (O_2^-) on the surface of TiO_2 would support gas reaction by lowering activation energy to attract gas molecules as catalytically active sites during the sensitization process[98]. Structurally, TiO_2 nanoparticles helped to prevent GO from agglomeration and increase the number of reaction sites, which provide a higher chance to react with target gas[14, 113]. As a result, the GO/ TiO_2 sensor was able to measure various reducing gases, as well as ammonia gas, and improve gas performance such as higher response and faster recovery time.

Nevertheless, the long-term stability of the composite was degraded due to susceptibility to humidity in ambient atmosphere and high initial resistance. The large number of oxygen functional groups of GO and the oxygen adsorbates (O_2^-) of TiO_2 film cause dynamic interaction with humidity or contaminants, resulting in increased resistance. It has been studied that the ambient oxygen and moisture are easily absorbed on the surface of GO by oxygen functional groups, such as hydroxyl, and increase resistance[222]. Because the reactive sites become occupied

by moisture under ambient atmosphere, the function of the composite sensor cannot be maintained for a long time.

In order to improve stability of the composite sensor, the composite solution was UV treated, and its surface and junction was engineered during the UV irradiation. As mentioned in Eq. (9,10), electron-hole pairs were photo-generated in TiO_2, and excited electrons were transferred to GO under the exposure of UV light. During the UV irradiation, the accumulation layer of the GO and depletion layer of the TiO_2 could be temporarily increased at the interfaces as described in figure 8.8 (c). The excessive electrons shifted to GO were employed to restore π bonds of carbon structure by eliminating oxygenated groups and to remove moisture on the surface of GO. Accordingly, GO became photo-reduced, and the p-n junction might be formed with decreased junction width at the interface as shown in figure 8.8 (d). By integrating TiO_2 with GO, photolysis of TiO_2 was encouraged by injecting electrons into GO, and the recombination of electron-hole pairs in TiO_2 was effectively prevented[207].

As a result, the gas detection ability of the UV treated composite sensor was preserved over a month, and sensing behavior was altered from n-type to p-type. The number of oxygen functional groups of GO in the composite was adjusted by the photocatalysis of TiO_2. Thus the hydrophilic property of GO was curtailed, and relative hydrophobic property of rGO suppressed moisture absorption[223]. Moreover, the amount of oxygen adsorbates (O_2^-) on TiO_2 was diminished by the photo-active hole in Eq. (9), resulting in the reduction of moisture attraction[224]. The photo-induced effect on gas performance remained for over a month at the cost of slight sacrifice of gas response.

8. 4. Conclusions

The room temperature gas sensing performance of the GO/TiO$_2$ composite prepared on flexible polymeric film was enhanced by the effect of photocatalysis of TiO$_2$ under UV. By incorporating TiO$_2$ to GO, the surface condition of GO was tailored, and Schottky barriers were created at the interface. As a result, detection of various reducing gases was enabled with an aid of TiO$_2$ nanoparticles, and the recovery time was quite reduced compared to pure GO film. However, the long-term stability remains as an unsolved problem due to susceptibility to humidity. To solve the stability issue of the sensor, the GO/TiO$_2$ composite solution was UV treated, and the surface and hetero-junction of the composite was modulated. Due to photocatalytic effect of TiO$_2$ under UV irradiation, electrons were transferred to GO, resulting in the photo-reduction of GO. Thereby, the majority charge carrier of the reduced GO was switched to holes, and p-n junction was produced at the interface instead of Schottky contact. The performance of the hybridized composite sensor was comparatively evaluated with the same reducing gases. Understandably, the gas sensing behavior of the hybridized sensor was converted from n-type to p-type, which confirms that the dominant sensing material of the composite is GO and TiO$_2$ acts as a catalyst. Although slight reduction of gas response in the UV-treated sensor was observed due to the changed amount of the oxygen functional groups in GO via photolysis of TiO$_2$, the function to identify target gas was maintained over a one-month period, showing strong resistance to humidity. The emphasis places on more specific elaboration of each materials' role in sensing mechanism by tailoring charge transfer under the same hybrid structure to provide a framework for effective design of new hybrids and ultimately advance their sensing performances.

122

Chapter 9. Summary and Future Works

9.1. Summary of research

High performance gas sensors integrated on wearable substrates were investigated with two-dimensional nanomaterials. To fabricate sensing devices on textiles, various flexible and wearable substrates were examined, along with the exploration of several low-temperature and non-corrosive fabrication processes. Electrodes were silk-printed onto bare nylon, polyester, and cotton fabrics. After constructing electrodes on fabrics, sensing materials were coated using a facile solution process. Two different solvents, water and ethanol, were compared as typical mediums to disperse graphene oxide (GO). Water dispersed GO solutions were uniformly drop-casted onto the fabrics, whereas ethanol dispersed GO solutions were rapidly absorbed into the weave gap, showing agglomeration. After drying the coated GO solutions, the morphologies of the dried GO films were investigated by comparing surface roughness. The gas sensing response of the GO on three types of fabrics, nylon, polyester, and cotton, was compared using ammonia at room temperature. Enhanced adhesion between sensing film and hydrophilic fabric was obtained by modifying wettability of solution where surface tension of solution and capillary force of fabric were balanced, resulting in uniformly stacked structure and high resistance of bending. The gas response result demonstrated the potential approach for wearable electronic sensors.

Room temperature (RT) gas detection was demonstrated by two-dimensional (2D) nanomaterials using two representative 2D nanomaterials, graphene oxide (GO) and molybdenum disulfide (MoS_2). Commercially available GO and monolayer MoS_2 were drop-casted on flexible

polyimide film, and their morphology and surface condition were studied. Using the prepared sensors, gas detection was successful at room temperature towards various reducing gases. At RT, the GO sensor detected ammonia and methane with n-type behavior, while the MoS_2 sensor sensed ethanol, methanol, acetone, ammonia, and methane with p-type behavior. Based on their sensing performance, the sensing mechanism of each material was studied. In GO sensing, oxygen functional groups, such as hydroxyl, on the surface of GO play an important role to absorb and interact with the analyte. On the other hand, a charge transfer mechanism is the main sensing mechanism in the case of $MoS_2,$ rather surface bonding. Due to its surface groups, overall gas response of GO was higher than that of MoS_2 at the expense of incomplete recovery. Therefore, the surface chemistry of 2D nanomaterials is critical for gas sensing at RT and investigation of surface condition is worthwhile to enhance sensing performance.

Newly emerged 2D MXenes were introduced as promising room-temperature sensing materials, due in part to their intriguing surface chemistry. Titanium carbide ($Ti_3C_2T_x$) was the first discovered and is the most well-investigated material of the MXenes; however, sensing properties of $Ti_3C_2T_x$ have not been investigated. The capability of $Ti_3C_2T_x$ to sense an array of VOC gases at room temperature was demonstrated. The synthesized $Ti_3C_2T_x$ nanosheets were integrated on flexible polyimide films with a facile solution casting method, and their surface chemistry was investigated to study surface reactions. The $Ti_3C_2T_x$ sensor detected all the tested VOC gases such as ethanol, methanol, acetone, and ammonia at room temperature and showed a p-type sensing behavior. The highest sensing response of the $Ti_3C_2T_x$ was obtained with the ammonia analyte, due to its large absorption energy. The possible sensing mechanism of this sensor was also proposed in terms of the majority charge carrier transfer through the interaction between sensing species and the sensing material. This novel $Ti_3C_2T_x$ gas sensor will be the first

124

in a new generation of versatile sensors for futuristic wearable electronics with comparable performance to other 2D material sensors.

Another MXene material investigated along with $Ti_3C_2T_x$ is vanadium carbide (V_2CT_x). Similar to $Ti_3C_2T_x$, V_2CT_X was terminated by chemically active oxygen (O), hydroxyl (OH), and fluorine (F) on the surface in a random distribution. 2D V_2CT_x gas sensors showed outstanding gas sensing performance and ultrahigh sensitivity toward non-polar gases at RT. The fabricated 2D V_2CT_x gas sensors were able to detect trace amounts of various gases including non-polar gases such as hydrogen and methane. The theoretical LoD for hydrogen was 1 ppm and that of methane was 9 ppm at RT, which is among the lowest of the reported values for all 2D materials and vanadium-based metal oxides prepared without any treatment. It is assumed that the excellent gas sensing performance of the 2D V_2CT_X device is related to the surface oxygen functional groups present on the surface of V_2CT_X nanoflakes. Compared to sensors fabricated using $Ti_3C_2T_x$ MXene, the overall gas sensing response of V_2CT_x MXene was slightly better toward the four tested VOC gases: ethanol, methanol, acetone, and ammonia. This may be related to the difference in binding strength of the gases on the functionated V and Ti atom layers on the surface of these MXenes. In addition, the selectivity of the two different carbides is quite different. Ti_3C_2T shows a high response to ammonia, while V_2CT_x showed more selectivity toward hydrogen. Since the two MXenes have similar surface terminations, the higher selectivity of the V_2CT_x device toward hydrogen is likely related to its surface transition metal (V atoms). Through the introduction of two different MXenes to sensing applications, huge potential of MXenes as a sensing material was strongly suggested considering such constituents, structure and surface functionality, which opens new direction to consider enhancing sensing properties.

Previous results have demonstrated the promising potential of 2D nanomaterials for gas sensor applications, but typical 2D materials operating at RT show major drawbacks of the sluggish or irreversible recovery and lack of long-term stability, which should be further refined. As an alternative approach to improve sensing performance for an array, the integration of 2D materials with metal oxides can be considered for multiple benefits. This combination may solve several challenges including sensitivity, selectivity, and stability with the synergistic benefits of hybridization including geometrical effects, electronic effects, and chemical effects. The room temperature gas sensing performance of the GO/TiO_2 composite on flexible polymeric film was enhanced by the effect of photocatalysis of TiO_2 under UV. By incorporating TiO_2 to GO, the surface condition of GO was tailored, and Schottky barriers were created at the interface. As a result, detection of various reducing gases was enabled with an aid of TiO_2 nanoparticles, and the recovery time was quite reduced compared to pure GO film. However, the long-term stability remained as an unsolved problem due to GO's susceptibility to humidity. To solve the stability issue of the sensor, the GO/TiO_2 composite solution was UV treated, and the surface and hetero-junction of the composite were modulated. Due to photocatalytic effect of TiO_2 under UV irradiation, GO became phot-reduced and a p-n junction was produced at the interface instead of Schottky contact. The performance of the hybridized composite sensor was comparatively evaluated using the same reducing gases. Understandably, the gas sensing behavior of the hybridized sensor was converted from n-type to p-type, which confirms that the dominant sensing material of the composite is GO and TiO_2 acts as a catalyst. Although a slight reduction of gas response in the UV-treated sensor was observed due to the changed amount of the oxygen functional groups on GO via photolysis of TiO_2, the ability to identify target gas was maintained for over a one-month period, showing strong resistance to humidity. This result suggests great

126

potential of a GO/TiO$_2$ composite sensor with the photocatalytic effect for multiple gas detection at RT, as well as long-term stability.

9.2. Future works

There are tremendous opportunities to investigate 2D nanomaterials and their boundless combinations with metal oxides for sensor applications. Going forward, new materials, and their hybrids, with innovative designs will be a promising option. Compared to graphene-based gas sensors, little attention has been paid to 2D TMD/MXenes sensors. In addition, the functionalization of TMDs/MXenes though metal oxide hybridizations is still at an early stage of research. In the case of some TMDs such as MoSe$_2$ and MoTe$_2$ or MXenes for sensor applications, no results have been published on their possible metal oxide hybrids. In this regard, simulation results could guide the insight for a heterostructure design prior to an experimental investigation. In addition, an investigation on surface treatment can elucidate the sensing mechanisms and garnish sensing performance for further advancement. Previous studies have examined the surface treatment of 2D nanomaterials, using techniques such as UV treatment or thermal annealing. By introducing photoreactive materials into the heterostructure, the performances on gas response and the response/recovery time can be improved in addition to gaining knowledge on photoinduced charger transfer. For instance, it has been reported that the perovskite crystal structure shows great photo reactivity. By decorating perovskite structured metal oxides on 2D nanomaterials, photoactivated effects can be magnified, resulting in boosted performance.

Bibliography

1.   Neethirajan, S.; Jayas, D.; Sadistap, S., Carbon Dioxide (CO_2) Sensors for the Agri-Food Industry—a Review. *Food and Bioprocess Technology* **2009,** *2*, 115-121.

2.   Fine, G. F.; Cavanagh, L. M.; Afonja, A.; Binions, R., Metal Oxide Semi-Conductor Gas Sensors in Environmental Monitoring. *Sensors* **2010,** *10*, 5469-5502.

3.   Han, Y.; Xu, Z.; Gao, C., Ultrathin Graphene Nanofiltration Membrane for Water Purification. *Advanced Functional Materials* **2013,** *23*, 3693-3700.

4.   Liu, X.; Cheng, S.; Liu, H.; Hu, S.; Zhang, D.; Ning, H., A Survey on Gas Sensing Technology. *Sensors* **2012,** *12*, 9635-9665.

5.   Neri, G., First Fifty Years of Chemoresistive Gas Sensors. *Chemosensors* **2015,** *3*, 1-20.

6.   Yun, Y. J.; Hong, W. G.; Choi, N.-J.; Kim, B. H.; Jun, Y.; Lee, H.-K., Ultrasensitive and Highly Selective Graphene-Based Single Yarn for Use in Wearable Gas Sensor. *Scientific reports* **2015,** *5*, 10904.

7.   Lee, E.; VahidMohammadi, A.; Prorok, B. C.; Yoon, Y. S.; Beidaghi, M.; Kim, D.-J., Room Temperature Gas Sensing of Two-Dimensional Titanium Carbide (Mxene). *ACS applied materials & interfaces* **2017,** *9*, 37184-37190.

8.   Bandodkar, A. J.; Jeerapan, I.; Wang, J., Wearable Chemical Sensors: Present Challenges and Future Prospects. *ACS Sensors* **2016,** *1*, 464-482.

9.   Castano, L. M.; Flatau, A. B., Smart Fabric Sensors and E-Textile Technologies: A Review. *Smart Materials and Structures* **2014,** *23*, 053001.

10.   Righettoni, M.; Amann, A.; Pratsinis, S. E., Breath Analysis by Nanostructured Metal Oxides as Chemo-Resistive Gas Sensors. *Materials Today* **2015,** *18*, 163-171.

11.   Park, H.; Tong, F.; Sujan, A.; Chung, Y.; Park, M.; Tatarchuk, B. J.; Koo, H.; Ahn, H.; Yoon, Y. S.; Kim, D.-J., Growth of Nanostructured ZnO on Wearable Fabrics for Functional Garment. *Materials Letters* **2014,** *118*, 47-50.

12.   Ghosh, R.; Singh, A.; Santra, S.; Ray, S. K.; Chandra, A.; Guha, P. K., Highly Sensitive Large-Area Multi-Layered Graphene-Based Flexible Ammonia Sensor. *Sensors and Actuators B: Chemical* **2014,** *205*, 67-73.

13.   Yang, G.; Lee, C.; Kim, J.; Ren, F.; Pearton, S. J., Flexible Graphene-Based Chemical Sensors on Paper Substrates. *Physical Chemistry Chemical Physics* **2013,** *15*, 1798-1801.

14.   Ammu, S.; Dua, V.; Agnihotra, S. R.; Surwade, S. P.; Phulgirkar, A.; Patel, S.; Manohar, S. K., Flexible, All-Organic Chemiresistor for Detecting Chemically Aggressive Vapors. *Journal of the American Chemical Society* **2012,** *134*, 4553-4556.

15.   Guo, Y.; Wu, B.; Liu, H.; Ma, Y.; Yang, Y.; Zheng, J.; Yu, G.; Liu, Y., Electrical Assembly and Reduction of Graphene Oxide in a Single Solution Step for Use in Flexible Sensors. *Advanced Materials* **2011,** *23*, 4626-4630.

16.   Su, P.-G.; Shieh, H.-C., Flexible NO_2 Sensors Fabricated by Layer-by-Layer Covalent Anchoring and in Situ Reduction of Graphene Oxide. *Sensors and Actuators B: Chemical* **2014,** *190*, 865-872.

17.   Choi, S.-J.; Kim, S.-J.; Kim, I.-D., Ultrafast Optical Reduction of Graphene Oxide Sheets on Colorless Polyimide Film for Wearable Chemical Sensors. *NPG Asia Materials* **2016,** *8*, e315.

18. Claramunt, S.; Monereo, O.; Boix, M.; Leghrib, R.; Prades, J.; Cornet, A.; Merino, P.; Merino, C.; Cirera, A., Flexible Gas Sensor Array with an Embedded Heater Based on Metal Decorated Carbon Nanofibres. *Sensors and Actuators B: Chemical* **2013,** *187*, 401-406.

19. Kim, H.; Kim, Y.; Kim, B.; Yoo, H.-J. In *A Wearable Fabric Computer by Planar-Fashionable Circuit Board Technique*, Wearable and Implantable Body Sensor Networks, 2009. BSN 2009. Sixth International Workshop on, IEEE: **2009**; pp 282-285.

20. Chuang, M. C.; Windmiller, J. R.; Santhosh, P.; Ramírez, G. V.; Galik, M.; Chou, T. Y.; Wang, J., Textile-Based Electrochemical Sensing: Effect of Fabric Substrate and Detection of Nitroaromatic Explosives. *Electroanalysis* **2010,** *22*, 2511-2518.

21. Paul, G.; Torah, R.; Beeby, S.; Tudor, J., The Development of Screen Printed Conductive Networks on Textiles for Biopotential Monitoring Applications. *Sensors and Actuators A: Physical* **2014,** *206*, 35-41.

22. Yang, K.; Freeman, C.; Torah, R.; Beeby, S.; Tudor, J., Screen Printed Fabric Electrode Array for Wearable Functional Electrical Stimulation. *Sensors and Actuators A: Physical* **2014,** *213*, 108-115.

23. Matsuhisa, N.; Kaltenbrunner, M.; Yokota, T.; Jinno, H.; Kuribara, K.; Sekitani, T.; Someya, T., Printable Elastic Conductors with a High Conductivity for Electronic Textile Applications. *Nature communications* **2015,** *6*.

24. Yun, Y. J.; Hong, W. G.; Choi, N.-J.; Kim, B. H.; Jun, Y.; Lee, H.-K., Ultrasensitive and Highly Selective Graphene-Based Single Yarn for Use in Wearable Gas Sensor. *Scientific reports* **2015,** *5*.

25.   Yun, Y. J.; Hong, W. G.; Kim, D. Y.; Kim, H. J.; Jun, Y.; Lee, H.-K., E-Textile Gas Sensors Composed of Molybdenum Disulfide and Reduced Graphene Oxide for High Response and Reliability. *Sensors and Actuators B: Chemical* **2017,** *248*, 829-835.

26.   Kim, H.-J.; Lee, J.-H., Highly Sensitive and Selective Gas Sensors Using P-Type Oxide Semiconductors: Overview. *Sensors Actuators B: Chem.* **2014,** *192*, 607-627.

27.   Choopun, S.; Hongsith, N.; Wongrat, E., Metal-Oxide Nanowires for Gas Sensors. In *Nanowires-Recent Advances*, InTech: **2012**.

28.   Wang, C.; Yin, L.; Zhang, L.; Xiang, D.; Gao, R., Metal Oxide Gas Sensors: Sensitivity and Influencing Factors. *Sensors* **2010,** *10*, 2088-2106.

29.   Miller, D. R.; Akbar, S. A.; Morris, P. A., Nanoscale Metal Oxide-Based Heterojunctions for Gas Sensing: A Review. *Sensors and Actuators B: Chemical* **2014,** *204*, 250-272.

30.   Yang, W.; Gan, L.; Li, H.; Zhai, T., Two-Dimensional Layered Nanomaterials for Gas-Sensing Applications. *Inorganic Chemistry Frontiers* **2016,** *3*, 433-451.

31.   Zhang, X.; Hou, L.; Ciesielski, A.; Samorì, P., 2D Materials Beyond Graphene for High-Performance Energy Storage Applications. *Advanced Energy Materials* **2016,** *6*, 1600671.

32.   Shao, Y.; Wang, J.; Wu, H.; Liu, J.; Aksay, I. A.; Lin, Y., Graphene Based Electrochemical Sensors and Biosensors: A Review. *Electroanalysis* **2010,** *22*, 1027-1036.

33.   Liu, X.; Ma, T.; Pinna, N.; Zhang, J., Two-Dimensional Nanostructured Materials for Gas Sensing. *Advanced Functional Materials* **2017,** *27*, 1702168.

34.   Garcia, J. C.; de Lima, D. B.; Assali, L. V.; Justo, J. F., Group Iv Graphene-and Graphane-Like Nanosheets. *The Journal of Physical Chemistry C* **2011,** *115*, 13242-13246.

35.   Barzegar, M.; Tudu, B., Two-Dimensional Materials for Gas Sensors: From First Discovery to Future Possibilities. *Surface Innovations* **2018,** *6*, 205-230.

36.   Tricoli, A.; Nasiri, N.; De, S., Wearable and Miniaturized Sensor Technologies for Personalized and Preventive Medicine. *Advanced Functional Materials* **2017,** *27*, 1605271.

37.   Ko, G.; Kim, H.-Y.; Ahn, J.; Park, Y.-M.; Lee, K.-Y.; Kim, J., Graphene-Based Nitrogen Dioxide Gas Sensors. *Current Applied Physics* **2010,** *10*, 1002-1004.

38.   Nomani, M. W.; Shishir, R.; Qazi, M.; Diwan, D.; Shields, V.; Spencer, M.; Tompa, G. S.; Sbrockey, N. M.; Koley, G., Highly Sensitive and Selective Detection of NO_2 Using Epitaxial Graphene on 6H-SiC. *Sensors and Actuators B: Chemical* **2010,** *150*, 301-307.

39.   Kumar, S.; Kaushik, S.; Pratap, R.; Raghavan, S., Graphene on Paper: A Simple, Low-Cost Chemical Sensing Platform. *ACS applied materials & interfaces* **2015,** *7*, 2189-2194.

40.   Dua, V.; Surwade, S. P.; Ammu, S.; Agnihotra, S. R.; Jain, S.; Roberts, K. E.; Park, S.; Ruoff, R. S.; Manohar, S. K., All-Organic Vapor Sensor Using Inkjet-Printed Reduced Graphene Oxide. *Angewandte Chemie International Edition* **2010,** *49*, 2154-2157.

41.   Ghosh, R.; Midya, A.; Santra, S.; Ray, S. K.; Guha, P. K., Chemically Reduced Graphene Oxide for Ammonia Detection at Room Temperature. *ACS applied materials & interfaces* **2013,** *5*, 7599-7603.

42.   Hu, N.; Yang, Z.; Wang, Y.; Zhang, L.; Wang, Y.; Huang, X.; Wei, H.; Wei, L.; Zhang, Y., Ultrafast and Sensitive Room Temperature NH_3 Gas Sensors Based on Chemically Reduced Graphene Oxide. *Nanotechnology* **2013,** *25*, 025502.

43.   Choi, Y. R.; Yoon, Y.-G.; Choi, K. S.; Kang, J. H.; Shim, Y.-S.; Kim, Y. H.; Chang, H. J.; Lee, J.-H.; Park, C. R.; Kim, S. Y., Role of Oxygen Functional Groups in Graphene Oxide for Reversible Room-Temperature NO_2 Sensing. *Carbon* **2015,** *91*, 178-187.

44.   Park, H.; Ahn, H.; Chung, Y.; Cho, S. B.; Yoon, Y. S.; Kim, D.-J., Transition of Gas Sensing Behavior in Non-Reduced Graphene Oxides with Thermal Annealing. *Materials Letters* **2014,** *136*, 164-167.

45.   Lee, K.; Gatensby, R.; McEvoy, N.; Hallam, T.; Duesberg, G. S., High-Performance Sensors Based on Molybdenum Disulfide Thin Films. *Advanced materials* **2013,** *25*, 6699-6702.

46.   Cho, B.; Hahm, M. G.; Choi, M.; Yoon, J.; Kim, A. R.; Lee, Y.-J.; Park, S.-G.; Kwon, J.-D.; Kim, C. S.; Song, M., Charge-Transfer-Based Gas Sensing Using Atomic-Layer MoS_2. *Scientific reports* **2015,** *5*.

47.   Cho, B.; Kim, A. R.; Park, Y.; Yoon, J.; Lee, Y.-J.; Lee, S.; Yoo, T. J.; Kang, C. G.; Lee, B. H.; Ko, H. C., Bifunctional Sensing Characteristics of Chemical Vapor Deposition Synthesized Atomic-Layered MoS_2. *ACS applied materials & interfaces* **2015,** *7*, 2952-2959.

48.   Late, D. J.; Doneux, T.; Bougouma, M., Single-Layer $MoSe_2$ Based NH_3 Gas Sensor. *Applied physics letters* **2014,** *105*, 233103.

49.   O'Brien, M.; Lee, K.; Morrish, R.; Berner, N. C.; McEvoy, N.; Wolden, C. A.; Duesberg, G. S., Plasma Assisted Synthesis of WS_2 for Gas Sensing Applications. *Chemical Physics Letters* **2014,** *615*, 6-10.

50.   Qin, Z.; Zeng, D.; Zhang, J.; Wu, C.; Wen, Y.; Shan, B.; Xie, C., Effect of Layer Number on Recovery Rate of WS_2 Nanosheets for Ammonia Detection at Room Temperature. *Applied Surface Science* **2017,** *414*, 244-250.

51.   Abbas, A. N.; Liu, B.; Chen, L.; Ma, Y.; Cong, S.; Aroonyadet, N.; Köpf, M.; Nilges, T.; Zhou, C., Black Phosphorus Gas Sensors. *ACS nano* **2015,** *9*, 5618-5624.

52.   Cho, S. Y.; Lee, Y.; Koh, H. J.; Jung, H.; Kim, J. S.; Yoo, H. W.; Kim, J.; Jung, H. T., Superior Chemical Sensing Performance of Black Phosphorus: Comparison with MoS$_2$ and Graphene. *Advanced Materials* **2016,** *28*, 7020-7028.

53.   Nasrollahzadeh, M.; Babaei, F.; Fakhri, P.; Jaleh, B., Synthesis, Characterization, Structural, Optical Properties and Catalytic Activity of Reduced Graphene Oxide/Copper Nanocomposites. *Rsc Advances* **2015,** *5*, 10782-10789.

54.   Peng, Y.; Li, J., Ammonia Adsorption on Graphene and Graphene Oxide: A First-Principles Study. *Frontiers of Environmental Science & Engineering* **2013,** *7*, 403-411.

55.   Huang, B.; Li, Z.; Liu, Z.; Zhou, G.; Hao, S.; Wu, J.; Gu, B.-L.; Duan, W., Adsorption of Gas Molecules on Graphene Nanoribbons and Its Implication for Nanoscale Molecule Sensor. *The Journal of Physical Chemistry C* **2008,** *112*, 13442-13446.

56.   Leenaerts, O.; Partoens, B.; Peeters, F., Adsorption of H$_2$O, NH$_3$, CO, NO$_2$, and NO on Graphene: A First-Principles Study. *Physical Review B* **2008,** *77*, 125416.

57.   Radisavljevic, B.; Radenovic, A.; Brivio, J.; Giacometti, i. V.; Kis, A., Single-Layer MoS$_2$ Transistors. *Nature nanotechnology* **2011,** *6*, 147-150.

58.   Kim, T. H.; Kim, Y. H.; Park, S. Y.; Kim, S. Y.; Jang, H. W., Two-Dimensional Transition Metal Disulfides for Chemoresistive Gas Sensing: Perspective and Challenges. *Chemosensors* **2017,** *5*, 15.

59.   Andoshe, D. M.; Jeon, J.-M.; Kim, S. Y.; Jang, H. W., Two-Dimensional Transition Metal Dichalcogenide Nanomaterials for Solar Water Splitting. *Electronic Materials Letters* **2015,** *11*, 323-335.

60.   Das, S.; Chen, H.-Y.; Penumatcha, A. V.; Appenzeller, J., High Performance Multilayer MoS$_2$ Transistors with Scandium Contacts. *Nano letters* **2012,** *13*, 100-105.

61.   Castellanos-Gomez, A.; Poot, M.; Steele, G. A.; van der Zant, H. S.; Agraït, N.; Rubio-Bollinger, G., Elastic Properties of Freely Suspended MoS$_2$ Nanosheets. *Advanced Materials* **2012,** *24*, 772-775.

62.   Ganatra, R.; Zhang, Q., Few-Layer MoS$_2$: A Promising Layered Semiconductor. *ACS nano* **2014,** *8*, 4074-4099.

63.   Cho, B.; Hahm, M. G.; Choi, M.; Yoon, J.; Kim, A. R.; Lee, Y.-J.; Park, S.-G.; Kwon, J.-D.; Kim, C. S.; Song, M., Charge-Transfer-Based Gas Sensing Using Atomic-Layer MoS$_2$. *Scientific reports* **2015,** *5*, 8052.

64.   Yue, Q.; Shao, Z.; Chang, S.; Li, J., Adsorption of Gas Molecules on Monolayer MoS$_2$ and Effect of Applied Electric Field. *Nanoscale research letters* **2013,** *8*, 425-431.

65.   Ivanovskii, A. L.; Enyashin, A. N., Graphene-Like Transition-Metal Nanocarbides and Nanonitrides. *Russian Chemical Reviews* **2013,** *82*, 735.

66.   Anasori, B.; Lukatskaya, M. R.; Gogotsi, Y., 2D Metal Carbides and Nitrides (Mxenes) for Energy Storage. *Nature Reviews Materials* **2017,** *2*, 16098.

67.   Anasori, B.; Xie, Y.; Beidaghi, M.; Lu, J.; Hosler, B. C.; Hultman, L.; Kent, P. R.; Gogotsi, Y.; Barsoum, M. W., Two-Dimensional, Ordered, Double Transition Metals Carbides (Mxenes). *ACS nano* **2015,** *9*, 9507-9516.

68.   Naguib, M.; Mashtalir, O.; Carle, J.; Presser, V.; Lu, J.; Hultman, L.; Gogotsi, Y.; Barsoum, M. W., Two-Dimensional Transition Metal Carbides. *ACS nano* **2012,** *6*, 1322-1331.

69.   Naguib, M.; Mochalin, V. N.; Barsoum, M. W.; Gogotsi, Y., 25th Anniversary Article: Mxenes: A New Family of Two-Dimensional Materials. *Advanced Materials* **2014,** *26*, 992-1005.

70.   Mashtalir, O.; Naguib, M.; Mochalin, V. N.; Dall'Agnese, Y.; Heon, M.; Barsoum, M. W.; Gogotsi, Y., Intercalation and Delamination of Layered Carbides and Carbonitrides. *Nature communications* **2013,** *4*, 1716.

71.   Ghidiu, M.; Lukatskaya, M. R.; Zhao, M.-Q.; Gogotsi, Y.; Barsoum, M. W., Conductive Two-Dimensional Titanium Carbide Clay with High Volumetric Capacitance. *Nature* **2014,** *516*, 78-81.

72.   Xie, Y.; Naguib, M.; Mochalin, V. N.; Barsoum, M. W.; Gogotsi, Y.; Yu, X.; Nam, K.-W.; Yang, X.-Q.; Kolesnikov, A. I.; Kent, P. R., Role of Surface Structure on Li-Ion Energy Storage Capacity of Two-Dimensional Transition-Metal Carbides. *Journal of the American Chemical Society* **2014,** *136*, 6385-6394.

73.   Halim, J.; Cook, K. M.; Naguib, M.; Eklund, P.; Gogotsi, Y.; Rosen, J.; Barsoum, M. W., X-Ray Photoelectron Spectroscopy of Select Multi-Layered Transition Metal Carbides (Mxenes). *Applied Surface Science* **2016,** *362*, 406-417.

74.   Hope, M. A.; Forse, A. C.; Griffith, K. J.; Lukatskaya, M. R.; Ghidiu, M.; Gogotsi, Y.; Grey, C. P., Nmr Reveals the Surface Functionalisation of Ti_3C_2 Mxene. *Physical Chemistry Chemical Physics* **2016,** *18*, 5099-5102.

75.   Yu, X.-f.; Li, Y.-c.; Cheng, J.-b.; Liu, Z.-b.; Li, Q.-z.; Li, W.-z.; Yang, X.; Xiao, B., Monolayer Ti_2CO_2: A Promising Candidate for NH_3 Sensor or Capturer with High Sensitivity and Selectivity. *ACS applied materials & interfaces* **2015,** *7*, 13707-13713.

76.   Xiao, B.; Li, Y.-c.; Yu, X.-f.; Cheng, J.-b., Mxenes: Reusable Materials for NH_3 Sensor or Capturer by Controlling the Charge Injection. *Sensors and Actuators B: Chemical* **2016,** *235*, 103-109.

77.   Ma, S.-h.; Yuan, D.; Jiao, Z.-Y.; Wang, T.-X.; Dai, X., Monolayer SC_2CO_2: A Promising Candidate as SO_2 Gas Sensor or Capturer. *The Journal of Physical Chemistry C* **2017**.

78.   VahidMohammadi, A.; Hadjikhani, A.; Shahbazmohamadi, S.; Beidaghi, M., Two-Dimensional Vanadium Carbide (Mxene) as a High-Capacity Cathode Material for Rechargeable Aluminum Batteries. *ACS nano* **2017**, *11*, 11135-11144.

79.   Lai, S.; Jeon, J.; Jang, S. K.; Xu, J.; Choi, Y. J.; Park, J.-H.; Hwang, E.; Lee, S., Surface Group Modification and Carrier Transport Properties of Layered Transition Metal Carbides (Ti_2CT_x, T:–OH,–F and–O). *Nanoscale* **2015,** *7*, 19390-19396.

80.   Zhang, Y.; Wang, L.; Zhang, N.; Zhou, Z., Adsorptive Environmental Applications of Mxene Nanomaterials: A Review. *RSC Advances* **2018,** *8*, 19895-19905.

81.   Zhang, Y.-J.; Zhou, Z.-J.; Lan, J.-H.; Ge, C.-C.; Chai, Z.-F.; Zhang, P.; Shi, W.-Q., Theoretical Insights into the Uranyl Adsorption Behavior on Vanadium Carbide Mxene. *Applied Surface Science* **2017,** *426*, 572-578.

82.   Chen, J.; Chen, K.; Tong, D.; Huang, Y.; Zhang, J.; Xue, J.; Huang, Q.; Chen, T., CO_2 and Temperature Dual Responsive "Smart" Mxene Phases. *Chemical Communications* **2015,** *51*, 314-317.

83.   Yang, C.; Xiao, F.; Wang, J.; Su, X., 3D Flower-and 2D Sheet-Like Cuo Nanostructures: Microwave-Assisted Synthesis and Application in Gas Sensors. *Sensors and Actuators B: Chemical* **2015,** *207*, 177-185.

84.   Hao, J.; Zhang, D.; Sun, Q.; Zheng, S.; Sun, J.; Wang, Y., Hierarchical SnS_2/SnO_2 Nanoheterojunctions with Increased Active-Sites and Charge Transfer for Ultrasensitive NO_2 Detection. *Nanoscale* **2018,** *10*, 7210-7217.

85.   Gu, F.; Nie, R.; Han, D.; Wang, Z., In2o3–Graphene Nanocomposite Based Gas Sensor for Selective Detection of NO$_2$ at Room Temperature. *Sensors and Actuators B: Chemical* **2015,** *219*, 94-99.

86.   Meng, F.-L.; Guo, Z.; Huang, X.-J., Graphene-Based Hybrids for Chemiresistive Gas Sensors. *TrAC, Trends Anal. Chem.* **2015,** *68*, 37-47.

87.   Yamazoe, N., New Approaches for Improving Semiconductor Gas Sensors. *Sensors and Actuators B: Chemical* **1991,** *5*, 7-19.

88.   Park, W.; Park, J.; Jang, J.; Lee, H.; Jeong, H.; Cho, K.; Hong, S.; Lee, T., Oxygen Environmental and Passivation Effects on Molybdenum Disulfide Field Effect Transistors. *Nanotechnology* **2013,** *24*, 095202.

89.   Qiu, H.; Pan, L.; Yao, Z.; Li, J.; Shi, Y.; Wang, X., Electrical Characterization of Back-Gated Bi-Layer MoS$_2$ Field-Effect Transistors and the Effect of Ambient on Their Performances. *Applied Physics Letters* **2012,** *100*, 123104.

90.   Varghese, S. S.; Lonkar, S.; Singh, K.; Swaminathan, S.; Abdala, A., Recent Advances in Graphene Based Gas Sensors. *Sensors and Actuators B: Chemical* **2015,** *218*, 160-183.

91.   Chatterjee, S. G.; Chatterjee, S.; Ray, A. K.; Chakraborty, A. K., Graphene–Metal Oxide Nanohybrids for Toxic Gas Sensor: A Review. *Sensors and Actuators B: Chemical* **2015,** *221*, 1170-1181.

92.   Lin, Q.; Li, Y.; Yang, M., Tin Oxide/Graphene Composite Fabricated Via a Hydrothermal Method for Gas Sensors Working at Room Temperature. *Sensors and actuators B: chemical* **2012,** *173*, 139-147.

93.   Zhang, H.; Feng, J.; Fei, T.; Liu, S.; Zhang, T., SnO_2 Nanoparticles-Reduced Graphene Oxide Nanocomposites for NO_2 Sensing at Low Operating Temperature. *Sensors and Actuators B: Chemical* **2014,** *190*, 472-478.

94.   Zhang, D.; Liu, A.; Chang, H.; Xia, B., Room-Temperature High-Performance Acetone Gas Sensor Based on Hydrothermal Synthesized SnO_2-Reduced Graphene Oxide Hybrid Composite. *RSC Advances* **2015,** *5*, 3016-3022.

95.   Anand, K.; Singh, O.; Singh, M. P.; Kaur, J.; Singh, R. C., Hydrogen Sensor Based on Graphene/ZnO Nanocomposite. *Sensors and Actuators B: Chemical* **2014,** *195*, 409-415.

96.   Liu, S.; Yu, B.; Zhang, H.; Fei, T.; Zhang, T., Enhancing NO_2 Gas Sensing Performances at Room Temperature Based on Reduced Graphene Oxide-Zno Nanoparticles Hybrids. *Sensors and Actuators B: Chemical* **2014,** *202*, 272-278.

97.   Li, X.; Zhao, Y.; Wang, X.; Wang, J.; Gaskov, A. M.; Akbar, S., Reduced Graphene Oxide (RGO) Decorated TiO_2 Microspheres for Selective Room-Temperature Gas Sensors. *Sensors Actuators B: Chem.* **2016,** *230*, 330-336.

98.   Ye, Z.; Tai, H.; Xie, T.; Yuan, Z.; Liu, C.; Jiang, Y., Room Temperature Formaldehyde Sensor with Enhanced Performance Based on Reduced Graphene Oxide/Titanium Dioxide. *Sensors and Actuators B: Chemical* **2016,** *223*, 149-156.

99.   Srivastava, S.; Jain, K.; Singh, V.; Singh, S.; Vijayan, N.; Dilawar, N.; Gupta, G.; Senguttuvan, T., Faster Response of NO_2 Sensing in Graphene–WO_3 Nanocomposites. *Nanotechnology* **2012,** *23*, 205501.

100.   Chen, N.; Li, X.; Wang, X.; Yu, J.; Wang, J.; Tang, Z.; Akbar, S., Enhanced Room Temperature Sensing of Co_3O_4-Intercalated Reduced Graphene Oxide Based Gas Sensors. *Sensors and Actuators B: Chemical* **2013,** *188*, 902-908.

101. Liang, S.; Zhu, J.; Wang, C.; Yu, S.; Bi, H.; Liu, X.; Wang, X., Fabrication of a Fe_2O_3@ Graphene Nanostructures for Enhanced Gas-Sensing Property to Ethanol. *Applied Surface Science* **2014,** *292*, 278-284.

102. Naguib, M.; Unocic, R. R.; Armstrong, B. L.; Nanda, J., Large-Scale Delamination of Multi-Layers Transition Metal Carbides and Carbonitrides "Mxenes". *Dalton transactions* **2015,** *44*, 9353-9358.

103. Marikutsa, A. V.; Rumyantseva, M. N.; Yashina, L. V.; Gaskov, A. M., Role of Surface Hydroxyl Groups in Promoting Room Temperature CO Sensing by Pd-Modified Nanocrystalline SnO_2. *Journal of Solid State Chemistry* **2010,** *183*, 2389-2399.

104. Ying, G.; Kota, S.; Dillon, A. D.; Fafarman, A. T.; Barsoum, M. W., Conductive Transparent V_2CT_x (Mxene) Films. *FlatChem* **2018,** *8*, 25-30.

105. LibreTexts Functional Groups and Classes of Organic Compounds. https://chem.libretexts.org/Textbook_Maps/General_Chemistry/Map%3A_Chemistry_(Averill_and_Eldredge)/24%3A_Organic_Compounds/24.1%3A_Functional_Groups_and_Classes_of_Organic_Compounds.

106. Lorwongtragool, P.; Sowade, E.; Watthanawisuth, N.; Baumann, R. R.; Kerdcharoen, T., A Novel Wearable Electronic Nose for Healthcare Based on Flexible Printed Chemical Sensor Array. *Sensors* **2014,** *14*, 19700-19712.

107. Ahn, H.; Park, J.-H.; Kim, S.-B.; Jee, S. H.; Yoon, Y. S.; Kim, D.-J., Vertically Aligned ZnO Nanorod Sensor on Flexible Substrate for Ethanol Gas Monitoring. *Electrochemical and Solid-State Letters* **2010,** *13*, J125-J128.

108. Windmiller, J. R.; Wang, J., Wearable Electrochemical Sensors and Biosensors: A Review. *Electroanalysis* **2013,** *25*, 29-46.

109.   Vazquez, G.; Alvarez, E.; Navaza, J. M., Surface Tension of Alcohol Water from 20 to 50. Degree. C. *Journal of chemical and engineering data* **1995,** *40*, 611-614.

110.   Zhang, X.; Wan, S.; Pu, J.; Wang, L.; Liu, X., Highly Hydrophobic and Adhesive Performance of Graphene Films. *Journal of Materials Chemistry* **2011,** *21*, 12251-12258.

111.   Zhang, J.; Zhang, R.; Wang, X.; Feng, W.; Hu, P.; O'Neill, W.; Wang, Z., Fabrication of Highly Oriented Reduced Graphene Oxide Microbelts Array for Massive Production of Sensitive Ammonia Gas Sensors. *Journal of Micromechanics and Microengineering* **2013,** *23*, 095031.

112.   Wu, J.; Becerril, H. A.; Bao, Z.; Liu, Z.; Chen, Y.; Peumans, P., Organic Solar Cells with Solution-Processed Graphene Transparent Electrodes. *Applied Physics Letters* **2008,** *92*, 263302.

113.   Lam, K. C.; Huang, B.; Shi, S.-Q., Room-Temperature Methane Gas Sensing Properties Based on in Situ Reduced Graphene Oxide Incorporated with Tin Dioxide. *Journal of Materials Chemistry A* **2017**.

114.   Pei, S.; Cheng, H.-M., The Reduction of Graphene Oxide. *Carbon* **2012,** *50*, 3210-3228.

115.   Wu, J.; Becerril, H. A.; Bao, Z.; Liu, Z.; Chen, Y.; Peumans, P., Organic Solar Cells with Solution-Processed Graphene Transparent Electrodes. *Applied Physics Letters* **2008,** *92*, 237.

116.   Long, G. L.; Winefordner, J. D., Limit of Detection. A Closer Look at the Iupac Definition. *Analytical Chemistry* **1983,** *55*, 712A-724A.

117.   Biaggi-Labiosa, A.; Solá, F.; Lebrón-Colón, M.; Evans, L.; Xu, J.; Hunter, G.; Berger, G.; Gonzalez, J., A Novel Methane Sensor Based on Porous SnO_2 Nanorods: Room Temperature to High Temperature Detection. *Nanotechnology* **2012,** *23*, 455501.

118.   Wu, Z.; Chen, X.; Zhu, S.; Zhou, Z.; Yao, Y.; Quan, W.; Liu, B., Room Temperature Methane Sensor Based on Graphene Nanosheets/Polyaniline Nanocomposite Thin Film. *IEEE Sensors Journal* **2013,** *13*, 777-782.

119.   Li, W.; Liang, J.; Liu, J.; Zhou, L.; Yang, R.; Hu, M., Synthesis and Room Temperature CH_4 Gas Sensing Properties of Vanadium Dioxide Nanorods. *Materials Letters* **2016,** *173*, 199-202.

120.   Wang, T.; Huang, D.; Yang, Z.; Xu, S.; He, G.; Li, X.; Hu, N.; Yin, G.; He, D.; Zhang, L., A Review on Graphene-Based Gas/Vapor Sensors with Unique Properties and Potential Applications. *Nano-Micro Letters* **2016,** *8*, 95-119.

121.   Lee, E.; Yoon, Y. S.; Kim, D.-J., Two-Dimensional Transition Metal Dichalcogenides and Metal Oxide Hybrids for Gas Sensing. *ACS sensors* **2018**.

122.   Rassi, A.; Dias, J. P.; Marin-Neto, J. A., Challenges and Opportunities for Primary, Secondary, and Tertiary Prevention of Chagas' Disease. *Heart* **2009,** *95*, 524-534.

123.   Jin, H.; Huynh, T.-P.; Haick, H., Self-Healable Sensors Based Nanoparticles for Detecting Physiological Markers Via Skin and Breath: Toward Disease Prevention Via Wearable Devices. *Nano Letters* **2016,** *16*, 4194-4202.

124.   Yamada, Y.; Hiyama, S.; Toyooka, T.; Takeuchi, S.; Itabashi, K.; Okubo, T.; Tabata, H., Ultratrace Measurement of Acetone from Skin Using Zeolite: Toward Development of a Wearable Monitor of Fat Metabolism. *Analytical Chemistry* **2015,** *87*, 7588-7594.

125.   Miekisch, W.; Schubert, J. K.; Noeldge-Schomburg, G. F., Diagnostic Potential of Breath Analysis—Focus on Volatile Organic Compounds. *Clinica Chimica Acta* **2004,** *347*, 25-39.

126.   Di Francesco, F.; Fuoco, R.; Trivella, M. G.; Ceccarini, A., Breath Analysis: Trends in Techniques and Clinical Applications. *Microchemical Journal* **2005,** *79*, 405-410.

127.   Chung, Y.; Park, H.; Lee, E.; Kim, S.-H.; Kim, D.-J., Communication—Gas Sensing Behaviors of Electrophoretically Deposited Nickel Oxide Films from Morphologically Tailored Particles. *Journal of the Electrochemical Society* **2016,** *163*, B624-B626.

128.   Shahzad, F.; Alhabeb, M.; Hatter, C. B.; Anasori, B.; Hong, S. M.; Koo, C. M.; Gogotsi, Y., Electromagnetic Interference Shielding with 2d Transition Metal Carbides (MXenes). *Science* **2016,** *353*, 1137-1140.

129.   Xue, Q.; Zhang, H.; Zhu, M.; Pei, Z.; Li, H.; Wang, Z.; Huang, Y.; Huang, Y.; Deng, Q.; Zhou, J., Photoluminescent Ti_3C_2 Mxene Quantum Dots for Multicolor Cellular Imaging. *Advanced Materials* **2017,** *29*, 1604847.

130.   Xu, S.; Wei, G.; Li, J.; Ji, Y.; Klyui, N.; Izotov, V.; Han, W., Binder-Free $Ti_3C_2T_X$ Mxene Electrode Film for Supercapacitor Produced by Electrophoretic Deposition Method. *Chem. Eng. J.* **2017,** *317*, 1026-1036.

131.   Wang, H.; Zhang, J.; Wu, Y.; Huang, H.; Li, G.; Zhang, X.; Wang, Z., Surface Modified MXene Ti_3C_2 Multilayers by Aryl Diazonium Salts Leading to Large-Scale Delamination. *Applied Surface Science* **2016,** *384*, 287-293.

132.   Lei, J.-C.; Zhang, X.; Zhou, Z., Recent Advances in Mxene: Preparation, Properties, and Applications. *Frontiers of Physics* **2015,** *10*, 276-286.

133.   Xu, B.; Zhu, M.; Zhang, W.; Zhen, X.; Pei, Z.; Xue, Q.; Zhi, C.; Shi, P., Ultrathin MXene-Micropattern-Based Field-Effect Transistor for Probing Neural Activity. *Advanced Materials* **2016,** *28*, 3333–3339.

134.   Tang, Q.; Zhou, Z.; Shen, P., Are Mxenes Promising Anode Materials for Li Ion Batteries? Computational Studies on Electronic Properties and Li Storage Capability of Ti_3C_2 and $Ti_3C_2X_2$ (X= F, OH) Monolayer. *Journal of the American Chemical Society* **2012,** *134*, 16909-16916.

135.   Han, M.; Yin, X.; Wu, H.; Hou, Z.; Song, C.; Li, X.; Zhang, L.; Cheng, L., Ti_3C_2 MXenes with Modified Surface for High-Performance Electromagnetic Absorption and Shielding in the X-Band. *ACS Applied Materials & Interfaces* **2016,** *8*, 21011-21019.

136.   Geistlinger, H., Electron Theory of Thin-Film Gas Sensors. *Sensors and Actuators B: Chemical* **1993,** *17*, 47-60.

137.   Lu, G.; Ocola, L. E.; Chen, J., Reduced Graphene Oxide for Room-Temperature Gas Sensors. *Nanotechnology* **2009,** *20*, 445502.

138.   Kim, K.; Park, H. J.; Woo, B.-C.; Kim, K. J.; Kim, G. T.; Yun, W. S., Electric Property Evolution of Structurally Defected Multilayer Graphene. *Nano Letters* **2008,** *8*, 3092-3096.

139.   Gautam, M.; Jayatissa, A. H., Ammonia Gas Sensing Behavior of Graphene Surface Decorated with Gold Nanoparticles. *Solid-State Electronics* **2012,** *78*, 159-165.

140.   Fenn, L.; Kissel, D., Ammonia Volatilization from Surface Applications of Ammonium Compounds on Calcareous Soils: I. General Theory. *Soil Science Society of America Journal* **1973,** *37*, 855-859.

141.   Choi, S.-J.; Jang, B.-H.; Lee, S.-J.; Min, B. K.; Rothschild, A.; Kim, I.-D., Selective Detection of Acetone and Hydrogen Sulfide for the Diagnosis of Diabetes and Halitosis Using SnO_2 Nanofibers Functionalized with Reduced Graphene Oxide Nanosheets. *ACS Applied Materials & Interfaces* **2014,** *6*, 2588-2597.

142.   Perkins, F. K.; Friedman, A. L.; Cobas, E.; Campbell, P.; Jernigan, G.; Jonker, B. T., Chemical Vapor Sensing with Monolayer MoS_2. *Nano Letters* **2013,** *13*, 668-673.

143.   Zhang, H.; Kulkarni, A.; Kim, H.; Woo, D.; Kim, Y.-J.; Hong, B. H.; Choi, J.-B.; Kim, T., Detection of Acetone Vapor Using Graphene on Polymer Optical Fiber. *Journal of nanoscience and nanotechnology* **2011,** *11*, 5939-5943.

144.   Tung, T. T.; Nine, M. J.; Krebsz, M.; Pasinszki, T.; Coghlan, C. J.; Tran, D. N.; Losic, D., Recent Advances in Sensing Applications of Graphene Assemblies and Their Composites. *Advanced Functional Materials* **2017,** *27*, 1702891.

144

145.   Steele, B. C., Fuel-Cell Technology: Running on Natural Gas. *Nature* **1999,** *400*, 619.

146.   Götz, M.; Lefebvre, J.; Mörs, F.; Koch, A. M.; Graf, F.; Bajohr, S.; Reimert, R.; Kolb, T., Renewable Power-to-Gas: A Technological and Economic Review. *Renewable energy* **2016,** *85*, 1371-1390.

147.   Ley, M. B.; Jepsen, L. H.; Lee, Y.-S.; Cho, Y. W.; Von Colbe, J. M. B.; Dornheim, M.; Rokni, M.; Jensen, J. O.; Sloth, M.; Filinchuk, Y., Complex Hydrides for Hydrogen Storage–New Perspectives. *Materials Today* **2014,** *17*, 122-128.

148.   Cho, E. S.; Ruminski, A. M.; Aloni, S.; Liu, Y.-S.; Guo, J.; Urban, J. J., Graphene Oxide/Metal Nanocrystal Multilaminates as the Atomic Limit for Safe and Selective Hydrogen Storage. *Nature communications* **2016,** *7*, 10804.

149.   Lam, K. C.; Huang, B.; Shi, S.-Q., Room-Temperature Methane Gas Sensing Properties Based on in Situ Reduced Graphene Oxide Incorporated with Tin Dioxide. *Journal of Materials Chemistry A* **2017,** *5*, 11131-11142.

150.   Shiraz, H. G., Efficient Room Temperature Hydrogen Gas Sensing Based on Graphene Oxide and Decorated Porous Silicon. *International Journal of Hydrogen Energy* **2017,** *42*, 15966-15972.

151.   Goltsov, V. A.; Veziroglu, T. N., A Step on the Road to Hydrogen Civilization. *International Journal of Hydrogen Energy* **2002,** *27*, 719-723.

152.   Yu, N.; Wang, L.; Li, M.; Sun, X.; Hou, T.; Li, Y., Molybdenum Disulfide as a Highly Efficient Adsorbent for Non-Polar Gases. *Physical Chemistry Chemical Physics* **2015,** *17*, 11700-11704.

153.   Yang, S.; Jiang, C.; Wei, S.-h., Gas Sensing in 2D Materials. *Applied Physics Reviews* **2017,** *4*, 021304.

154. Choi, W.; Choudhary, N.; Han, G. H.; Park, J.; Akinwande, D.; Lee, Y. H., Recent Development of Two-Dimensional Transition Metal Dichalcogenides and Their Applications. *Materials Today* **2017,** *20*, 116-130.

155. Zhang, Q.; Zhang, J.; Wan, S.; Wang, W.; Fu, L., Stimuli-Responsive 2D Materials Beyond Graphene. *Advanced Functional Materials* **2018**, 1802500.

156. Li, H.; Yin, Z.; He, Q.; Li, H.; Huang, X.; Lu, G.; Fam, D. W. H.; Tok, A. I. Y.; Zhang, Q.; Zhang, H., Fabrication of Single-and Multilayer MoS_2 Film-Based Field-Effect Transistors for Sensing No at Room Temperature. *small* **2012,** *8*, 63-67.

157. Kim, S. J.; Koh, H.-J.; Ren, C. E.; Kwon, O.; Maleski, K.; Cho, S.-Y.; Anasori, B.; Kim, C.-K.; Choi, Y.-K.; Kim, J., Metallic $Ti_3C_2T_X$ Mxene Gas Sensors with Ultrahigh Signal-to-Noise Ratio. *ACS nano* **2018,** *12*, 986-993.

158. Anasori, B.; Lukatskaya, M. R.; Gogotsi, Y., 2D Metal Carbides and Nitrides (MXenes) for Energy Storage. *Nature Reviews Materials* **2017,** *2*, 16098.

159. Lukatskaya, M. R.; Kota, S.; Lin, Z.; Zhao, M.-Q.; Shpigel, N.; Levi, M. D.; Halim, J.; Taberna, P.-L.; Barsoum, M. W.; Simon, P., Ultra-High-Rate Pseudocapacitive Energy Storage in Two-Dimensional Transition Metal Carbides. *Nature Energy* **2017,** *2*, 17105.

160. Xia, Y.; Mathis, T. S.; Zhao, M.-Q.; Anasori, B.; Dang, A.; Zhou, Z.; Cho, H.; Gogotsi, Y.; Yang, S., Thickness-Independent Capacitance of Vertically Aligned Liquid-Crystalline MXenes. *Nature* **2018,** *557*, 409.

161. Boota, M.; Anasori, B.; Voigt, C.; Zhao, M. Q.; Barsoum, M. W.; Gogotsi, Y., Pseudocapacitive Electrodes Produced by Oxidant-Free Polymerization of Pyrrole between the Layers of 2D Titanium Carbide (Mxene). *Advanced Materials* **2016,** *28*, 1517-1522.

162.   VahidMohammadi, A.; Moncada, J.; Chen, H.; Kayali, E.; Orangi, J.; Carrero, C. A.; Beidaghi, M., Thick and Freestanding Mxene/Pani Pseudocapacitive Electrodes with Ultrahigh Specific Capacitance. *Journal of Materials Chemistry A* **2018**.

163.   Ling, Z.; Ren, C. E.; Zhao, M.-Q.; Yang, J.; Giammarco, J. M.; Qiu, J.; Barsoum, M. W.; Gogotsi, Y., Flexible and Conductive Mxene Films and Nanocomposites with High Capacitance. *Proceedings of the National Academy of Sciences* **2014,** *111*, 16676-16681.

164.   Seh, Z. W.; Fredrickson, K. D.; Anasori, B.; Kibsgaard, J.; Strickler, A. L.; Lukatskaya, M. R.; Gogotsi, Y.; Jaramillo, T. F.; Vojvodic, A., Two-Dimensional Molybdenum Carbide (MXene) as an Efficient Electrocatalyst for Hydrogen Evolution. *ACS Energy Letters* **2016,** *1*, 589-594.

165.   Ran, J.; Gao, G.; Li, F.-T.; Ma, T.-Y.; Du, A.; Qiao, S.-Z., Ti_3C_2 MXene Co-Catalyst on Metal Sulfide Photo-Absorbers for Enhanced Visible-Light Photocatalytic Hydrogen Production. *Nature communications* **2017,** *8*, 13907.

166.   Champagne, A.; Shi, L.; Ouisse, T.; Hackens, B.; Charlier, J.-C., Electronic and Vibrational Properties of V_2C-Based Mxenes: From Experiments to First-Principles Modeling. *Physical Review B* **2018,** *97*, 115439.

167.   Naguib, M.; Kurtoglu, M.; Presser, V.; Lu, J.; Niu, J.; Heon, M.; Hultman, L.; Gogotsi, Y.; Barsoum, M. W., Two-Dimensional Nanocrystals Produced by Exfoliation of Ti_3AlC_2. *Advanced Materials* **2011,** *23*, 4248-4253.

168.   Dodds, P. E.; Staffell, I.; Hawkes, A. D.; Li, F.; Grünewald, P.; McDowall, W.; Ekins, P., Hydrogen and Fuel Cell Technologies for Heating: A Review. *International journal of hydrogen energy* **2015,** *40*, 2065-2083.

169.   Naguib, M.; Halim, J.; Lu, J.; Cook, K. M.; Hultman, L.; Gogotsi, Y.; Barsoum, M. W., New Two-Dimensional Niobium and Vanadium Carbides as Promising Materials for Li-Ion Batteries. *Journal of the American Chemical Society* **2013,** *135*, 15966-15969.

170.   Mounasamy, V.; Mani, G. K.; Ponnusamy, D.; Tsuchiya, K.; Prasad, A. K.; Madanagurusamy, S., Template-Free Synthesis of Vanadium Sesquioxide (V_2O_3) Nanosheets and Their Room-Temperature Sensing Performance. *Journal of Materials Chemistry A* **2018,** *6*, 6402-6413.

171.   Choi, J.-G., The Surface Properties of Vanadium Compounds by X-Ray Photoelectron Spectroscopy. *Applied surface science* **1999,** *148*, 64-72.

172.   Harris, K. J.; Bugnet, M.; Naguib, M.; Barsoum, M. W.; Goward, G. R., Direct Measurement of Surface Termination Groups and Their Connectivity in the 2D MXene V_2CT_x Using Nmr Spectroscopy. *The Journal of Physical Chemistry C* **2015,** *119*, 13713-13720.

173.   Khazaei, M.; Arai, M.; Sasaki, T.; Chung, C. Y.; Venkataramanan, N. S.; Estili, M.; Sakka, Y.; Kawazoe, Y., Novel Electronic and Magnetic Properties of Two-Dimensional Transition Metal Carbides and Nitrides. *Advanced Functional Materials* **2013,** *23*, 2185-2192.

174.   Liu, F.; Zhou, A.; Chen, J.; Jia, J.; Zhou, W.; Wang, L.; Hu, Q., Preparation of Ti_3C_2 and Ti_2C Mxenes by Fluoride Salts Etching and Methane Adsorptive Properties. *Applied Surface Science* **2017,** *416*, 781-789.

175.   Junkaew, A.; Arróyave, R., Enhancement of the Selectivity of MXenes (M_2C, M= Ti, V, Nb, Mo) Via Oxygen-Functionalization: Promising Materials for Gas-Sensing and-Separation. *Physical Chemistry Chemical Physics* **2018,** *20*, 6073-6082.

176.   Xu, X.; Yin, M.; Li, N.; Wang, W.; Sun, B.; Liu, M.; Zhang, D.; Li, Z.; Wang, C., Vanadium-Doped Tin Oxide Porous Nanofibers: Enhanced Responsivity for Hydrogen Detection. *Talanta* **2017,** *167*, 638-644.

177.   Wang, Y.-T.; Whang, W.-T.; Chen, C.-H., Hollow V_2O_5 Nanoassemblies for High-Performance Room-Temperature Hydrogen Sensors. *ACS applied materials & interfaces* **2015,** *7*, 8480-8487.

178.   Simo, A.; Mwakikunga, B.; Maaza, M., One-Dimensional Vanadium Dioxide Nanostructures for Room Temperature Hydrogen Sensors. *Sensors & Transducers* **2015,** *189*, 143.

179.   Pak, Y.; Kim, S.-M.; Jeong, H.; Kang, C. G.; Park, J. S.; Song, H.; Lee, R.; Myoung, N.; Lee, B. H.; Seo, S., Palladium-Decorated Hydrogen-Gas Sensors Using Periodically Aligned Graphene Nanoribbons. *ACS applied materials & interfaces* **2014,** *6*, 13293-13298.

180.   Zhu, L.; Jia, Y.; Gai, G.; Ji, X.; Luo, J.; Yao, Y., Ambipolarity of Large-Area Pt-Functionalized Graphene Observed in H_2 Sensing. *Sensors and Actuators B: Chemical* **2014,** *190*, 134-140.

181.   Assar, M.; Karimzadeh, R., Enhancement of Methane Gas Sensing Characteristics of Graphene Oxide Sensor by Heat Treatment and Laser Irradiation. *Journal of colloid and interface science* **2016,** *483*, 275-280.

182.   Seo, J.; Lim, Y.; Shin, H., Self-Heating Hydrogen Gas Sensor Based on an Array of Single Suspended Carbon Nanowires Functionalized with Palladium Nanoparticles. *Sensors and Actuators B: Chemical* **2017,** *247*, 564-572.

183.   Reddeppa, M.; Park, B.-G.; Kim, M.-D.; Peta, K. R.; Chinh, N. D.; Kim, D.; Kim, S.-G.; Murali, G., H_2, H_2S Gas Sensing Properties of RGO/Gan Nanorods at Room Temperature: Effect of UV Illumination. *Sensors and Actuators B: Chemical* **2018,** *264*, 353-362.

184.   Kuru, C.; Choi, D.; Kargar, A.; Liu, C. H.; Yavuz, S.; Choi, C.; Jin, S.; Bandaru, P. R., High-Performance Flexible Hydrogen Sensor Made of WS_2 Nanosheet–Pd Nanoparticle Composite Film. *Nanotechnology* **2016,** *27*, 195501.

185.   Zhang, D.; Jiang, C.; Zhang, Y., Room Temperature Hydrogen Gas Sensor Based on Palladium Decorated Tin Oxide/Molybdenum Disulfide Ternary Hybrid Via Hydrothermal Route. *Sensors and Actuators B: Chemical* **2017,** *242*, 15-24.

186.   Baek, D.-H.; Kim, J., MoS_2 Gas Sensor Functionalized by Pd for the Detection of Hydrogen. *Sensors and Actuators B: Chemical* **2017,** *250*, 686-691.

187.   Kumar, R.; Goel, N.; Kumar, M., UV-Activated MoS_2 Based Fast and Reversible NO_2 Sensor at Room Temperature. *ACS sensors* **2017,** *2*, 1744-1752.

188.   Chimowa, G.; Tshabalala, Z. P.; Akande, A. A.; Bepete, G.; Mwakikunga, B.; Ray, S. S.; Benecha, E. M., Improving Methane Gas Sensing Properties of Multi-Walled Carbon Nanotubes by Vanadium Oxide Filling. *Sensors and Actuators B: Chemical* **2017,** *247*, 11-18.

189.   Bo, Z.; Yuan, M.; Mao, S.; Chen, X.; Yan, J.; Cen, K., Decoration of Vertical Graphene with Tin Dioxide Nanoparticles for Highly Sensitive Room Temperature Formaldehyde Sensing. *Sensors and Actuators B: Chemical* **2018,** *256*, 1011-1020.

190.   Li, W.; Liang, J.; Liu, J.; Zhou, L.; Yang, R.; Hu, M., Synthesis and Room Temperature CH_4 Gas Sensing Properties of Vanadium Dioxide Nanorods. *Materials Letters* **2016,** *173*, 199-202.

191.   Liang, J.; Liu, J.; Li, W.; Hu, M., Preparation and Room Temperature Methane Sensing Properties of Platinum-Decorated Vanadium Oxide Films. *Materials Research Bulletin* **2016,** *84*, 332-339.

192.   Zhang, C. J.; Pinilla, S.; McEvoy, N.; Cullen, C. P.; Anasori, B.; Long, E.; Park, S.-H.; Seral-Ascaso, A. s.; Shmeliov, A.; Krishnan, D., Oxidation Stability of Colloidal Two-Dimensional Titanium Carbides (MXenes). *Chemistry of Materials* **2017,** *29*, 4848-4856.

193.   Liang, J.; Liu, J.; Li, N.; Li, W., Magnetron Sputtered Au-Decorated Vanadium Oxides Composite Thin Films for Methane-Sensing Properties at Room Temperature. *Journal of Alloys and Compounds* **2016,** *671*, 283-290.

194.   Varghese, S. S.; Varghese, S. H.; Swaminathan, S.; Singh, K. K.; Mittal, V., Two-Dimensional Materials for Sensing: Graphene and Beyond. *Electronics* **2015,** *4*, 651-687.

195.   Prezioso, S.; Perrozzi, F.; Giancaterini, L.; Cantalini, C.; Treossi, E.; Palermo, V.; Nardone, M.; Santucci, S.; Ottaviano, L., Graphene Oxide as a Practical Solution to High Sensitivity Gas Sensing. *The Journal of Physical Chemistry C* **2013,** *117*, 10683-10690.

196.   da Silva, M. F. P.; de Oliveira, D. R.; Cavallari, M. R.; Dirani, E. A. T.; Triboni, E. R.; Paterno, L. G.; Fonseca, F. J.; Ando, R. A.; da Silva Baptista, M.; Landers, R., A Simple Visible Light Photo-Assisted Method for Assembling and Curing Multilayer GO Thin Films. *Materials Chemistry and Physics* **2015,** *165*, 125-133.

197.   Latif, U.; Dickert, F. L., Graphene Hybrid Materials in Gas Sensing Applications. *Sensors* **2015,** *15*, 30504-30524.

198.   Feng, L.; Wu, L.; Qu, X., New Horizons for Diagnostics and Therapeutic Applications of Graphene and Graphene Oxide. *Advanced Materials* **2013,** *25*, 168-186.

199.   Hazra, S. K.; Basu, S., Graphene-Oxide Nano Composites for Chemical Sensor Applications. *C* **2016,** *2*, 12.

200.   Chen, C.; Cai, W.; Long, M.; Zhou, B.; Wu, Y.; Wu, D.; Feng, Y., Synthesis of Visible-Light Responsive Graphene Oxide/TiO$_2$ Composites with P/N Heterojunction. *ACS nano* **2010,** *4*, 6425-6432.

201.   Li, H.; Pang, S.; Wu, S.; Feng, X.; Müllen, K.; Bubeck, C., Layer-by-Layer Assembly and UV Photoreduction of Graphene–Polyoxometalate Composite Films for Electronics. *Journal of the American Chemical Society* **2011,** *133*, 9423-9429.

202.   Williams, G.; Seger, B.; Kamat, P. V., TiO$_2$-Graphene Nanocomposites. UV-Assisted Photocatalytic Reduction of Graphene Oxide. *ACS nano* **2008,** *2*, 1487-1491.

203.   Yin, X. M.; Li, C. C.; Zhang, M.; Hao, Q. Y.; Liu, S.; Li, Q. H.; Chen, L. B.; Wang, T. H., SnO$_2$ Monolayer Porous Hollow Spheres as a Gas Sensor. *Nanotechnology* **2009,** *20*, 455503.

204.   Zhang, Y.; Tang, Z.-R.; Fu, X.; Xu, Y.-J., TiO$_2$− Graphene Nanocomposites for Gas-Phase Photocatalytic Degradation of Volatile Aromatic Pollutant: Is TiO$_2$− Graphene Truly Different from Other TiO$_2$− Carbon Composite Materials? *ACS nano* **2010,** *4*, 7303-7314.

205.   Akhavan, O.; Abdolahad, M.; Esfandiar, A.; Mohatashamifar, M., Photodegradation of Graphene Oxide Sheets by TiO$_2$ Nanoparticles after a Photocatalytic Reduction. *The Journal of Physical Chemistry C* **2010,** *114*, 12955-12959.

206.   Perera, S. D.; Mariano, R. G.; Vu, K.; Nour, N.; Seitz, O.; Chabal, Y.; Balkus Jr, K. J., Hydrothermal Synthesis of Graphene-TiO$_2$ Nanotube Composites with Enhanced Photocatalytic Activity. *ACS Catalysis* **2012,** *2*, 949-956.

207.   Wang, P.; Zhai, Y.; Wang, D.; Dong, S., Synthesis of Reduced Graphene Oxide-Anatase TiO$_2$ Nanocomposite and Its Improved Photo-Induced Charge Transfer Properties. *Nanoscale* **2011,** *3*, 1640-1645.

208.   Ye, Z.; Tai, H.; Xie, T.; Su, Y.; Yuan, Z.; Liu, C.; Jiang, Y., A Facile Method to Develop Novel TiO_2/RGO Layered Film Sensor for Detecting Ammonia at Room Temperature. *Materials Letters* **2016,** *165*, 127-130.

209.   Zhang, W.; Cui, J.; Tao, C. a.; Wu, Y.; Li, Z.; Ma, L.; Wen, Y.; Li, G., A Strategy for Producing Pure Single-Layer Graphene Sheets Based on a Confined Self-Assembly Approach. *Angewandte Chemie* **2009,** *121*, 5978-5982.

210.   Wang, P.; Wang, J.; Wang, X.; Yu, H.; Yu, J.; Lei, M.; Wang, Y., One-Step Synthesis of Easy-Recycling TiO_2-RGO Nanocomposite Photocatalysts with Enhanced Photocatalytic Activity. *Applied Catalysis B: Environmental* **2013,** *132*, 452-459.

211.   Montes-Morán, M. A.; Young, R. J., Raman Spectroscopy Study of High-Modulus Carbon Fibres: Effect of Plasma-Treatment on the Interfacial Properties of Single-Fibre–Epoxy Composites: Part Ii: Characterisation of the Fibre–Matrix Interface. *Carbon* **2002,** *40*, 857-875.

212.   Hu, C.; Liu, Y.; Yang, Y.; Cui, J.; Huang, Z.; Wang, Y.; Yang, L.; Wang, H.; Xiao, Y.; Rong, J., One-Step Preparation of Nitrogen-Doped Graphene Quantum Dots from Oxidized Debris of Graphene Oxide. *Journal of Materials Chemistry B* **2013,** *1*, 39-42.

213.   Mabrook, M.; Hawkins, P., A Rapidly-Responding Sensor for Benzene, Methanol and Ethanol Vapours Based on Films of Titanium Dioxide Dispersed in a Polymer Operating at Room Temperature. *Sensors Actuators B: Chem.* **2001,** *75*, 197-202.

214.   Kang, S. M.; Park, S.; Kim, D.; Park, S. Y.; Ruoff, R. S.; Lee, H., Simultaneous Reduction and Surface Functionalization of Graphene Oxide by Mussel-Inspired Chemistry. *Advanced Functional Materials* **2011,** *21*, 108-112.

215. Zhang, L.-S.; Wang, W. D.; Liang, X.-Q.; Chu, W.-S.; Song, W.-G.; Wang, W.; Wu, Z.-Y., Characterization of Partially Reduced Graphene Oxide as Room Temperature Sensor for H$_2$. *Nanoscale* **2011,** *3*, 2458-2460.

216. Wu, X.; Sprinkle, M.; Li, X.; Ming, F.; Berger, C.; de Heer, W. A., Epitaxial-Graphene/Graphene-Oxide Junction: An Essential Step Towards Epitaxial Graphene Electronics. *Phys. Rev. Lett.* **2008,** *101*, 026801.

217. Cui, S.; Mao, S.; Wen, Z.; Chang, J.; Zhang, Y.; Chen, J., Controllable Synthesis of Silver Nanoparticle-Decorated Reduced Graphene Oxide Hybrids for Ammonia Detection. *Analyst* **2013,** *138*, 2877-2882.

218. Lipatov, A.; Varezhnikov, A.; Wilson, P.; Sysoev, V.; Kolmakov, A.; Sinitskii, A., Highly Selective Gas Sensor Arrays Based on Thermally Reduced Graphene Oxide. *Nanoscale* **2013,** *5*, 5426-5434.

219. Ago, H.; Kugler, T.; Cacialli, F.; Salaneck, W. R.; Shaffer, M. S.; Windle, A. H.; Friend, R. H., Work Functions and Surface Functional Groups of Multiwall Carbon Nanotubes. *The Journal of Physical Chemistry B* **1999,** *103*, 8116-8121.

220. Stratakis, E.; Savva, K.; Konios, D.; Petridis, C.; Kymakis, E., Improving the Efficiency of Organic Photovoltaics by Tuning the Work Function of Graphene Oxide Hole Transporting Layers. *Nanoscale* **2014,** *6*, 6925-6931.

221. Lightcap, I. V.; Kosel, T. H.; Kamat, P. V., Anchoring Semiconductor and Metal Nanoparticles on a Two-Dimensional Catalyst Mat. Storing and Shuttling Electrons with Reduced Graphene Oxide. *Nano Letters* **2010,** *10*, 577-583.

222. Buchsteiner, A.; Lerf, A.; Pieper, J., Water Dynamics in Graphite Oxide Investigated with Neutron Scattering. *The Journal of Physical Chemistry B* **2006,** *110*, 22328-22338.

223.   Phan, D.-T.; Chung, G.-S., Effects of Rapid Thermal Annealing on Humidity Sensor Based on Graphene Oxide Thin Films. *Sensors and Actuators B: Chemical* **2015,** *220*, 1050-1055.

224.   Cui, S.; Wen, Z.; Huang, X.; Chang, J.; Chen, J., Stabilizing MoS$_2$ Nanosheets through SnO$_2$ Nanocrystal Decoration for High-Performance Gas Sensing in Air. *Small* **2015,** *11*, 2305-2313.